

**REPORT DOCUMENTATION PAGE****Form Approved**  
**OMB No. 0704-0188**

Public reporting burden for this collection of information is estimated to average 1 hour per response, including the time for reviewing instructions, searching data sources, gathering and maintaining the data needed, and completing and reviewing the collection of information. Send comments regarding this burden estimate or any other aspect of this collection of information, including suggestions for reducing this burden to Washington Headquarters Service, Directorate for Information Operations and Reports, 1215 Jefferson Davis Highway, Suite 1204, Arlington, VA 22202-4302, and to the Office of Management and Budget, Paperwork Reduction Project (0704-0188) Washington, DC 20503.

**PLEASE DO NOT RETURN YOUR FORM TO THE ABOVE ADDRESS.**

|   |                                |  |
|---|--------------------------------|--|
| <b>1. REPORT DATE (DD-MM-YYYY)</b><br>29-08-2013  | <b>2. REPORT TYPE</b><br>FINAL | <b>3. DATES COVERED (From - To)</b><br>06-12-2010 - 31-08-2013 |
| <b>4. TITLE AND SUBTITLE</b><br>Northwest Manufacturing Initiative  |                                | <b>5a. CONTRACT NUMBER</b>                                     |
|   |                                | <b>5b. GRANT NUMBER</b><br>W911NF-11-1-0023                    |
|   |                                | <b>5c. PROGRAM ELEMENT NUMBER</b>                              |
| <b>6. AUTHOR(S)</b><br>David E. Culler, Ph.D.<br>W. Wood<br>J. Kadali<br>R. Talla<br>R. Hugo<br>T. Russell<br>A. Thoreson<br>E. Porgharibshahishahrehabak<br>Dae-wook Kim<br>Ellen A. Fuller<br>J. Rick Evans   |                                | <b>5d. PROJECT NUMBER</b>                                      |
|   |                                | <b>5e. TASK NUMBER</b>   |
|   |                                | <b>5f. WORK UNIT NUMBER</b>                                    |
| <b>7. PERFORMING ORGANIZATION NAME(S) AND ADDRESS(ES)</b><br>Organization for Economic Initiatives, Inc.<br>1144 Gateway Lp, Ste 203<br>Springfield OR 97477-7750   |                                | <b>8. PERFORMING ORGANIZATION REPORT NUMBER</b>                |
| <b>9. SPONSORING/MONITORING AGENCY NAME(S) AND ADDRESS(ES)</b><br>US Army RDECOM ACQCTR - W911NF<br>4300 S. Miami Blvd.; Durham NC 27703<br><br>Monitoring Agency: ONRRO; 300 Fifth Ave., Suite 710; Seattle WA 98104   |                                | <b>10. SPONSOR/MONITOR'S ACRONYM(S)</b>                        |
|   |                                | <b>11. SPONSORING/MONITORING AGENCY REPORT NUMBER</b>          |
| <b>12. DISTRIBUTION AVAILABILITY STATEMENT</b><br>Approved for public release; distribution unlimited.  |                                |  |
| <b>13. SUPPLEMENTARY NOTES</b><br>The views, opinions and/or findings contained in this report are those of the author(s) and should not be construed as an official Department of the Army position, policy or decision, unless so designed by other documentation.  |                                |  |
| <b>14. ABSTRACT</b><br>Advanced manufacturing and applied research in automation continue to be areas that are important to our national engineering infrastructure, industrial competitiveness and preparing the next generation through education. The Oregon Institute of Technology has demonstrated great progress in the areas of product development, autonomous robots and composites manufacturing over the last 3 years due in great part to the grant/s provided by the US Army. Through a collaboration between the Manufacturing/Mechanical program and the Computer Software Engineering Technology program, a Smart Materials Warehouse that is run with robots and monitored by an "eye in the sky" IP camera was developed. Product development capabilities have been greatly improved with the addition of a 130W CO2 laser and a CNC foam/wood router. Finally, the composites area has been enhanced with a filament winder developed in house. The results are presented in this report and have helped increase enrollment and Oregon Tech's national rankings. Analysis of physically vapor deposited hard Cr, Ti, and Zr base coatings deposited onto HRC 52 low alloy steel at 250oC substrate temperature. Evaluation included TEM, SEM, Erosion testing, acoustic emission, scratch testing, strain to failure methods. Coatings were ranked. Cold Metal Transfer (CMT) pulsed GMAW to deposit AWS ER 307 onto HRC50 hardened steel coupons ranging from 2mm to 6.35mm thickness. Single layer deposit height ranged from 1-2mm thickness. A minimum heat input of 0.066KJ/mm was used. Fiber reinforced plastic (FRP) composite materials offer many |                                |  |

# INSTRUCTIONS FOR COMPLETING SF 298

advantages over metals, however, FRP composites exhibit some distinct disadvantages such as defects, limited performance data, limited repair technology, and high fabrication cost. Ultra-hard ceramic coatings such as diamond, nanocomposite and AlTiN were applied into the tools for CFRP drilling. The diamond coated drill showed the most consistent hole size and lowest roundness because of its superior wear resistance. Due to the abrasive nature of carbon fibers, the other coated tools did not show significant improvement over uncoated carbide tool. In order to improve the mechanical performance of FRP composite structural joints, the interference-fit fastening technology was studied. Experimental and numerical studies showed that the average fatigue life when modest amount of interference-fit was applied. The optimal interference-fit % varies among the FRP materials systems. Fatigue enhancement of interference-fit joints may be due to local pre-compression stresses induced by inference-fit, which improves the joint stiffness.

## 15. SUBJECT TERMS

Autonomous and Mobile Robots, CAD/CAM and Numerical Control, Composites Manufacturing, Physical vapor deposition, cold metal transfer, erosion, scratch test, hardness, thin film, TiN, CrN, ZrN, TEM, SEM, low alloy steel, PVD, PEMS, nano indentation, acoustic emission, strain to failure, Composites, Fiber reinforced plastics, CFRP, GFRP, Drilling, Tools, Ultra-hard coatings, Hole quality, Interference-fit, Bearing strength, Fatigue life, Fatigue enhancement, Joint stiffness, FE simulations.

## 16. SECURITY CLASSIFICATION OF:

a. REPORT  
U

b. ABSTRACT  
U

c. THIS PAGE  
U

17. LIMITATION OF  
ABSTRACT  
UL

18. NUMBER  
OF PAGES  
145

19a. NAME OF RESPONSIBLE PERSON  
J. Rick Evans

19b. TELEPHONE NUMBER (Include area code)  
541-756-5596

---

## **Northwest Manufacturing Initiative**

**Grant: W911NF-11-1-0023**

**Mr. Rick Evans, Administrative Representative**

**Organization for Economic Initiatives, Inc.  
1144 Gateway Loop, Suite 203  
Springfield OR 97477-7750**

**Prepared By:  
Oregon Institute of Technology  
Portland State University  
Washington State University – Vancouver  
Ellen A. Fuller  
J. Rick Evans**

**31 August 2013**

**Final Report**

**Unclassified**

Approved for public release; distribution unlimited.

The views, opinions and/or findings contained in this report are those of the author(s) and should not be construed as an official Department of the Army position, policy or decision, unless so designed by other documentation.

**US ARMY RDECOM ACQ CTR – W911NF  
4300 S. MIAMI BLVD  
DURHAM NC 27703**

## TABLE OF CONTENTS

|                       |          |
|-----------------------|----------|
| <b>Foreword .....</b> | <b>3</b> |
|-----------------------|----------|

### **Executive Summaries**

|   |    |
|---|----|
| Oregon Institute of Technology (OIT) Executive Summary..... | 4  |
| Portland State University (PSU) Executive Summary.....      | 7  |
| Washington State University (WSU) Executive Summary .....   | 10 |

### **Appendices**

|                                     |     |
|-------------------------------------|-----|
| Appendix A - OIT Final Report.....  | A-1 |
| Appendix B - PSU Final Report ..... | B-1 |
| Appendix C - WSU Final Report.....  | C-1 |

## **Foreword**

The Organization for Economic Initiatives, Inc. (OEI) is pleased to submit this final progress report for W911NF-11-1-0023. We have provided both performance and fiscal oversight for the entire project, including our partner organizations, through reports, site visits, and financial reviews. This report provides details on our collaborative research into 1) improving equipment life-cycle through in-service restoration using two coatings technologies: physical vapor deposition and cold metal transfer using gas metal arc welding, 2) limiting defects and improving repair technologies in the use of fiber reinforced plastic (FRP) composite materials, and 3) the development of agile, reconfigurable automated manufacturing environments. These research components address both defense industrial base capability gaps and defense systems engineering gaps. Statements of the problems studied and summaries of the most important results can be found in the Executive Summaries of our collaborative partner organization, including Portland State University, Washington State University, and Oregon Institute of Technology. The detailed research data from each of our partners can be found in the appendices.

**Executive Summary for Army Research Labs Grant (ARL 10)**  
**Oregon Institute of Technology**  
**Department of Manufacturing and Mechanical Engineering and Technology (MMET)**  
**Written By: Principle Investigator and Budget Authority Dr. David Culler**

Manufacturing technologies have evolved over the last five decades into highly integrated systems that incorporate many aspects of *Product Design and Development, Planning and Scheduling and Shop Floor Automation*. The widespread application of Computer Aided Design and Manufacturing (CAD/CAM), Computer Numerical Control (CNC), Product Lifecycle Management (PLM), industrial robotics and the use of composite materials are just a few of the pieces of the manufacturing automation landscape that are commonplace in industries such as defense, automotive, aerospace, and many others. The merging of the above mentioned technologies and tools into integrated systems continues to create new opportunities and challenges that must be faced not only in industry but, also at the educational level so that the next generation of engineers, technologists and scientists are prepared to design, build and operate systems that are more flexible, agile, re-configurable and efficient than ever before. To achieve this goal, people from diverse disciplines (including mechanical, electrical, industrial and software) will have to combine their efforts and work in cohesive teams.

There is currently much interest at the national level in reducing the capital cost and time required to modify manufacturing processes to respond to changing product and market demands. The Oregon Institute of Technology (Oregon Tech) has made significant contributions to the national effort through the development of initiatives, laboratories and engineering / technology programs that are focused on teaching theoretical concepts in parallel with hands-on applications to train engineers that are “work ready”. By taking this approach and complementing the classroom/lab educational experience with the type of applied research and systems development made possible by this ARL grant, Oregon Tech has established itself as one of the top ranked universities in the country, recently being ranked 48<sup>th</sup> among the top 20% of engineering programs, and the number one program in the state of Oregon in terms of return on investment for the student as well as the top spot for placement of students in their field upon graduation at the highest starting salaries.

The continued growth and development of the three labs affected by this grant; 1) Product Development and Machining (CAM) Lab, 2) Smart Automation Lab and 3) Composites Manufacturing Lab have benefitted greatly from the work and equipment acquisitions made possible by the ARL grant. It has been used to increase teaching and manufacturing capabilities in many areas, support faculty and program development and provide both income and project topics for both undergraduate and graduate students. Aside from the benefits to engineering programs and students directly, this project has taken important steps and identified new opportunities to assist the regional defense and manufacturing sector with a source of education and training in the varied technologies, automation and integrated systems that are used in prototype and composite material product development.

The report that accompanies this executive summary covers in detail each of the areas of research, product development / automation aspects and equipment acquisitions that occurred as a result of this grant during the period of 2011-2013. Only a brief outline of the major areas and a short description of the major accomplishments in each area are presented here as part of the executive summary.

**1. *Prototype Product Development and Computer Integrated Manufacturing (CIM) Cell***

A Flexible Manufacturing System (FMS) is a completely automated production line where material handling, processing, inspection and management are computerized. The team used existing and new components to build a cell that combines PLC's with a conveyor, robotics, bar code, vision system and a C-More panel to understand and re-configure the system for various products. This laid the groundwork for implementing vision cameras and software for inspection, product identification and data collection that will be used in classes and for further research. With the ARL funding, a new 150W laser and an 8' X 4' CNC router were purchased and installed. These machines are fast and provide a platform for rapid development of assemblies, molds and components.

**2. *Development of Robotic Control Systems for Mobile Robots***

Starting with 2 new workstations where the basics of servo and stepper motor controls can be taught and existing IRobot® and BattleBot platforms, a completely new control system (including software interfaces) were developed and used to build both 2 wheel and 4 wheel driven mobile, wireless robots for use in various applications including the Smart Materials Warehouse discussed later. The Arduino® controller boards and Gecco® drives are the basis for the configuration. Visual Studio and C# (C-sharp) were used to develop a Graphical User Interface where all the functionality of the robots could be utilized. The 4 robots designed and built include 2 basic bots a forklift bot and a 4 wheel model used for mounting the Kinect® cameras from X-Box gaming as well as a laptop so that the robot could recognize obstacles and generate 3D images for processing and guidance purposes when the robot works on the manufacturing floor.

**3. *Qualifying for Industrial / Educational CERT Program with FANUC® Robotics***

As part of the previous phases of the ARL research, various FANUC robots were purchased and installed for the purpose of teaching, work-cell configuration and applied research. In order to become part of the national network of FANUC CERT training sites around the country, 32 hours of training in Lake Forest CA were required and other requirements had to be fulfilled that had not been completed previously. Thanks to the ARL grant, this process was completed and two faculty have been certified, thus making Oregon Tech one of the few sites on the west coast with the ability to certify students as well as industry professionals in the operation and programming of multiple standard models. The certification also meant that students would be able to use an extensive E-Learning package and robot simulators that were not available previous to the completion of the training. Updates, tech support and connecting to other universities in the network were additional benefits of meeting the criteria set by FANUC.

#### **4. *Acquisition and Implementation of Composites Manufacturing Equipment***

Among the manufacturing industries most important to the North West region are aerospace and defense. Composite materials, including their processing and use to build new products are one of the focus areas of the engineering program at Oregon Tech. Through funding and student work supported in this grant, two important processes have been added to the laboratory used by students and faculty. First, the addition of a CNC foam and wood router with a large Z-travel capability has greatly improved the ability to build molds and designs created using 3D CAD models. This machine was used non-stop to make the entire air package (wings, spoilers, nose-cone and covers) during preparation for the recent Formula 1 competition. Secondly, a basic filament winder used to create cylindrical parts from composite filament and resin was designed, built and installed. Rocket bodies, UAV parts and tubing are just a few of the examples of what has been built by students using the new machine. A software program called CADFIL® has also been installed. This software helps the user design the components, mandrels and CNC code to develop products on the filament winder.

#### **5. *Smart Materials Warehouse Applying Vision Systems and Custom Software EmguCV®***

The objective of this research is to develop systems that can manage work-cells and factory floors using autonomous, mobile robots in conjunction with IP high resolution cameras mounted in the ceiling of the building. This work combined the efforts of manufacturing graduate students and groups of Computer Software Engineering Technology (CSET) students to develop a prototype environment to make deliveries automatically around a typical materials warehouse. Utilizing the robots discussed above in section 2, the simulated 40' X 40' warehouse had a receiving area where the first robot would get a call from the system and move over to read a bar-code from the pallet and, based on the product I.D., deliver the raw-stock to processing stations where it could be cut and shaped into blanks for subsequent machining. Using a custom made software developed in Visual Studio and EmguCV, routes could interactively be defined for different products, the ceiling mounted camera would monitor warehouse activities and robot movements and data was collected to provide feedback and system performance. Since current systems in use rely on RFID tags or magnetic strips to guide robots, the results of this work demonstrated a unique approach that could be applied in military and industrial applications including surveillance, supplies management, operations in dangerous zones and automated manufacturing. Faculty, students and visitors were impressed and satisfied with the progress and results that came out of this collaborative, multi-disciplinary research effort.

In conclusion, the work and resources that have resulted from the ARL grant have been critical to the growth and success of various engineering programs and student projects at the Oregon Institute of Technology during the period of the grant. The machinery, processes, software and research findings not only contributed to projects already completed but will also serve as a foundation to continue work in multiple areas in the future. As this report demonstrates, there are opportunities to expand and develop projects and new capabilities in every area described above. It has been a rewarding experience for everyone involved and great for our students.



## Portland State University Executive Summary

This project considered two surfacing technologies, magnetron sputtered, PVD, and an emerging technology low heat input Cold Metal Transfer, CMT, gas metal arc welding process. Traditional PVD process substrate temperatures are 400°C, precluding PVD on fully hardened low alloy steels. This project considered a range of PVD hard coatings and deposition conditions, including plasma assisted, all at substrate temperatures of 250°C. At this temperature the initial substrate hardness, HRC 52 was maintained. One potential application of this reduced substrate temperature is as a replacement for electrolytic hard chrome coatings. Evaluation of the properties of the PVD coatings was benchmarked to traditional hexavalent deposited chromium. Coatings were deposited by Southwest Research Institute. In addition to conventional PVD, coatings were deposited using plasma enhanced magnetron sputtering, PEMS. Coatings were evaluated chemically, microstructurally, and mechanically via scratch, erosion, and mechanical strain induced failure. Coating hardness varied from HK400 to about HK4000. The coatings were ranked by each evaluation criteria and the results for select coatings included in the summary table. The optimum coating choice depends on the specific evaluation criteria considered most important. Several of the coatings performed better than the chromium benchmark. The results indicate that deposition parameters and coating types can be tailored using the low temperature PVD and PEMS process and can be considered for replacement of traditional hard chrome coatings for wear and corrosion resistance.

| Coating | PVD N2 flow | PVD or PEMS | Ranking |     |              |                          |             |         |           | HV (Nano) |
|---------|-------------|-------------|---------|-----|--------------|--------------------------|-------------|---------|-----------|-----------|
|         |             |             | AE      | SEM | HRC Adhesion | Erosion 90o              | Erosion 30o | Scratch | Structure |           |
|         |             |             |         |     |              | mass loss (g)/gm erodant |             |         |           |           |
| Cr2N    | low         | PVD         |         |     | 1            | 5                        | 5           | 4       | 3         | 860       |
| CrN     | high        | PVD         |         |     | 1            | 5                        | 5           | 9       | 3         | 671       |
| ZrN     | low         | PVD         | M       | L   | 1            | 4                        | 4           | 1       | 1         | 2598      |
| ZrN     | high        | PVD         | L       | L   | 1            | 1                        | 1           |         | 1         | 1849      |
| ZrSiCN  | low         | PVD         | M       | L   | 5            | 2                        | 2           |         | 1         | 2615      |
| ZrSiCN  | high        | PVD         | M       | L   | 2            | 5                        | 5           |         | 1         | 1639      |
| TiN     | low         | PVD         | L       | L   | 1            | 5                        | 5           |         | 1         | 1411      |
| TiN     | high        | PVD         | M       | M   | 3            | 2                        | 2           | 8       | 3         | 2088      |
| TiN     | low         | PEMS        | L       | M   | 2            | 5                        | 5           |         | 1         | 1307      |
| TiN     | high        | PEMS        |         |     | 1            | 4                        | 4           |         | 4         | 1487      |
| TiSiCN  | low         | PVD         | L       | M   | 3            | 1                        | 1           |         | 1         | 2081      |
| TiSiCN  | high        | PVD         |         |     | 2            | 2                        | 2           | 6       | 1         | 2554      |
| TiSiCN  | low         | PEMS        |         |     | 1            | 1                        | 1           |         | 1         | 2139      |
| TiSiCN  | high        | PEMS        |         |     | 1            | 3                        | 3           |         | 2         | 2208      |
| EHCr    | NA          | NA          | M       | M   |              | 5                        | 5           | 4       |           |           |

### Acoustic Emission crack sensitivity

(AE): L=least, M=Most sensitive

### Image analysis crack sensitivity

(SEM): L= Least, M=Most sensitive

**HRC indent coating adhesive failure sensitivity** : 1=best, 5=worst

**Structure quality**:1=best, 5= worst microstructure quality

The CMT patented low heat input pulsed GMAW welding process is designed for spatter free joining of very thin metals including aluminum and titanium. Its uniquely designed features suggest its potential application for low heat input surfacing. A range of process deposition parameters were evaluated by deposition onto quench and tempered AISI 4142 steel, HK<sub>500gm</sub> 533, with thicknesses between 2mm and 6.35mm. Single pass layer thicknesses ranged from 1-2mm. The CMT's preprogrammed digital computer based control system presented challenges for establishing the minimum potential heat input and layer thickness. The preprogrammed logic is optimized for joining, not surfacing and optimization for surfacing would benefit by permitting the end user access to control

algorithms that could lead to thinner single layer deposits with even lower heat input than achieved in this effort, 0.065Kj/mm, (1.65Kj/in).

## **Washington State University Executive Summary**

Fiber reinforced plastic (FRP) composite materials offer many advantages over metals, such as high specific strength and stiffness, excellent formability, and corrosion resistance. Increasing efforts have been made to incorporate these materials into the design of various components and structures for commercial/military craft as well as renewable energy systems. Due to the advantages from the FRP materials, Oregon/Southwest Washington based manufacturing companies (Boeing, Christensen/RECS, Oregon Iron Works, Miles Fiber Glass, etc) put their effort on increasing amount of FRP materials in their products. However, FRP composites exhibit some distinct disadvantages such as defects, limited performance data, limited repair technology, and high fabrication cost.

One of the serious issues with composite fabrication is defect left from manufacturing and/or assembly. For example, the high strength and abrasive nature of the FRP materials cause excessive tool wear and often result in poor work piece quality when making holes using the drilling process. Ultra-hard coatings such as CVD diamond, AlTiN, and nanocomposite coatings with the base tungsten carbide (WC) tool were used for drilling carbon fiber reinforced plastics (CFRP) composites. The nanocomposite coating has a nano-scale matrix structure comprised of  $\text{Si}_3\text{N}_4$  and AlTiN. The tool wear in CFRP machining was quite different from that in conventional metal machining. The primary wear type was a dulling or blunting of the cutting edge, which has been referred to as edge rounding wear or edge recession. In this paper, a hypothesis has been developed to explain the edge rounding wear in CFRP machining. Due to the fracture-based chip formation of CFRP, there is lack of the work material stagnation zone in front of the cutting edge, which normally prevents the edge wear in metal machining. Series of wear lead to rapid dulling of the cutting edge. The diamond coating significantly reduces the edge rounding wear. However, AlTiN coated drills showed no visible improvement over the uncoated carbide drill, despite of their high hardness, thus not protecting the drill. This is due to the oxidation of AlTiN coating during machining. The hole quality parameters of ultra-hard coated drills were compared with those of the uncoated carbide drills when drilling CFRP. The hole quality parameters chosen for the study include hole size, hole roundness, surface roughness, and entry delamination. The diamond coated drill showed the most consistent hole size and lowest roundness because of its superior wear resistance. The other coated tools showed a two hole-size trends of coating removal and subsequent carbide wear. It was found that surface roughness and delamination damage slightly increased with tool wear for all three coated carbides and uncoated carbides. Of the various coatings tested, the diamond coated drill showed the slightly better performance overall. The nanocomposite and AlTiN coated tools showed better hole quality initially than the uncoated. However, the wear of coatings led to a decrease in hole quality.

Another issue with FRP composite fabrication is the integrity of assembled FRP structures. Due to the size limitation of composite consolidation processes, FRP sheets should be assembled. FRP structural joints can be created by adhesion (using a matrix as a glue) or by mechanical fastening using bolts or fasteners. Adhesion offers the greatest joint strength, but does not allow for replacement, maintenance, or removal of sections. Mechanical fastener joints allow for the removal of components and high durability, but create discontinuities in the fiber, delamination in fiber matrix interfaces, and allow for moisture absorption. For the large FRP structures such as commercial aircraft, mechanical

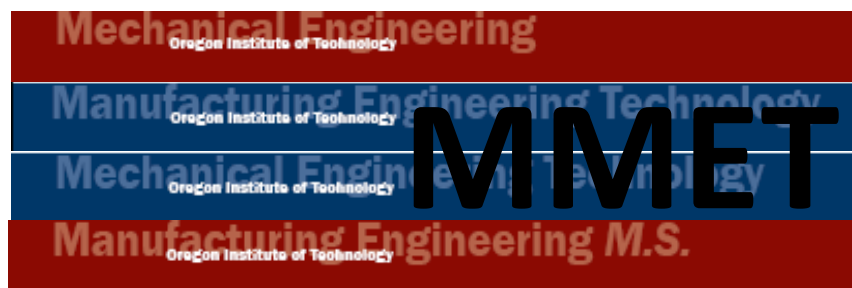
fastening is widely used for their final assembly. Fastening with clearance-fit pins is widely used, however, it allows moisture intrusion and escape, which limits their use in many applications where fluids must be contained to either prevent leaks/spills, or to prevent the composite itself from absorbing moisture which causes increased inter-laminar degradation. Interference-fit pins from 0.4% to 1% interference were applied to 6.35 mm hole glass fiber reinforced plastics (GFRP) composites to investigate the beneficial effects of interferences in terms of static strength/stiffness and fatigue life. An interference-fit pin installation process simulation using three-dimensional (3-D) finite element analysis (FEA) was conducted considering the friction coefficient (0.1) with various interference-fit percentages. FEA results show that interference-fit induces the compressive stresses in the radial direction while the tensile stresses remain in the tangential direction. The magnitudes of the stresses increase with increasing interference-fit percent up to 1%. The strain gauge experimental results agree well with the numerical results. The strain magnitudes after the pin installation increase with increasing interference-fit percent. As for the sample with 1% interference-fit, discrepancy between the experimental result and the numerical result was observed on the strain profiles when installing the pin. This may be due to the micro-scale fibre damage occurred in local regions around the hole due to large amount of interference-fit percent between the pin and GFRP hole during the pin installation experiments. The quasi-static and fatigue properties of the pin-loaded GFRP composites with interference-fit (up to 1%) are then compared to samples with transition-fit (0% of interference-fit). Even with possible local damage on the joints, interference-fit does not degrade the performance of the composite joints under quasi-static loading, especially when kept under 1% of interference-fit. Average bearing strength was slightly improved after insertion of interference-fit pin up to 1%. Larger bearing strength deviation was found at the interference-fit joined samples. When considering the scatter of raw data, the bearing strength values among the samples are overlapped. The hybrid processed sample has the largest bearing strength over the vacuum infusion and hand layup samples because the matrix-rich hand layup portion of the hybrid sample may obstruct inter- and intra-laminar cracks of the vacuum infusion portion, which carries most loading. The pin-loaded joints of GFRP laminate with 0.6% and 1% of interference-fit showed enhanced fatigue life than 0% of transition-fit. But, a few vacuum infusion and hybrid processed coupons with interference-fit of 1% had shorter fatigue life than 0% of transition-fit, due to their damage associated during pin installation. The joint stiffness per unit bearing area was improved by interference-fit of 0.6% in quasi-static test. This may be due to local pre-compression stresses induced by inference-fit, which improves the joint stiffness. This improved joint stiffness per unit bearing area by interference-fit may cause fatigue enhancement. In addition, interference-fit decreases the degradation rate of joint stiffness per unit bearing area over the fatigue cycles.

## **Appendix A – Oregon Institute of Technology Final Report**

# Final Report for Army Research Labs Grant (ARL 10)

## *Smart Automation, Robotics, Product Development and Composites*

Performing Organization: Oregon Institute of Technology  
Department of Manufacturing and Mechanical  
Engineering and Technology (MMET)



Written By: Dr. David Culler, PI

AUGUST, 2013

**Final Report for Army Research Labs Grant (ARL 10)**  
**Oregon Institute of Technology**  
**Department of Manufacturing and Mechanical Engineering and Technology**  
**Written By: Principle Investigator and Budget Authority Dr. David Culler**

## **Table of Contents**

|  |           |
|--|-----------|
| <b>Acknowledgments .....</b>   | <b>3</b>  |
| <b>Preface .....</b>   | <b>4</b>  |
| <b>Problem Statement.....</b>  | <b>4</b>  |
| <b>Background .....</b>  | <b>4</b>  |
| <b>Outline of Most Important Results .....</b>   | <b>5</b>  |
| <b>Computer Controlled (CNC) Filament Winder.....</b>  | <b>6</b>  |
| <b>Computer Integrated Manufacturing (CIM) Cell .....</b>  | <b>8</b>  |
| <b>Hurricane 130W Laser Cutter/Engraver (48" X 36") .....</b>                                    | <b>9</b>  |
| <b>Mobile Robot Development and Vision Systems for a Smart Materials Warehouse.....</b>          | <b>10</b> |
| <b>Fanuc Robotics CERT Training Site status for Oregon Institute of Technology.....</b>          | <b>18</b> |
| <b>ShopBot 3-Axis CNC Wood and Foam Router .....</b>   | <b>19</b> |
| <b>Teaching Stations for Stepper / Servo Motor Control .....</b>                                 | <b>20</b> |
| <b>Appendix 1: Vision Course Paper Presented at ASEE 2013 (Atlanta, GA).....</b>                 | <b>21</b> |
| <b>Appendix 2: Sample C# Code Developed For Mobile Robot Control .....</b>                       | <b>34</b> |
| <b>Appendix 3: Sample EMGU CV Code Developed for Eye In The Sky Camera Image Processing.....</b> | <b>40</b> |
| <b>Appendix 4: Sample C++ Code Developed for Kinect Camera Image Processing .....</b>            | <b>42</b> |
| <b>Appendix 5: Summary of Expenditures by Category .....</b>                                     | <b>48</b> |
| <b>Appendix 6: Engineering Dean's Newsletter from Spring 2012 .....</b>                          | <b>49</b> |

**Final Report for Army Research Labs Grant (ARL 10)**  
**Oregon Institute of Technology**  
**Department of Manufacturing and Mechanical Engineering and Technology**  
**Written By: Principle Investigator and Budget Authority Dr. David Culler**

## **Acknowledgements**

There are many people that have been involved at one stage or another of this project. Administrators, faculty, students, reviewers and managers deserve a lot of credit for the results. The original writer and PI of the project, John Anderson began with a vision for the robotics portion and recognized the need to expand our composite material manufacturing capabilities early on. The collaboration with Computer Software Engineering Technology (CSET) faculty Jim Long also provided a critical link to developing the software needed for image processing and working with cameras. The junior projects class worked very hard to develop programs needed to connect the Smart Materials Warehouse concept to the cameras and connections needed to demonstrate a final working system. We also had great support from MMET department chair Brian Moravec and ETM Dean Charlie Jones.

Some of the people are listed here:

### **MMET: Robotics & Vision**

Noah Anderson (MSMFG)  
Matthew Floyd (MSMFG)  
Hoe Jin Kim (MSMFG)

### **CSET: Kinect Systems**

Brenna Duffitt (BSCSET)  
Cody Noble (BSCSET)  
Jacob Norton (BSCSET)

### **CSET: Eye In The Sky**

Max Blumenthal (BSCSET)  
Mallory Conn (BSCSET)  
Jacob Tyler (BSCSET)  
Patrick Miki (BSCSET)

### **MMET: Filament Winder**

Shawn Smith (MSMFG)

### **Organization for Economic Initiatives**

Ellen A. Fuller  
Business/Grants Manager

**Oregon Institute of Technology**  
**Department of Manufacturing and Mechanical Engineering and Technology**  
**Written By: Principle Investigator and Budget Authority Dr. David Culler**

**Preface:**

The manufacturing sector in the Pacific Northwest has always played an important if not critical role in the economy of this region of the United States. In an effort to sustain and grow this sector, the Northwest Manufacturing Initiative began in 2008 and included funding for applied research, undergraduate and graduate program development and equipment purchases at three important universities; Oregon Institute of Technology in Klamath Falls, Portland State University and Washington State University in Vancouver. At Oregon Tech, the previous work was completed and documented in earlier reports. The focus of the current work (2010-2012) has been on robotics and smart automation research as well as the acquisition and implementation of manufacturing equipment. The three areas that are covered here and have produced important results are flexible product development, composites manufacturing and mobile robot guidance and monitoring with vision systems.

**Problem Statement:**

Academia, government and industry must work together so that current and future students are educated and prepared for jobs in diverse areas of engineering and manufacturing. It is well known that companies are having difficulty finding qualified personnel, especially in fields related to computing, the trades (machining, welding, high-tech equipment repair, etc.) and automation. Furthermore, skilled labor that is characterized by the combination of analytical knowledge, critical thinking, hands-on experience and the ability to function in multi-disciplinary teams is currently at a premium. One way that universities can help in fulfilling these needs is to create an environment in both the classroom and through lab experiences and applied research that challenge students in areas related to product development, automated equipment and the increasing role of computer software and programming in engineering applications. Many of these topics have been grouped together under the title "Smart Automation", which can incorporate many areas of modern manufacturing systems including computer aided systems (CA'X'), robotics, product / process data management and custom software programs. The purpose of this project is to create opportunities for faculty and students to participate and develop skills, technology and tools for working in these areas, thus helping industry and economic growth.

**Background:**

The Oregon Institute of Technology (Oregon Tech) is a regional leader among universities, offering many degree programs in engineering and technology. Oregon Tech prides itself on producing industry ready graduates that are able to make contributions at many levels due to their combination of theoretical studies and hands-on applications in labs and projects across the entire curriculum. Entering freshmen, unlike at many other universities, declare their major upon entry and immediately began to take classes related to their field of choice. Continuing to add new capabilities, equipment, current technologies and software is vital to the growth and continued success of our programs and student body. Manufacturing and flexible automation has traditionally been one of the strongest areas of our program. Both mechanical and manufacturing students are required to build early skill sets in machining, welding and computer aided design that serve as the foundation for junior and senior classes and projects such as machine design, finite element analysis, computer aided manufacturing and robotics. The culmination of this experience is a capstone/senior project lasting an entire year and completed in teams. Projects may be based on research being done by the professor in charge, the Formula 1 team or Mini Baja for a competition or a project where students try to solve an existing problem in a local or regional company.



### **Outline of Most Important Results:**

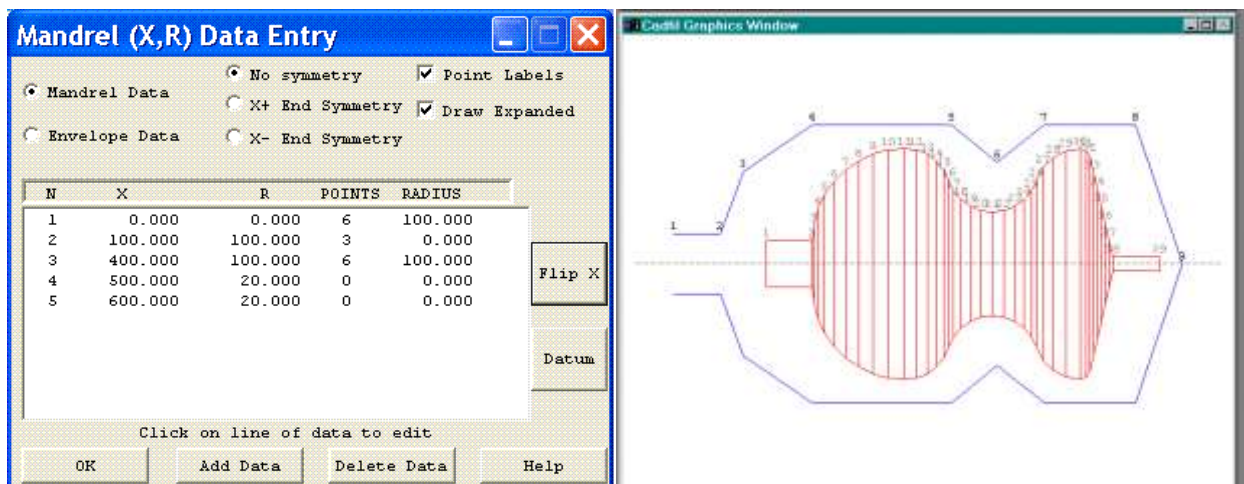
1. Filament Winder
  - a. Design and Build Machine (Structure, Physical Controls, Software)
  - b. Filament Winding Software CADFIL®
  - c. Product Development for UAV Project
2. Computer Integrated Manufacturing Cell
  - a. Programmable Automation (PLC, Robot, CNC)
  - b. Additions of C-More Panel, BarCode Reader, Imaging Source® camera
  - c. Paper Published at ASEE 2013 on 10 Week Vision Course (Included in Appendix)
  - d. Miniature Prototype Warehouse Application using Imaging Source and RoboRealm®
3. Hurricane 130W Laser Cutter/Engraver (48" X 36")
  - a. Rapid prototyping for product/project development
  - b. Provides size and power improvements/capabilities
  - c. Helps with program marketing and recruiting
  - d. Used to make plaques, awards, decorations, etc.
4. Smart Materials Warehouse
  - a. Robotic platforms and wireless control systems
  - b. Eye in the Sky project with Computer Software Engineering Technology students
  - c. Kinect Camera System mounted on Battlebot chassis with CSET students
  - d. Novel approach to guidance and monitoring of robots (AGV's) in manufacturing setting
5. Fanuc Robotics CERT Training Site status for Oregon Institute of Technology
  - a. California Training for 2 faculty members from MMET
  - b. Software, Simulators, E-Learning Software
  - c. Student Certification Program
6. ShopBot 3-Axis CNC Wood and Foam Router
  - a. Links to Composite Manufacturing and Labs
  - b. Links to support product development for Formula1 student racing team
  - c. 8' X 4' X 18" capacity creates opportunities for many projects and enhanced capabilities
7. Teaching Stations for Stepper / Servo Motor Control
  - a. Stepper motor/lead screw assembly to teach basic concepts to students
  - b. Servo motor/lead screw assembly to teach basic concepts to students

## 1. Computer Controlled (CNC) Filament Winder

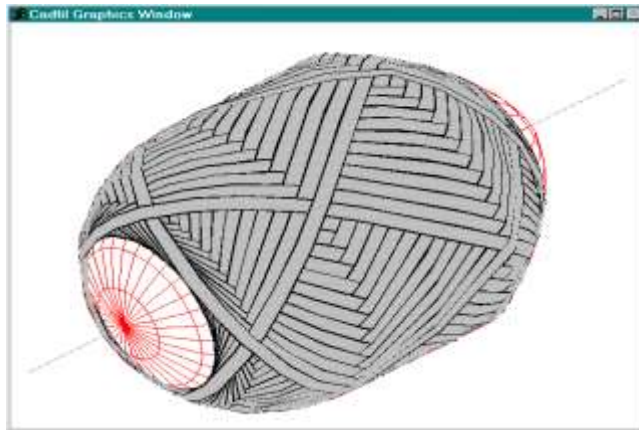
The composite filament winder previously under development was connected and used during the last few terms of the school year. A variety of rocket bodies were manufactured and different techniques for overlapping and wrapping were utilized. The Mach 2® control software was configured to operate the linear ball screws for the horizontal table and the spindle motor was connected. The machine will be very helpful for student projects and instruction purposes. The CADFIL® software that is used to integrate the CAD solid model of the product, the mandrel needed for creating the shape, the winding patterns to be applied and the generation of numerical control code was also implemented. A graduate student used a component of his UAV project as a test piece and the system worked satisfactorily. Safety devices, guards, electrical covers and cable routing guides were installed to make the machine compliant with university standards. The machine is housed in the composites labs and will be used in future projects. Many months were put into building the machine, testing and adding safety devices.



The CADFIL software program is used to develop the strategy and numerical control program that are needed to produce a component on a filament winder. For rotationally symmetric shapes the first stage in generating winding programs is to create a mandrel file defining the shape to be wound. At the same time the user can create a mandrel envelope. The mandrel and envelope data are saved in a text file with the .mnd file name extension. A mandrel definition consists of X,R data co-ordinates defining the surface. The user needs to define sufficient points to have a reasonable representation of the curvature of the mandrel profile. A mandrel envelope is a clearance surface around the mandrel on which the fiber-dispensing head will move. It is defined in the same way as the mandrel shape.



Having created a mandrel as described in previous sections a fiber path can be created. The fiber path defines the number and pattern that will be used to wind the fiber around the mandrel. Some of the attributes include how the path is started, fiber winding angle, requirements for the path to close down to a boss on the mandrel end and features of the mandrel that may give rise to difficulties. The geometry of the component, previously defined in mandrel generation, determines the stable paths that the user will be able to achieve. The main requirement of the fiber path is that it should not slip. Finally, the CADFIL software maps the fiber path from the surface of the component onto a notional control surface on which the winding machine is constrained to move. The user gives data relating to the materials that he will be using during the winding of the component. From these data, the system calculates the fiber bundle cross-sectional area, and by inclusion of the bandwidth will enable the system to calculate the thickness of the composite to be laid down and the cycles for coverage.



Band Pattern Selection

Number of cycles: 30 30 30

Initial Rotation: 11.0000 15.0000 Degrees

| SECTION | START   | NO. OF | TABLET | ARC/SEC | SEC/SEC | 1-SPD  | 2-SPD  |
|---------|---------|--------|--------|---------|---------|--------|--------|
| NO.     | PATTERN | CYCLES | NO.    | ANGLE   | CHARGE  | FACTOR |        |
| 1       | 10      | 30     | 11     | 99.00   | 60.00   | 1.0175 | 0.0175 |
| 2       | 21      | 30     | 11     | 213.00  | 116.00  | 1.0282 | 0.0282 |
| 3       | 7       | 30     | 11     | 166.00  | 140.00  | 1.0364 | 0.0364 |
| 4       | 7       | 30     | 11     | 204.00  | 148.00  | 1.0476 | 0.0476 |
| 5       | 11      | 30     | 11     | 219.00  | 212.00  | 1.0586 | 0.0586 |
| 6       | 10      | 30     | 11     | 275.00  | 220.00  | 1.0692 | 0.0692 |
| 7       | 1       | 30     | 11     | 348.00  | 332.00  | 1.0827 | 0.0827 |
| 8       | 1       | 30     | 12     | 12.00   | 356.00  | 1.0937 | 0.0937 |

OK Cancel

Click on pattern, then OK OK

Advised 2/11/81 Page 1-2

Extra shell (deg):

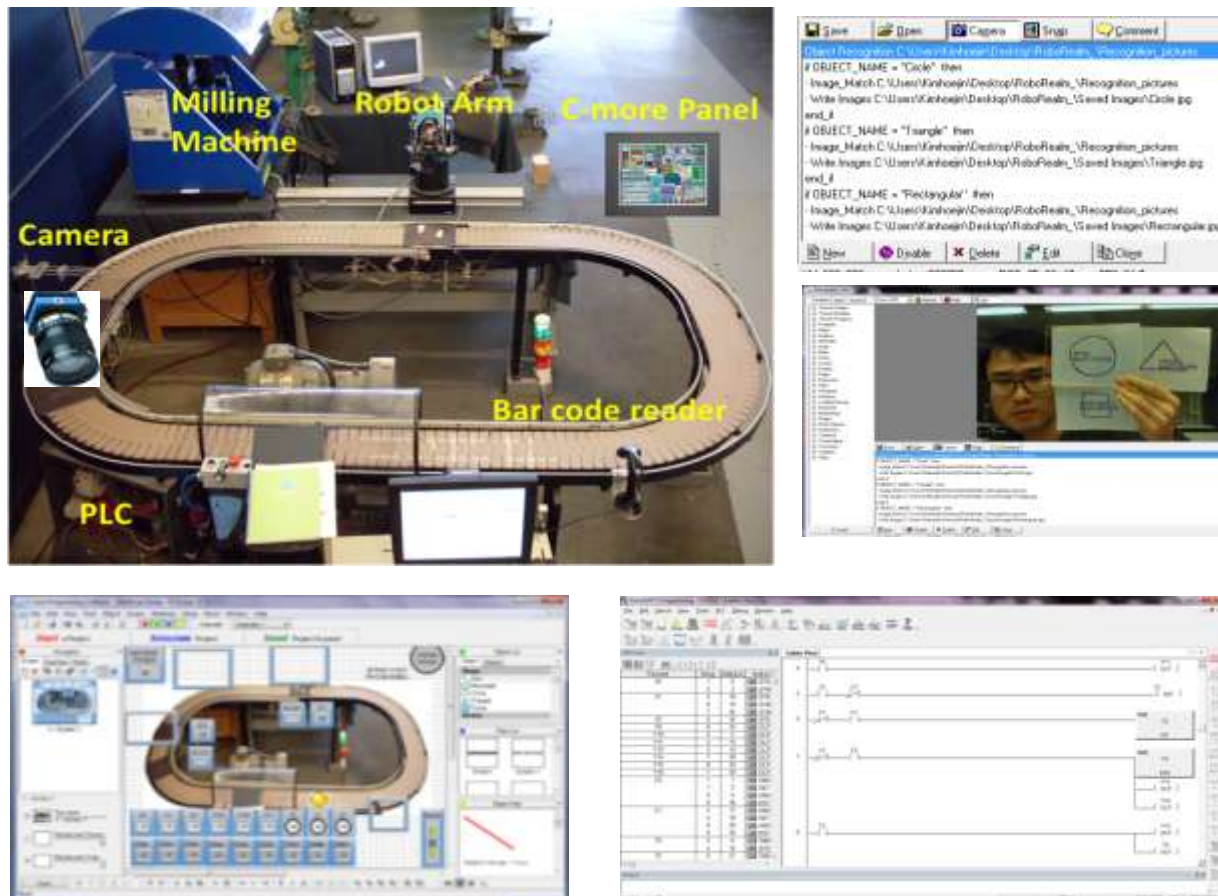
OK Cancel

The viewing section enables the user to view from any direction the component and one of its relevant payout path tracks. The payout path is shown as a series of payout eye points, connected by lines. This permits the user to view the motion of the payout eye relative to the mandrel. The result of the above definition produces the final strategy for winding the fiber filament around the mandrel during production. It is possible for the user to create a solid model representation of the fiber dispensing head using a number of cylindrical and cuboid primitives. In this mode the user can draw each position of the payout head around the mandrel for a particular payout path. The payout block and mandrel are either draw in wire-frame or solid mode. The head is rotated for the rotating eye and yaw axes. The fiber band is also drawn from the payout head to the mandrel.

Once the definition is complete, the user is ready for post-processing. The function of the post-processor is to convert the payout (.PAY) file into instructions (Numerical Control data) for the filament winding machine (FWM) in order that it may reproduce the designed fiber path on the surface of the mandrel. The NC data is produced in the form of a data file that can subsequently be transferred to the winding machine. Various post-processing options can be supplied (using up to 6 axes) dependent on the axis configuration of the machine and the nature of the winding to be undertaken. The winding can be divided into three main areas, these being: 1.Winding with a single tow, 2.Winding with multiple tows or 3.Winding with tape. The standard CADFIL post-processors are the '3 axis' and '4 axis' systems. The '3 axis' system is primarily for winding using a payout eye with a single tow (or perhaps a narrow tape), the 4 axis system is for use with multiple tows using a roller or comb payout system. The post-processor is independent from the path generation software and is configured specifically for particular customers. The various post-processing systems (e.g. 3, 4 or 5 axis systems) can be accessed from the NC Post Process option of the CADFIL main menu.

## 2. Computer Integrated Manufacturing Cell

To make a cell for an automated manufacturing system a Programmable Logic Controller (PLC), vision camera, robot arm, bar code reader, and C-more panel are integrated using a simple conveyor with stations. The PLC controls the system by sending signals to each machine. Three steel plates flow around on the conveyor belt. When a rectangular part on the plate having the bar code tag passes underneath the bar code reader, the system reads the bar code on the top of the aluminum automatically, and integers of the bar code is sent to the computer. When the product locates underneath the camera, a pneumatic switch blocks the plate in order to give the camera a short time to recognize the image and determine the product or if it has a defect. The camera sends the results to the PLC and computer software to decide if it needs rework and the PLC sends signals to a robot arm in the next step, the robot arm will put it on the milling machines to drill holes. A human can operate the entire process by using C-more panel which is connected to the system through the PLC.

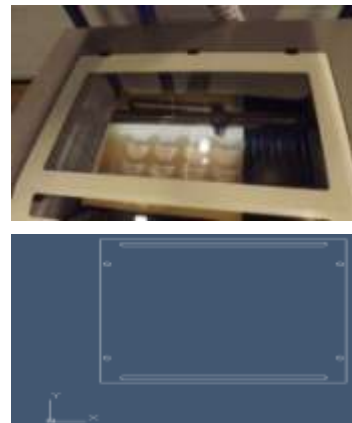


RoboRealm® is an application for use in computer vision, image analysis, and robotic vision systems. Using an easy point and click interface, RoboRealm simplifies vision programming. Image or video processing can be technically difficult. RoboRealm provides the software needed to get such a system up and running. It has compiled many image processing functions into an easy to use windows based application that operator can use with camera. RoboRealm offers to can see your robot's environment, process the acquired image, analyze what needs to be done and send the needed signals to your robot. It also it has an API (Application Programming Interface) in C, C++, C#, and Visual Basic so that it can communicate with other devices.



### 3. Hurricane 130W Laser Cutter/Engraver (48" X 36")

The laser purchased from Hurricane Lasers in Las Vegas, with a 48" X 36" work envelope and (150W) CO2 laser has been operating for over a year. Although we had a problem with the machine initially, it turned out to be to our benefit because we had the technician from Hurricane come to our facility and show us how to perform preventative maintenance and operate the machine/software used for cutting and engraving parts. We also learned how to focus and align the machine, as well as use the rotary attachment for engraving on cylindrical parts. The machine checked out fine and has been used to cut acrylic, wood, paper, leather, and other plastics. A picture of the installed Laser machine as well as the exhaust system for evacuating fumes, and the computer system are shown below here.



The laser system uses a simple design and programming interface called LaserCut5.3®. The software has a drawing pallet similar to Microsoft paint with tools for creating lines, arcs, text, etc. With this program, designs can be imported in standard formats such as .dxf, .bmp, as well as from programs such as Corel®. Using the geometry, the user separates the design into features. By changing the color of a feature such as a box, text, holes or complex shapes, the system recognizes the colors as separate operations. The control that the user has over each operation includes the type of cut (engrave or cut) as well as the processing conditions (similar to speed and feed-rate on a mill or a lathe). The parameters which are controlled by the user are the power and the speed of the cut. For different types of materials and material thicknesses the manufacturer provides a table of recommended values. Engraving is like etching the material and as the name implies, cut is used to penetrate completely through the material.



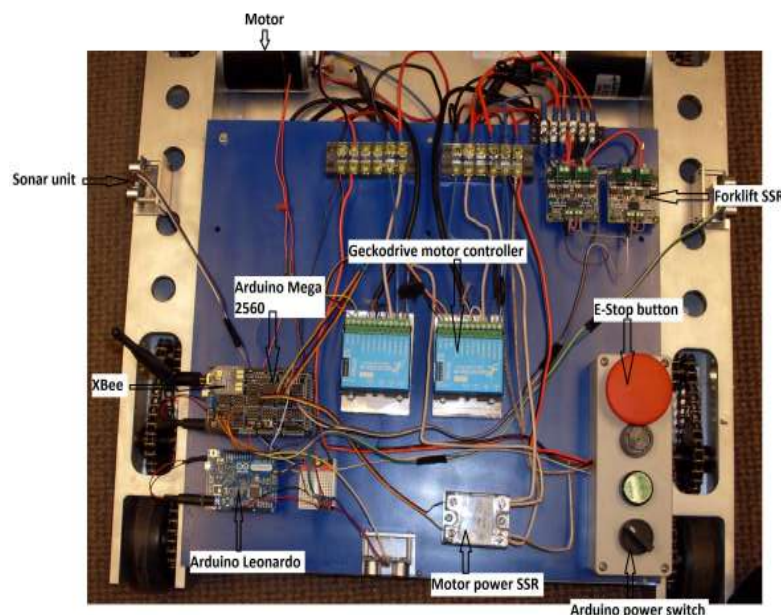
The laser has become indispensable for the engineering program at Oregon Tech. A complete conveyor system (body and components) were designed and manufactured out of ¼" acrylic, where the motors and drives were added afterward. There were also a group of senior project students that used the laser for multiple components of an assembly for a prototype knee prosthetic. The disks were all part of a fluid dampening system that represented a completely new idea in designing and building prosthetic replacements for joints and articulations. One of the capabilities of the laser is to etch lettering, logos and decorations on parts that have either been painted or powder coated. Using this feature, students have been able to produce high quality parts that look like they were done by professionals. Visitors to the labs and customers of projects done on campus often comment on the impressive results.

### 4. Mobile Robot Development and Vision Systems for a Smart Materials Warehouse

For material handling purposes, it is convenient to use robots that can move freely throughout a given space. This is usually done using automatic guided vehicles (AVGs) that use markers imbedded in the floor to determine location and path. This research project attempts to do something different by utilizing mobile robots that will be used in a warehouse setting and be guided and monitored by either remote computers (wireless) and onboard or ceiling mounted cameras using a customized software interface designed using Microsoft Visual Studio® and the C-Sharp (C#) programming language. The project is made up of several parts that were developed independently and then integrated together to demonstrate the Smart Material Warehouse concept. This section will describe the main parts: 1) Robot construction and control, 2) The “eye in the sky” ceiling mounted camera and software developed in Open CV® (called EMGU CV) and 3) The 3D image processing / obstacle avoidance system using the Kinect vision camera technology from X-Box video games mounted on a mobile robot.

Four robots were designed and built for use in the warehouse application. They are similar but have different capabilities and functions that are performed. Each is based loosely on the IRobot platform that has been used in many consumer and military applications, including the Roomba vacuum cleaner and floor cleaning systems, models that can be used to clean swimming pools and gutters and multiple models for infantry and special operations missions including building clearing, raids, dangerous conditions, bomb disposal and a bigger model for heavier payloads.

To have a variety of building options, the Oregon Tech group purchased 4 BattleBot kits that came with motors, mounts, batteries, controllers, wheels and a heavy duty platform included. The team used the kits to develop 2 of the 2-wheel models that were very maneuverable and 2 of the 4 wheel versions that were more robust and could carry significant payloads. The technology that was integrated into the mobile robots included digital motor controllers, programmable micro controllers, sonar, and wireless serial communication. A radio frequency identification (RFID) reader, a liquid crystal display (LCD) and a linear actuator utilized as a forklift were also added to some of the robots to demonstrate material handling and product identification for routing.



The robots have had several capabilities built into them. Some of the robots have different functions and therefore have different equipment and functionality. All of the robots are capable of wireless serial communication, forward and backward linear motion, and turning around the center point between the two primary drive wheels. All of the robots use Zigbee XBees for wireless serial communication. The serial communication allows for commands to be sent and feedback to be received using text. Forward and backward motion are achieved by sending the text command “P+” or “P-” (respectively) followed by a distance in mm over the wireless serial connection.

The code that was developed for the Arduino receives the command and compares it to a list of commands that have been set up in the code. Turning is achieved in much the same way, but using different commands. SmallBot and BattleBot were built with only these basic capabilities. More functionality has been added to them by their respective software teams. This has been done using additional equipment such as cameras and additional software run on either a laptop or a desktop computer. The additional capabilities that have been added to ProtoBot and LiftBot could be added to SmallBot and BattleBot at a later time. ProtoBot and LiftBot have both been equipped with sonar. Parallax sonar units have been mounted facing in all four directions on both robots. The sonar units use sound to measure the distance to the nearest object that is in front of them. The sonar is operated by a separate Arduino microcontroller than the one that controls other robot functions. If the sonar detects an object that is within a set distance from it, it will signal the primary Arduino. This command is sent by changing certain digital output high>low. The primary Arduino stops its motion to avoid a collision.

ProtoBot has also been fitted with an RFID reader and an LCD screen. The RFID reader is powered by and communicates with the control Arduino. When an RFID tag is read, the Arduino receives the tag number over wired serial communication. The tag number is then displayed on the LCD screen and sent over wireless serial communication to the command computer. LiftBot has had a linear actuator mounted on the front of the robot chassis. This actuator has a forklift mounted to it. This robot is meant for material handling. The fork is operated using four power relays to control the polarity across the motor leads. The relays are controlled by the primary Arduino using the commands “LU” and “LD” to move the forklift up and down respectively for a specified number of seconds.

To control all of the onboard robot functions, an Arduino Mega 2560 microcontroller is used. The Arduino Mega has 54 digital input/output (IO) pins. 15 of those pins can be used for pulse width modulation output to simulate analog output. It also has 16 analog inputs, 4 serial communication ports, and a 16 MHz Oscillator [6]. A sensor shield is being used to make the wiring of the robot simpler. The shield is made by DF Robot and separates the power and ground leads so that each IO pin has in its own power and ground. The sensor shield also has a place to directly connect the XBee. The XBee is what is used for wireless serial communication. The XBee has a 2.4 MHz transmitter/receiver and is fully user configurable using the Digi International software X-CTU. X-CTU is free to download from the web site “<http://www.digi.com/support/productdetail?pid=3352&osvid=57&type=utilities>.”

An Arduino® Leonardo microcontroller is used to operate the sonar units. This Arduino only has 14 digital IOs and is much smaller and cheaper than the Arduino Mega. The reason the second Arduino was utilized was because the sonar operation requires that the Arduino send out a sound pulse and wait for the sound to return. This causes interference with the motor operation because it relies on delays as well. Geckodrive® G320x DC servodrives are the motor drives that are being used. They are capable of delivering 20A to the motors at a range of 18V to 80V DC. The motor drives have connections for a power source, the motor leads, the motor encoders, the direction pin, and the pulse pin. The direction

pin is used to change the direction that the motors will turn. The pulse pin is used to control how fast and how long the motors will turn.

The encoders that are used are AMT 103 incremental encoders. Using the built-in dip switches, the encoder can be adjusted from a resolution of 48 to 2048 pulses per revolution (ppr). These encoders require a 3V to 5V power supply and are connected directly to the Geckodrives. A solid state relay (SSR) has also been added to the system. This motor relay is used to turn the power to the Geckodrives on and off. The motor relay is controlled by an IO pin on the Arduino Mega and is rated for 30A DC. There is also an industrial switch box that contains an emergency stop (E-stop) button, a charging port, a power light, and a power switch. The E-stop button is wired in series with the positive side of the motor relay so that all power to the motors can be stopped if needed. On LiftBot the forklift power supply is routed through the E-stop button as well. The power light and power switch are connected to the 12V power supply that is used to power the Arduinos.

LiftBot has some additional control hardware due to the need to power the forklift. Two dual SSR boards made by Phidgets® were added to the robot for this purpose. The motor for the linear actuator that is used for the forklift is a 24V DC motor. The motor direction is controlled by changing the polarity across the motor lead. There are also two limit switches built into the rail of the linear actuator. Activating either one of them will cause an open condition across the limit switch leads. The problem of making the fork move up and down was handled by connecting the forklift power supply to each set of SSRs the same way. The positive lead is connected to one of the SSRs and the negative is connected to one side of the other SSR on the same board. The red motor lead was then connected to the other side of the SSR that was already connected to the positive power lead and the black motor lead was connected to the other side of the SSR with the negative power lead. This way when both SSRs on the board are turned on, a circuit is made. The other board is set up the same way except that the motor leads are reversed. On the control side of the SSRs, all of the negative sides are connected in series and run through the built in limit switches. This will cause fork motion to stop as soon as either one of the limit switches is activated. In addition the positive sides of the SSRs on each board are jumpered together. This allows the SSRs on each board to be turned off and on with a single wire. A 5V signal from the Arduino Mega is used to activate the SSRs when the fork is operated.

The Parallax sonar units use a three pin setup for operation. The 5V and ground are used to power the unit, while the third pin is used as an input and output. When the IO pin is turned on by the controller, the sensor sends out a 40 KHz sound pulse. Then the IO pin waits for 750 micro seconds ( $\mu$ s) then turns the IO pin high until the sound is reflected back to the sensor. The sensor has a maximum range of about 3 meters. As mentioned before, LiftBot used a linear actuator to raise and lower the fork. The linear actuator is made up of a 24V DC motor that drives a lead screw. The lead screw is housed in an extruded aluminum beam. A custom made fork has been attached to the beam in a way that it can be driven up and down by the lead screw. Two braces have been welded to the back of the beam cap and are used to support the top of the beam. Figure 8 shows the forklift with its components labeled.

The RFID reader uses induction to power the transmitter that is embedded in the RFID tag. Once the transmitter is powered, the tag sends the tag number back to the reader by radio transmission. The RFID reader that was used for this project uses serial communication to send the tag number to the control device, in this case the Arduino Mega. The Arduino Mega uses a 5V IO system but the RFID reader uses a 10V system so an adapter circuit was built on a small breadboard that was mounted on the robot. All of the components for this circuit came in the kit with the RFID reader and the instructions to build it were



found on the following web page "<http://www.robotshop.com/content/PDF/schematic-pr8.pdf>." The schematic on this page is also shown in appendix C and was used for connecting the LCD screen as well. The RFID reader and the LCD screen both required some soldering before they could be used. The reader had a cable that needed to be cut and the individual pins had terminals soldered to them. The LCD screen needed a row of pins soldered onto the integrated circuit (IC) board. The instructions [9] were followed on how to connect these devices. The small breadboard was used again to allow for a potentiometer to be used to adjust the LCD screen brightness.

Code was developed for several different applications as part of this project. The bulk of the programming was done using C++. This code was written for the Arduino micro controllers using the Arduino programming environment that is available on the Arduino web site "<http://www.arduino.cc/>." Entirely different programs were written for the Arduino Mega and Leonardo. The main control code that goes on the Arduino Mega has also been altered for each robot depending on their geometry and onboard functions. Microsoft Visual Studio was used to create a GUI for manual operation of the robots. This code was written using C#. The basic structure of an Arduino program consists of two void subroutines. The first is called void setup and is run once at the beginning of the program. This void can contain any valid C++ commands including calling functions or other subroutines. As its name implies, it is usually used to set up variables, set initial pin modes and values, and initialize things like serial communication. Void loop is the second subroutine that must be in every Arduino program. It always comes after void setup and it runs over and over until the microcontroller is turned off or reset. Void loop is generally where most of the code goes. Due to its cyclic nature, routines and functions can be placed in here to be run in order many times. This is ideal for monitoring multiple sensors or just waiting for text to come in over a serial connection.

The Arduino control code that is used for all of the onboard robot functions except the sonar was already begun when this project started. The original code consisted of routines for serial communication, adjusting settings such as velocity and acceleration, turning the motor power system on and off, and linear forward and backward motion. Several variables were declared before void setup, which makes them public and therefore usable in any routine. The define command was also utilized to name the IO pins. The structure for the define command is as follows: `#define constantName number`. This method replaces any mention of "constantName" with the value of "number" when the code is compiled. With the exception of one user defined function and the variable declarations, all of the original code was contained in the setup and loop voids.

One of the first things done was to make this program more modular. Void setup was left with the same structure although a lot was added to it by the time the program was complete. However, the contents of void loop were replaced almost entirely with a series of function and routine calls. A few condition statements were added to help control the flow. The rest of the contents of void loop were moved into separate functions and routines that were called from void loop. This made the program much easier to work with and modify throughout the rest of the process. One of the other major changes that were made to the original code was to change the technique for controlling the robots velocity. The original method calculated the amount of time that it should take to accelerate and decelerate as well as the time at constant velocity. The program then made sure that the motors were performing those actions for the proper amount of time regardless of the distance that was traveled. This method did not provide accurate positioning.

Motors are controlled by sending signal pulses to the motor drivers. The motor drivers then send power to the motor. Each signal pulse that is sent to the motor drivers is turned into one unit of rotation of the

motor. The unit of rotation is dependent on the encoder setting and the Geckodrive settings. For the setting used during this project there are 819 units per complete output shaft rotation. The robot velocity control was altered so that the number of pulses needed during acceleration, deceleration, and constant velocity were calculated. Then the condition statements that determine what the robots acceleration state is, is based on the number of pulses that have been produced. This allows the positioning of the robot to be much more accurate. Routines were added and modified to allow for separate settings to be assigned for linear and turning motion. This was done because the suitable turning speeds are much lower than the practical linear speeds. In order for the robot to move at a reasonable pace in a straight line, the velocity setting needed to be set such that for turning the robot would move too fast to maintain traction. This meant that position accuracy was lost. The method that was used was to add variables to store the values for linear velocity and acceleration and turning velocity and acceleration. In the commands function, depending on the type of motion the relevant velocity and acceleration is saved to the variable that the movement routine uses and applies.

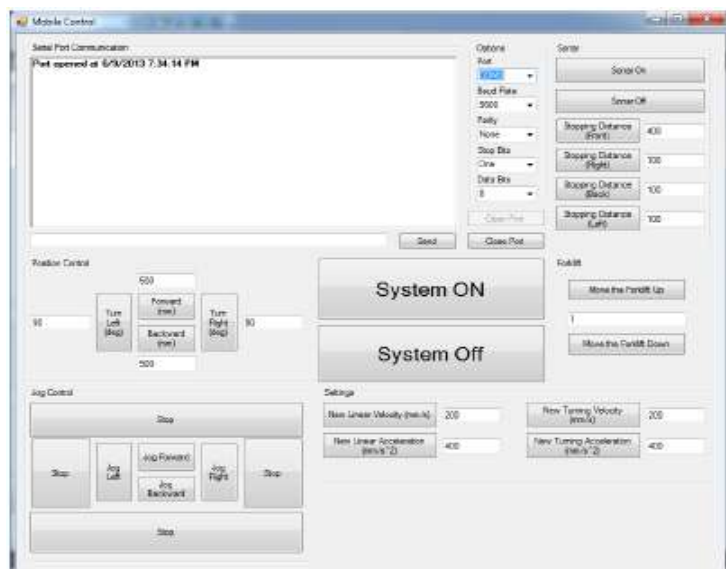
The Arduino Mega has four built in serial ports available. A second serial port was utilized for communication with Arduino Leonardo. This communication allows the settings for the sonar units to be change from the Arduino Mega. The Arduino Mega can be commanded over the wireless serial connection to command the Leonardo to change the setting. There was a problem with this Arduino to Arduino connection initially. The first communication would be handled perfectly but every subsequent communication would be ignored. The text would be received and passed to the routine that determines what the command is. But the command would never be executed. This problem was finally solved by using the built in function "trim." The trim function is used to remove any leading and trailing spaces from the string. This cleaned up the command and allowed the routine to recognize it.

On the ProtoBot a third Arduino Mega serial port was utilized. This one was used for communication with the RFID reader. The incoming string is collected the same way for the RFID reader as it is for the other serial ports, but because the information does not need to be sent to the commands function, the whole process can be handled in the serial communication routine. Once the string is collected it is simply sent to the command computer over the wireless serial connection. It is also sent to the LCD screen using functions from the LiquidCrystal library that comes with the Arduino programming environment. Again, specifically for ProtoBot, the LiquidCrystal library was used to operate the LCD screen. To use a library the user must include it into the code. This is done by typing "#include <libraryName.h>" (where libraryName is the name of the desired library) at the top of a program before void setup. This allows the user to access any of the functions that are part of that library. In this case, LiquidCrystal contains functions to turn the screen on and off as well as clear and write to the screen. The LiquidCrystal library also requires that the user define the Arduino IO that will be used to operate the LCD screen. It should also be mentioned that this library only works for certain types of LCD screens.

Programs on the Arduino Leonardo handle all of the sonar operation. The code that is used to take a measurement using the sonar was taken from the Ping example that is included with the Arduino programming environment. This code was modified to only provide measurements in mm. Then the code was integrated into the program for operating all four sonar units. This program was started very similarly to the control program. Some variables are declared at the beginning along with some define statements for the IO pin constants. Void setup is used to start serial communication, set the IO pin types as ether input of digital output, set the output pins initial state, and set the initial state of some variables. Void loop contains primarily function calls with some condition statement.

This code was built in a modular fashion and uses some of the same functions as the control code. The serial communication routines are identical and the commands routine uses the same structure that is used in the control code. The functions that were written specifically for this project are SonarCycle and Distcheck. SonarCycle uses a case statement to cycle through the four sonar units. The current sonar pin is used as the argument of the function. The case statement determines what that pin is and cycles to the next sonar pin. Distcheck is used to compare the distance value that was calculated for the last sonar unit that was pinged to a preset minimum distance. If the distance is too close, two output pins are set high. This signals the control Arduino to stop any motion that it is currently performing. The serial communication with the control Arduino can be used to change the minimum allowable distances over the wireless serial communication from the control computer. The sonar can be turned on and off over the serial port as well. To do this, a designated input pin is set to high or low.

The control GUI was written using Microsoft Visual Studios software, and the C# programming language. The free software that is used to handle serial communication was created by Richard L. McCutchen and is called PCComm.SerialCommunication Version 1.0. This code was modified for the purpose of this project by removing unneeded portions. The portions that were removed primarily involved the type of transmission, ether hex or text. This code was removed to simplify the program and because the transmissions for this projects purposes would always be text. There was already a GUI portion associated with PCComm.SerialCommunication. The original GUI consisted of a serial monitor that included a window to view serial messages and text box for entering messages that were to be sent. It also included dropdown menus for selecting the serial port and other serial options. For the purposes of this project, this GUI was expanded and modified. Many buttons were added to control the specific robot functions. For the click of each button a command is built based on what button was clicked and any text boxes that are associated with the button. The command is then sent over the serial connection to the robot. The figure below shows the completed robot control GUI.



Many of the principles and technologies used in this project, for the mobile robots, are very different from what would be used for a robot with a fixed base. Because the robot can only move on the floor, the robots location only needs to be determined in terms of X and Y position. The math involved in this process is much simpler than the matrix math required for determining tool location on an articulated arm robot. However, the mobile robots do not have a fixed reference point to base their current

location on. This means that complex algorithms are needed to locate the robot and find its position in relation to any obstacles or its destination. The mobile robots are also required to be more aware of their surroundings. For a standard articulated arm robot, the entire work space can be taken into account when the robot is programmed. In the smart warehouse scenario, there could be multiple dynamic pieces of equipment, material, and personnel in the same work space. The onboard sensors and camera provide the capability for the robot system to constantly monitor their environment and make changes if needed. The skills that were developed during the course of this project include C++ programming, C# programming, interfacing microcontrollers with other hardware, electronics networking, and electro mechanical controls design.

The existing robots could also be interfaced with other robots such as articulated arms. In this way they could be used as part of a completely automated manufacturing demonstration. Additional capabilities could be added to these robots to allow them greater mobility. More functionality could be added to the Arduino to allow for multiple commands to be received in one transmission. The robot could then execute the commands one at a time. Additional communication routines could be used to allow for control of multiple robots simultaneously. These types of systems could eventually be used for military applications such as search and rescue, warehouse management, munitions management, arming and disarming of military vehicles, and in medical facilities for deliveries.

Once the robots were built and tested, they were ready to be used in a warehouse environment. Computer Software Engineering Technology (CSET) students were tasked with developing a robotic system that utilizes an “Eye in the Sky” camera and software developed using EMGUCV (the C# version of OPENCV) to detect robots in a manufacturing materials warehouse, locate them and identify pathways and obstacles on the floor. With this specific type of mobile robot, called Automatic Guided Vehicles (AGV’s), materials, tooling and resources can be transported with very little human interaction. The custom built AGV’s are being equipped and integrated with vision systems to demonstrate autonomous control, guidance and surveillance capabilities. As a standard working scenario for this research project, the small robots must transport materials to be stored, moved, processed and delivered to students completing projects in the machine shop using lathes, mills, drill presses, grinders etc. A 3D image of the warehouse and a picture of the actual work environment are shown below.

### 3D Model of Smart Materials Warehouse Designed in Solidworks



Scenario for Presentation: Raw materials are received from the supplier and they are subsequently cut and shaped into blanks that students use for their MFG120 machining projects.

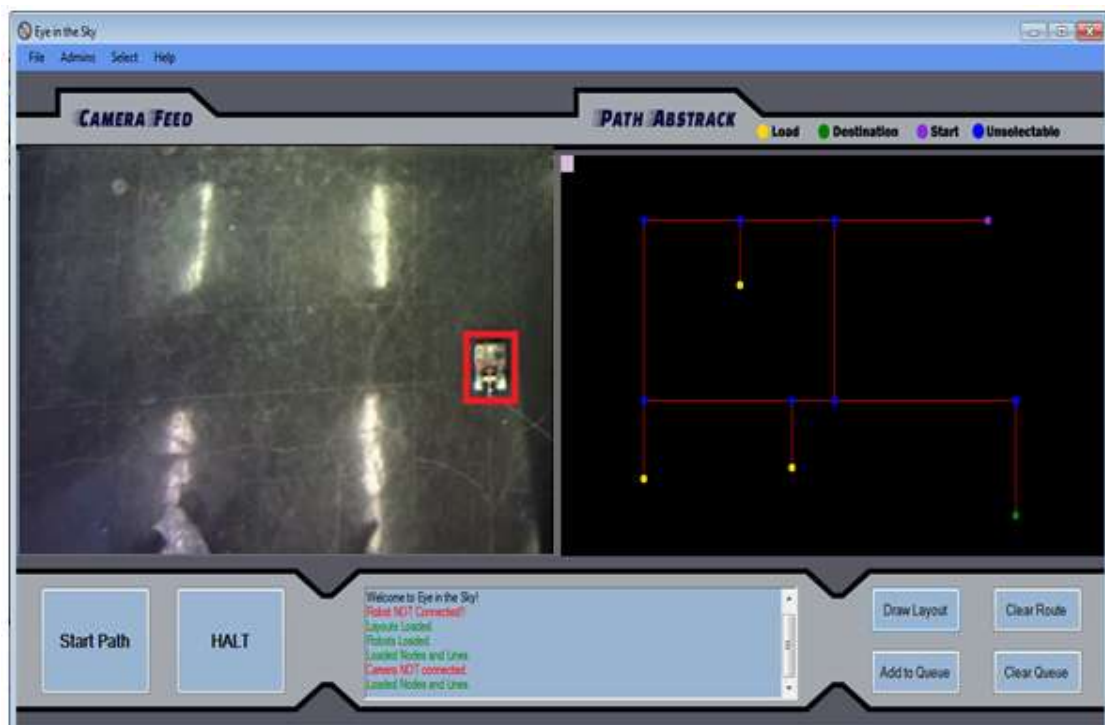
### Work Environment at University Engineering Department



The user, through the central control station will command the robot to leave the robot docking stations, move over to storage to be loaded, then proceed to each of the required stops in preparation, then deliver to a load/unload robot at the staging stations. After completion the robots may also be available to take orders to shipping, where it will then be handled by other staff. To accomplish this, it was necessary to model the working environment, take into account the current layout of storage, machines and tables to create scenarios typical to material flow through the warehouse. After processing the live footage, the system provides feedback to the main control center that then commands the robots to deploy where they are needed and load/transport the raw materials across the warehouse floor. Aside from the numerous skills that the students gained during the project, it is also a great example of how engineers from different disciplines and diverse backgrounds must work together to solve problems facing industry. The 5 main objectives associated with the system of the team were:

1. The system must be able to take a live footage from the ceiling mounted cameras.
2. The system must communicate with the central control and move the robot.
3. The system shall be able to determine a path for the robot to follow on the manufacturing floor.
4. The system will allow the user to view the live footage from the ceiling mounted cameras, determine robot start and end points, and monitor the robot.
5. The system will store data during runtime in a specific format in the database.

The screen image below shows the robot being tracked by the ceiling mounted camera on the left side and the path development interface on the right hand side. Based on the path, motion (motor) commands were sent wirelessly to the robot and it would move through the warehouse and stop at the stations needed to process the raw materials. CSET students working with the Kinect® cameras were able to move their robot to locations around the floor and stop when an obstacle was encountered. The video feed was displayed on the computer screen and general shapes identified (for example a human, machine or a pallet). CSET faculty members were pleased with the results of the work done by students.



## 5. Fanuc Robotics CERT Training Site status for Oregon Institute of Technology

One of the fastest growing and most popular areas in all of engineering is robotics. In addition to the traditional applications in manufacturing such as welding, painting and material handling, robots are now being used in everything from medical procedures to space exploration, and for making aerospace parts using composite materials. A unique aspect of robots is their ability to capture the attention of people from all ages and walks of life, especially kids and young perspective engineering students. Many programs such as Lego, FIRST, Project Lead the Way and VEX are being used around the world to introduce more and more people to the world of robotics. Oregon Tech currently does a good job and has the potential to be a regional leader in robotics education for many reasons; 1) various programs use robots in some part of their curriculum (Mechanical, Electrical, Manufacturing, Software), 2) there are faculty members with the expertise to work in areas such as robotics theory, construction, operation and programming and, 3) we have the labs, technology and equipment to grow our program and facilitate multi-disciplinary learning and work with industry people on collaborative projects.

One of the most exciting developments that resulted from this work is our inclusion in the nationally recognized CERT program, a network of training centers sponsored by the world leader in robotics, FANUC Inc. We currently have 2 5-axis robots with vision capabilities that are worth about \$35K each and a larger model that is comparable to the biggest and best found in industry. During a recent visit from the regional educational director for Fanuc, Tom Diehl, he stated that "Oregon Tech has one of the best equipped labs that I have seen in the region". He further commented on the possibility of becoming the selected regional training center for FANUC by completing the implementation of the complete and standardized FANUC program of study (including E-learning materials, robot simulators and interfaces with other devices).



Oregon Tech now has instructors that have completed the 4 day workshop offered at one of their five regional training centers. After visiting Klamath Falls and learning that we have all of the equipment needed, FANUC offered to train 2 instructors for \$6000.00. In addition, the other materials including manuals, 10 E-learning packages for our students and 5 licenses for the simulators were provided for \$1000.00 more. The funds provided by the Commission on College Teaching were combined with an Army Research Labs grant and a contribution from the MMET department and the Dean's office to complete this very important project.

**Handling Tool Operation and Programming**  
**32 CONTACT HOURS (3.0 CEU)**



The course covers the tasks that an operator, technician, engineer or programmer needs to set up and program a FANUC Robotics Handling Tool Software Package.

Course Code: J2P0310

Course Objectives: Students successfully completing this course will be able to:

- Power up and Jog the Robot
- Recover from common program and robot faults
- Execute production operations
- Create, modify and execute a material handling program
- Create and execute MACROS
- Monitor, Force, and Simulate Input and Output Signals
- Backup and restore individual programs and files



**FANUC**  
ROBOTICS  
CERTIFIED  
EDUCATION  
ROBOT TRAINING

Recommended safety procedures are integrated into all training exercises.

The course consists of lectures, demonstrations, and a series of lab exercises designed to reinforce what the student has learned.

In addition to lab exercises, a pretest and posttest are used to measure mastery of objectives.





## 6. ShopBot 3-Axis CNC Wood and Foam Router

The tremendous need for a large CNC machine for cutting softer materials such as foam, wood, plastics, etc. has been growing for the last few years. Projects are slowed and simplified drastically when composite molds have to be made by hand. This is why an economical, sturdy, reliable router was purchased to fill this urgent need for our composites lab and classes. Projects such as fairings, car bodies, covers and bike molds produce a higher quality product in many ways for both student work and faculty applied research. The router chosen has an 8' x 4' x 18" (x,y,z) work envelope for deep cuts and has good rigidity for cutting woods, high density foam or plastics. It has also been integrated with our current CAM software program by creating a customized post-processor that generates the specially formatted NC code.



## 7. Teaching Stations for Stepper / Servo Motor Control

Two learning stations were designed and developed for students at the beginning of the ARL project. These stations demonstrate many of the basic building blocks that were used later on robots and CNC machines. The first is a stepper motor system controlled by a PLC and the second is a servo motor system also controlled by a PLC. Using these systems students can be taught about motor controls, basic ladder logic programming, wiring of components, motor pulses as they relate to linear motion and the use of encoders in feedback acquisition. Since many of the automated components used in this project used these types of motors, it was important to begin with a simple teaching device before moving on to more complex systems such as robots and CNC machines. These stations remain in the robotics lab and are being used in undergraduate courses.





**Appendix 1: Vision Course Paper Presented at ASEE 2013, June 22 (Atlanta, GA)**



**120th ASEE Annual Conference & Exposition**  
FRANKLY, WE DO GIVE A D\*MN  
June 23-26, 2013

Paper ID #6615

---

**A Proposal to Implement a Course on Vision Systems with Applications in Robotics at the Oregon Institute of Technology**

**Mr. Matthew Floyd, Oregon Institute of Technology**

**Mr. Hoejin Kim, OIT**

**Dr. David E. Culler, Oregon Institute of Technology**

M.S. and Ph.D. in Industrial Engineering from NMSU, 1995 Specialist in CAD/CAM integration and product development Currently Associate Professor, MMET, Oregon Institute of Tech.

# **A Proposal to Implement a Course on Vision Systems with Applications in Robotics at the Oregon Institute of Technology**

## **Abstract**

Robotics, material handling systems, surveillance, object recognition, and component inspection in manufacturing are just a few of the areas where cameras and vision technology are being combined to design new processes and update existing ones. A problem arises from the wide range of skills and knowledge related to the mechanical set-up, electrical controls and software required to develop and successfully implement these systems. A class that introduces students to this subject matter so they can do projects and work in an industry setting is needed.

This paper proposes a course program of study that will be used to introduce Manufacturing and Mechanical Engineering Technology students to vision technologies at Oregon Institute of Technology in Klamath Falls Oregon. The main focus of this paper and what differentiates it from other proposals is that it identifies software and computer programming as one of the major barriers that keep Manufacturing and Mechanical Technology students from learning about vision systems and their use in automated/ robotic/ manufacturing applications.

Many lessons have been learned through collaborative projects with the computer science and computer software engineering students/faculty. In the past, MET and MFGET departments have worked on aspects of the projects and then turned them over to the computer department for software development. The authors take the approach that introductory “canned” programs can now provide basic functionality and tools, while some libraries of “code” functionality can be found on manufacturer’s web sites and user forums. Finally, pure development of applications is available in a variety of applications programming interfaces “API” languages including Visual Basic, C++, C#, and others.

The expected benefits of this course are to provide a language and concept bridges that will allow more ET students to participate in the design and implementation of systems in conjunction with engineers from other disciplines. With the foundation built from this course and previous projects, the department will be able to grow and expand on the work completed each year. There is a need in industry for Mechanical/Manufacturing engineers and technologists with interdisciplinary skills and experience that they get as part of their college education.

## **Literature Review**

Robot vision is a rapidly growing segment of robotics and computer engineering with application in numerous fields. It can be utilized in any situation where human vision is currently used. This field currently has many limitations, but improvements are being made on a continuous basis. Some of the primary areas of interest are Surveillance, inspection, obstacle avoidance, and guidance.

A lot of the work being done in the area of surveillance is focused on reducing the amount of processing power needed to do high quality object tracking and recognition. This allows for

lower power consumption needed for mobile and small scale applications [1]. It also means that these systems can be produced more cheaply.

Automated visual inspection is something that is already being used in factories and processing plants. It allows for high speed inspection of every part where traditional inspection methods would only inspect samples of the product. Larger scale inspection is also being developed for bridge applications [3]. These same methods could be adapted for use in all kind of industrial and structural inspection situations where safety and consistency are concern.

Obstacle avoidance and guidance are closely related areas that are applicable to mobile robots. Guidance looks at the big picture and navigation from one point to another. Some specific applications are UAV guidance [4]. Many existing vision guidance systems rely on artificial markers for location purposes, but work is being done to develop ways of recognizing natural land marks for guidance purposes [4]. Collision avoidance deals more with small scale avoiding unexpected objects in the current path. Some of the work in this field involves systems that mimic insect nervous systems [2] because of their simplicity. These systems use relatively simple algorithms and hardware to avoid approaching object that are in the robot's path while giving very little reaction to objects that are in near collision positions[2].

The following is two more specific examples of how machine vision is being used. *An Autonomous Robotic System for Inspecting Substation Equipment* [5] presents Smart Guard, a completely autonomous robotic system that can inspect substation equipment. The vision based navigation system is applied when the robot patrols in a substation and inspect substation equipment. The method for inspection of substation equipment is to first analyze images and determine the ratio of distance, second is to compare current images to a reference image and to look at temperature using an infrared camera and match the two images.

Success in navigation requires success at the four building blocks of navigation; perception, localization, cognition, and motion control. In order to make these possible for navigation, it mentions three methods of navigation; magnetic guidance system, the integrated GPS-DR Navigation, and the omnidirectional Vision System. The omnidirectional vision system uses a camera installed on the robot to recognize four kinds of patterns or landmark which have different information and move forward following landmarks along the side of a road. Visual navigation may be a good way to reduce cost in the future, but there is still a lot of work needed to improve the positioning accuracy.

*An Autonomous Mobile Robotic System for Surveillance of Indoor Environment* [6] presents autonomous mobile robot used for surveillance of indoor environments by autonomously navigating with a monocular camera, a laser scanner, and an RFID device. For this surveillance vision system, laser-based mapping, safe navigation, global localization, and path planning are introduced. After area mapping is completed by using RFID Tags, the robot analyses the scene searching for abandoned or missing objects, RFID tags provide information about the surrounding region or instructions for the robot to perform a certain task. The proposed approach assumes that RFID tags are distributed throughout the environment, along with visual landmarks. As soon as a tag is sensed, the bearing of the tag relative to the robot is estimated. Bearing information is then used to trigger a rotational movement of an onboard camera, so that it is oriented toward the visual landmark associated to the tag.

There are two way for this system to recognize objects in the indoor environment. The first is to recognize abandoned or missing object detection by comparing the position of predefined objects or the presence of new ones, and the second is to use laser-based people detection and follow any intruder by reacting with predefined actions.

## **Introduction and Background**

Machine vision is an area of industry that is growing rapidly and working its way into many engineering fields. The use of machine vision for guidance and inspection in manufacturing and assembly plants makes it necessary engineering technologists to have at least a basic understanding of the their function, capabilities, and limitations. This paper will outline some tools and methods that would be useful for teaching college undergraduates, studying engineering technology, how to use and program robotic vision systems. It will recommend an inexpensive kit that could be purchased for teaching the basic skills. A course outline will also be developed for a quarter system class that would provide basic understanding of the technology being used in industry.

The information in this paper will be largely based on the experience of the authors who have been doing graduate work in the field of robot vision from the perspective of Manufacturing Engineering Technology. The focus of this work was in the area of part inspection and automated material handling guidance systems. Many off the shelf products were used to develop basic systems for the identification of parts and part features using machine vision. Obstacle recognition and path planning was also performed using readily available software.

Software and computer programming knowledge are essential for implementing vision systems in a manufacturing environment. The main focus of this paper and what differentiates it from other proposals is that it identifies software and computer programming as the major barriers that keep Manufacturing and Mechanical Technology students from learning about vision systems. The first hurdle to teaching engineering technology students is making them familiar with a suitable software package. With an introduction to simple and inexpensive software and hardware, students can then explore the capabilities and limitation of machine vision.

## **Hardware**

The camera is regarded as an eye of a robotic system, and is meant to capture an image and send it to a computer. The camera can be anything from the web cam on a laptop computer to a cell phone camera or digital still camera to a high end industrial camera. In most situations, a camera that can stream video would be used. Another consideration is that the higher quality resolution and sensitivity the camera is capable of, the better image recognition the system will have.

In some situation, the camera might be mounted far away from the objects, while others might require close up capability and still others might require weather proofing for outdoor use. When choosing a camera it is important to take all of the requirements into account. When it comes to lens, again, there are a variety of camera lens that can be used depending on the situation. To connect the camera to the computer, there are many options such as wireless, high definition

cables, and USB cables. Each type has its own advantages and disadvantages, so depending on the situation and the type of camera, the kind of cable can be selected.

The computer that will be used is the next consideration. Again this will depend greatly on the application of the system, and some of the consideration for this are; will the system be mobile, will the computer need to be running other applications at the same time, what kind of image processing will be done, and what kind of environment will the system be operating in? The primary concerns when choosing a computer to perform image processing are the amount of RAM and Processor speed.

## **Software**

Once a vision system has acquired an image and sent the data to the computer, a program is needed to perform target Acquisition, Recognition, and Analysis. These processes should be accomplished quickly and accurately to ensure proper function of the system. The image processing software should also be able to communicate with other program through an Application Programming Interface (API) so that actions can be taken based on what the vision system sees.

These are three kinds of representative vision application software for the image processing. OpenCV, called Open Source Computer Vision Library, is a library of programming functions mainly aimed at real-time computer vision, and has libraries for C, C++, C#, Visual Basic. It can be downloaded from Internet for free. One disadvantages of OpenCV is the fact that it requires a lot of knowledge and skills about C languages to build programs.

Halcon, which is commercial software, is the comprehensive standard software for machine vision with an integrated development environment (IDE) and is used worldwide. It provides the solution for the full range of applications in the field of machine vision and board, wafer & die inspection, medical image analysis, automotive and robotics, surveillance, and remote sensing. It also offers various language interfaces, such as a C++ and a native .NET interface. Using these interfaces, an operator can access all of HALCON's more than 1800 powerful functions from programming languages such as C, C++, C#, Visual Basic. Some disadvantages of Halcon are that it is expensive because it is a commercial product and it requires an operator with significant programming knowledge.

RoboRealm is a simpler software package for use in computer vision, image analysis, and robotic vision systems. Using an easy point and click interface, RoboRealm drastically simplifies vision programming. Image or video processing can be technically difficult. Homemade robots are continuously moving towards PC based systems (laptop, netbook, embedded, etc.) that have the power to support complex image processing functions. RoboRealm provides the software needed to get such a system up and running. It has compiled many image processing functions into an easy to use windows based application that operator can use with any digital image. RoboRealm acquires images of the robot's environment, and process the image, analyzes what needs to be done and send the needed signals to your robot's motors, servos, etc. It also has an API function for access to and from C, C++, C#, and Visual Basic that can make a possible to communicate with other devices. Some advantages of RoboRealm are that it requires little programming skill to operators due to the built in functions, and it only costs about \$50.00.

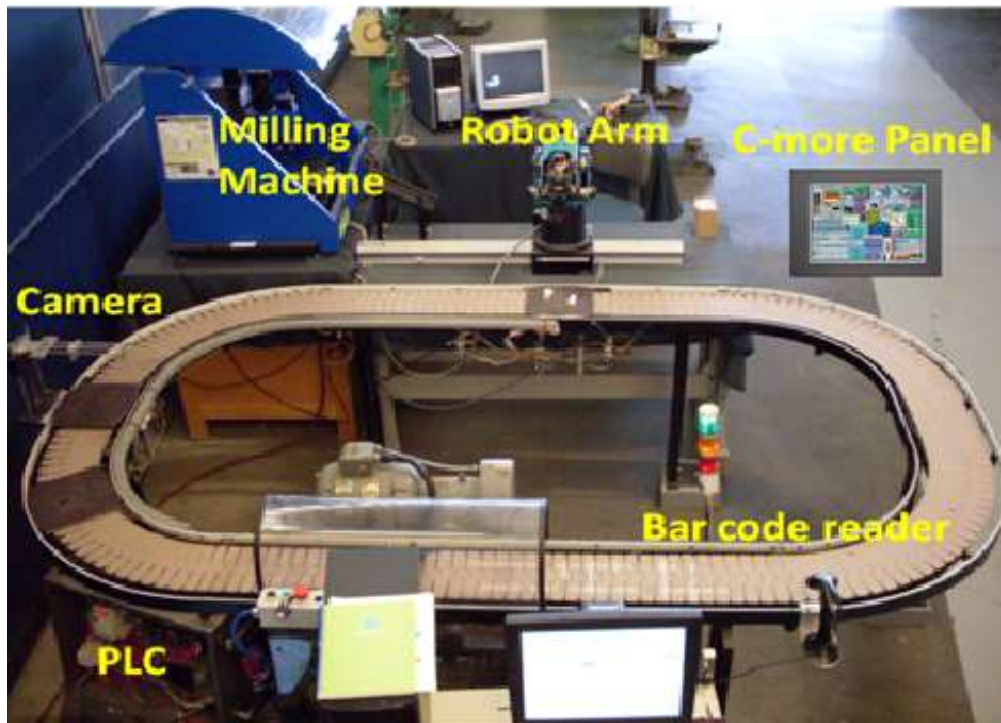
Imaging source software, which is called IC Imaging Control and made only for image acquisition using imaging source cameras, provides the operator with function and an API between C language and camera. This function in the IC Imaging Control is composed of basic things such as scroll/zoom, image capturing, saving, manipulating, image sequence, timestamps, and triggers which support programming environment such as C, C#, C++, Visual Basic.

## **Industrial Application Examples of Vision System**

Vision systems are widespread and have been utilized in industry to increase the productivity. For instance, in the semi-conductor industry most products are complicated and too small to recognize with the naked eye, but utilizing a vision system the productivity can be increased because the camera can compare a captured image with an reference image and decide autonomously whether it has defects or not. Inspected products are stacked on a pallet by a robotic arm that senses product status with a camera, and then an automatic guided vehicle (AGV) can carry it to storage or shipping autonomously. All processes are executed by vision technology. It is also being adopted in the field of surveillance and robot guidance.

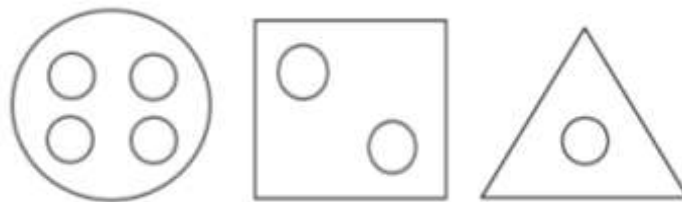
## **Application of Vision System for Education**

**Small Manufacturing Cell:** Several examples mentioned above were adapted to a small manufacturing cell, which is a scaled down version of real systems that are widely used in industry. This small cell is composed of a vision system, robotic arm, milling machine, c-more control panel, variable frequency drive (VFD), a programmable logic controller (PLC), and a barcode scanner. The conveyor belt, operated by VFD through the PLC program, carries products to different stations that communicate with other machines such as a camera, a milling machine, and a robotic arm the PLC can control the entire process. The camera and RoboRealm software for the vision system is used for the image acquisition, recognition, and analysis. For instance, when the product passes in front of the camera, switches on the conveyor belt would be on and vision system would capture, recognize shapes, and analyze it by matching it to a reference image as soon as the product has stopped. If it has defects or appears different than the reference image, then the vision system sends information to the PLC which can then send signals to the robotic arm and milling machine. The robotic arm can then pick up the product and put it back in the milling machine for rework or place in a reject pile (Figure 1). The barcode scanner reads the bar code on top of the product and sends information to the computer to provide part information to the vision system and allow for faster image analysis. The C-more panel connects to the PLC through an Ethernet cable and provides GUI which provides control of the PLC through a touch screen. The data center computer is in charge of data management, communication interfaces.

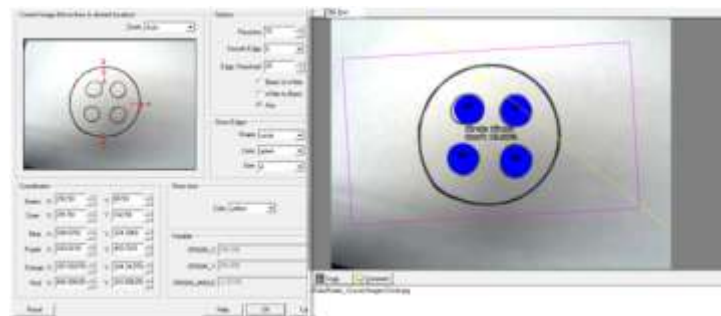


**Figure 1: CIM Cell with vision station incorporated**

There are three types of shapes representing different product (figure 2). There is a circle, a square, and a triangle. Each shape has some small circle inside representing part features. If there are an incorrect number of circles or the circles are an incorrect size, the product is regarded as defective (figure 3).



**Figure 2: Shapes used for testing camera/software**

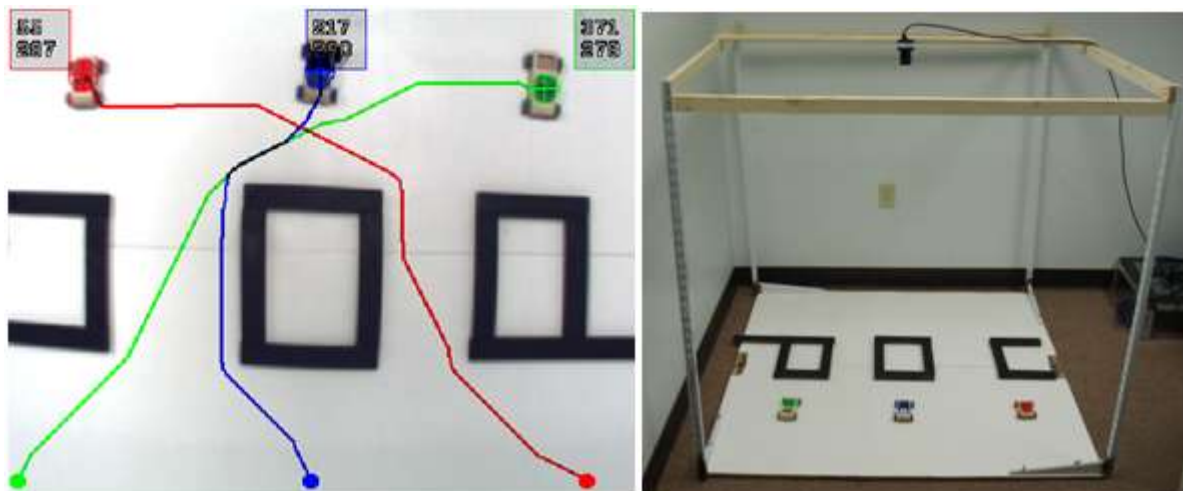


**Figure 3: Identification of known errors (# and location of holes)**

**Table 1 shows the function for shape recognition**

|   |  |   |
|---|--|---|
| Object Recognition<br>if OBJECT_NAME =<br>"Circle_circle" then<br>.. Origin_Probe<br>.. Canny<br>.. Circles<br>.. if CIRCLES_COUNT = 4<br>then<br>... Timer<br>... Write Images<br>.. end_if<br>end_if<br>: | :<br>if OBJECT_NAME =<br>"Square_circle" then<br>.. Origin_Probe<br>.. Canny<br>.. Circles<br>.. if CIRCLES_COUNT = 2<br>then<br>... Timer<br>... Write Images<br>.. end_if<br>end_if<br>: | :<br>if OBJECT_NAME =<br>"Triangle_circle" then<br>.. Origin_Probe<br>.. Canny<br>.. Circles<br>.. if CIRCLES_COUNT = 1<br>then<br>... Timer<br>... Write Images<br>.. end_if<br>end_if |
|---|--|---|

**Smart Robotic Warehouse:** A vision system was adapted to a simulated smart robot warehouse. This smart robot warehouse is composed of vision system with a camera installed on the ceiling to observe objects on the floor, in this case toy cars, and obstacles. The three toy cars are different colors; red, blue, and green. In this case the obstacles are black so that the vision system can recognize the difference between the toy cars and the obstacles. After that, it develops a path having each car move from point A to point B and produces X and Y coordinates for car's start and end positions (figure 4). Then it would transmit coordinate data to the moveable robot through the API in real time so that robot can get from place to place while avoiding obstacles. A manual control G.U.I. have been developed for the robots that will be used in the continuation of this research. This G.U.I. and a portion of the robot control code are shown in figures 5 and 6.

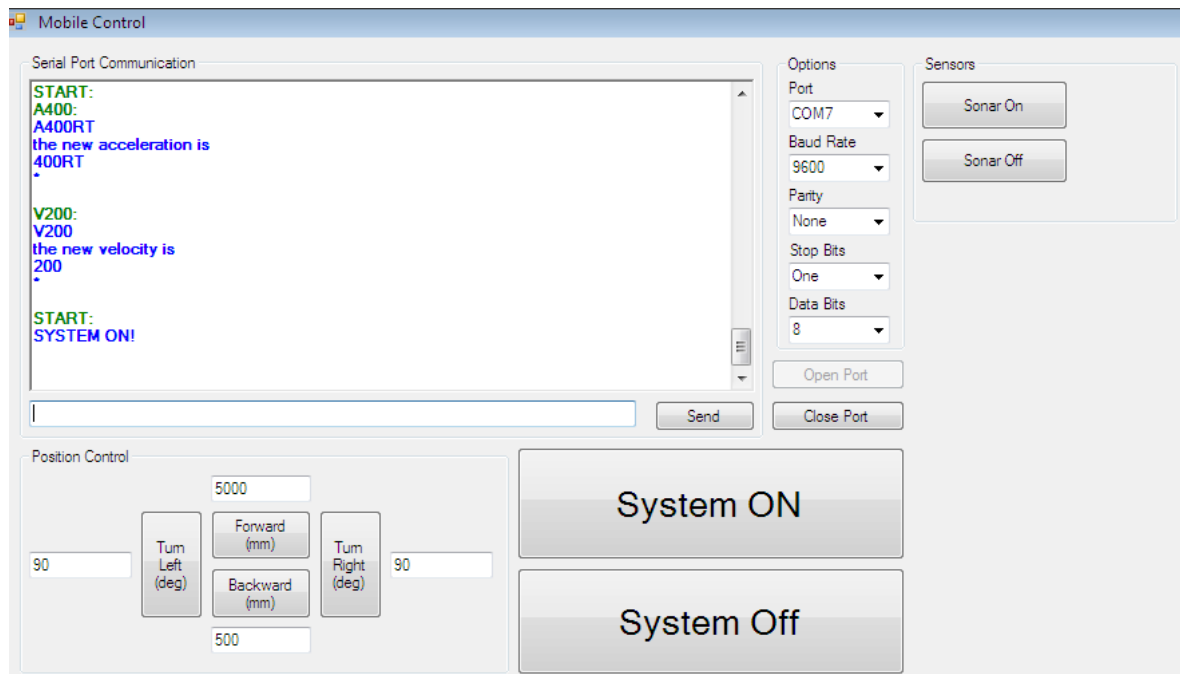


**Figure 4: Prototype warehouse set up for testing**



**Table 2 shows the function for path planning**

|   |   |  |
|---|---|--|
| Radial_Distortion<br>Crop 63,6 - 480,346<br>Marker[Corrected]<br>Color_Filter<br>Dilate 15<br>Center of Gravity<br>Marker[Revert]<br>Auto Threshold<br>Erode 12<br>Math Revert Current<br>Path_Planning<br>Display_Variables<br>: | Marker[Red]<br>Color_Filter<br>Dilate 15<br>Center of Gravity<br>Marker[Revert]<br>Auto Threshold<br>Erode 12<br>Math Revert Current<br>Path_Planning<br>Display_Variables<br>Marker[Blue]<br>Color_Filter<br>: | Dilate 15<br>Center of Gravity<br>Marker[Revert]<br>Auto Threshold<br>Erode 12<br>Math Revert Current<br>Path_Planning<br>Display_Variables<br>Math Current Red<br>Math Current Blue<br>Watch_Variables<br>: |
|---|---|--|



**Figure 5: Functions and programming environment for Roborealms**

```

sketch_MR_5_3 | Arduino 0022
File Edit Sketch Tools Help

sketch_MR_5_3.g

void Move()
{
  if (motor_go == 1)
  {
    // Decide which part of the velocity curve your at
    if (count < sa) // Acceleration
    {
      dly = 1 / (2 * a * t);
    }
    else if (count >= sa && count < (sa + sc)) // Constant velocity
    {
      dly = 1 / (2 * Va);
    }
    else if (count >= (sa + sc) && count < (sa + sc + sd)) // Deceleration
    {
      dly = 1 / (2 * d * ((Pt / Va) + (Va / d) - t));
    }

    t = t + 2 * dly; // update the current time
    if (dly < 0) // Error correction for time calculation
    {
      dly = 1 / (2 * a * 0.01);
    }

    // Move stepper one pulse using delay just calculated
    digitalWrite(stepPin , HIGH);
    digitalWrite(stepPin2 , HIGH);
    delayMicroseconds(dly * 1e6);
    digitalWrite(stepPin , LOW);
    digitalWrite(stepPin2 , LOW);
    delayMicroseconds(dly * 1e6);
    count ++;
    // The move is finished
    if (count >= Pt)
    {
      Serial.println ("Move Complete");
      Serial.print ("Total steps indexed: "); Serial.println (count);
      Serial.print ("Total distance traveled: "); Serial.println (count * 319.19 / 820);
      count=0;
      t=0.01;
      motor_go =0;
      Pt = 0;
    }
  }
}

```

**Figure 6: Sample program for the robot control**

## Low Cost Educational Kit

The following is a sample kit that could be used for education of engineering technology students. The kit will be kept as inexpensive as possible in order to minimize financial concerns when implementing the proposed program. Existing school computers should be sufficient for educational image processing because high speed and accuracy are not necessary.

## Software

RoboRealm should be used for image processing because it is easy to use and cost approximately \$50. This software can be purchased from the RoboRealm's website ([WWW.roborealm.com](http://WWW.roborealm.com)) and is available for a free 30 day trial (figure 7).



**Figure 7: RoboRealm software interface**

## Hardware

For a camera, it is recommended that a webcam is used. Webcams are available anywhere that computer accessories are sold and can usually be found for under \$20. The camera should come with any drivers that are required to operate it, as well as a USB cable or wireless antenna to connect it to the computer.

White paper and colored markers will also be needed. These materials will be used for simple shape and color recognition. It is recommended that they are purchased from the office supply store with best prices. A ream of printer paper costs about \$5 and enough markers for a whole class should cost about \$30.

Other useful object that could be purchased would be toys, tools, and other miscellaneous object that could be used to perform more complex analysis. It would also be possible to use object that are already available at the school such as pencils, book, or any other educational tools that are already in the class room.

## Course Program Outline

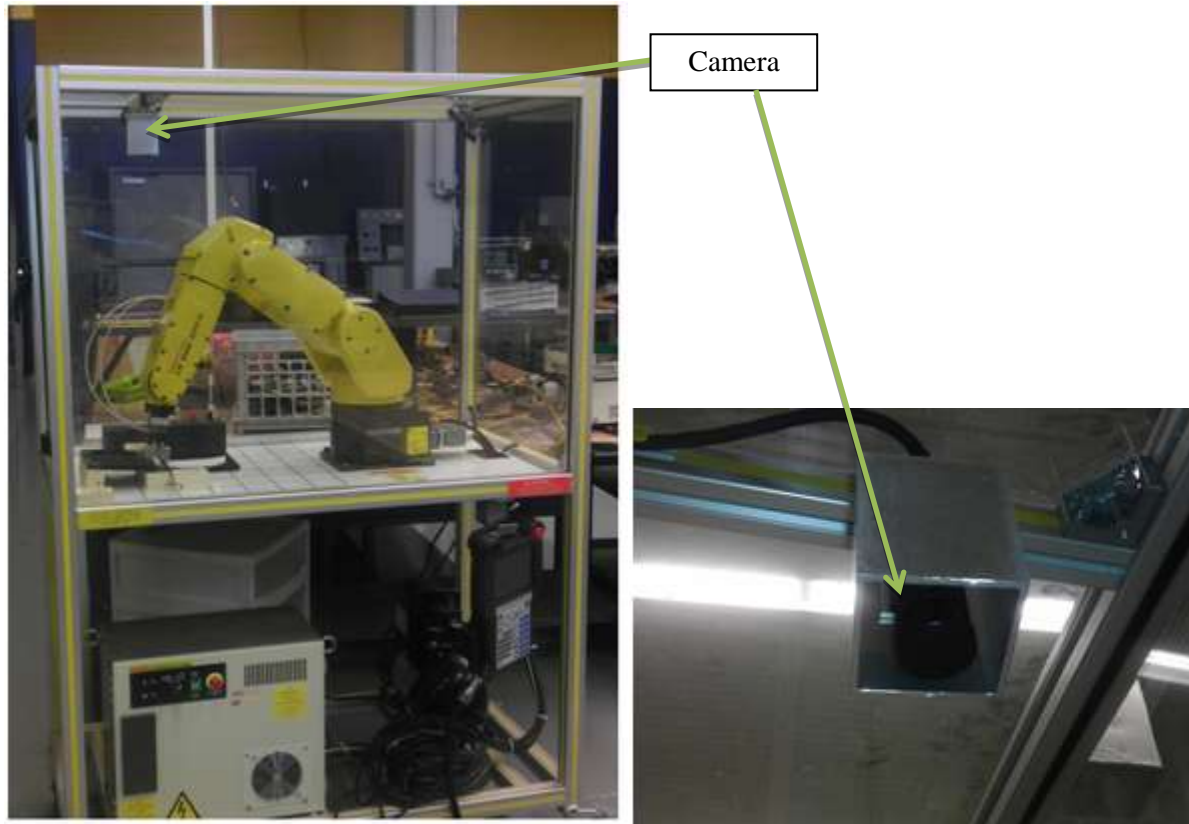
**Table 3 below shows the proposed class schedule for a course in robot vision systems.**

| Weeks | Subject                   | Content  | Note |
|-------|---------------------------|--|------|
| 1     | What is robot vision      | Discuss basic components of a robot vision system                          |      |
| 2     | What is a vision system   | Discuss how the components of a vision system work together                |      |
| 3     | Introduction to RoboRealm | Get familiarized with the RoboRealm user interface and available functions |      |
| 4     | Shape recognition         | Use RoboRealm to recognize basic shapes squares, circles, and triangles    |      |
| 5     | Compare shapes            | Use RoboRealm to compare shapes and images, and recognize a human face     |      |
| 6     | Recognize color           | Use RoboRealm to recognize color in  |      |

|    |                    |  |  |
|----|--------------------|--|--|
|    |                    | combination with shapes  |  |
| 7  | Path planning      | Use RoboRealm to navigate from point A to point B while avoiding obstacles |  |
| 8  | Motor outputs      | Use RoboRealm to send signals to motors for motion control                 |  |
| 9  | RoboRealm API      | Interface RoboRealm with other software using the API                      |  |
| 10 | Review and Project | Work on team projects to use robot vision to accomplish a goal             |  |

## Discussion & conclusion

The information given in this paper shows that a class that teaches the basics of robot vision would be useful, practical, and achievable. The primary obstacle of computer programming can be minimized by the proper selection of processing software, and possibly requiring a programming for engineers class as a pre-requisite. Equipment for the class can be very inexpensive because high speed and accuracy are not required for educational purposes. A course in robotics is already offered by the school, so the course in visions systems could be offered as a second class in a series. The attended school also has 2 Fanuc LR Mate 200 iC robotic arms, in educational enclosures, that are equipped with cameras and I/O capability for communication with other systems (figure 8). These could easily be integrated into the class.



**Figure 8: Current capabilities include cameras in the Fanuc CERT training cart.**

The increase in the use of automation and specifically robot vision systems in a variety of industries means that companies will be looking for engineers with the skills and knowledge required to design and maintain these systems. In order to accommodate that need, the attended school should offer the proposed class as an engineering technology elective. This will give graduates a valuable advantage in an increasingly competitive job market.

## Reference

- [1] Hagiwara, H., Asami, K., Komori, M.: FPGA Implementation of Image Processing for Real-Time Robot Vision System. *Communications in Computer and Information Science* 206, 134-141 (2011)
- [2] Okuno, H., Yagi, T.: A robot vision system for collision avoidance using a bio-inspired algorithm. *Lect. Notes Comput. Sci.* 4985, 107-116 (2008)
- [3] Oh, J., Jang, G., Oh, S., Lee, J., Yi, B., Moon, Y., Lee, J., Choi, Y.: Bridge Inspection Robot System with Machine Vision. *Automation in Construction* 18, 929-941 (2009)
- [4] Cesetti, A., Frontoni, E., Mancini, A., Zingaretti, P., Longhi, S.: A Vision-Based Guidance System for UAV Navigation and Safe Landing using Natural landmarks. *J Intell Robot Syst.* 57, 233-257 (2010)
- [5] [Wang, Binhai](#) (Electric Power Robotics Laboratory, Shandong Electric Power Research Institute, Jinan, 250002 Shandong, China); [Guo, Rui](#); [Li, Bingqiang](#); [Han, Lei](#); [Sun, Yong](#); [Wang, Mingrui](#) **Source:** *Journal of Field Robotics*, v 29, n 1, p 123-137, January-February 2012, *Applied Robotics for the Power Industry*
- [6] [Di Paola, Donato](#) (Institute of Intelligent Systems for Automation (ISSIA), National Research Council (CNR), Bari, Italy); [Milella, Annalisa](#); [Cicirelli, Grazia](#); [Distante, Arcangelo](#) **Source:** *International Journal of Advanced Robotic Systems*, v 7, n 1, p 19-26, March 2010

## Appendix 2: Sample C# Code Developed For Mobile Robot Control

Mobile Robot control version 5.7

started by: Noah Anderson

continued by: Matthew Floyd

Last Update: 5-13-13

description:

This program is written for an Arduino Mega 2560.

It receives input from the user in order to control a mobile robot.

The program specifies direction (forward and backward), velocity, turning, acceleration, and deceleration as well as turning the motor drivers on and off.

Notes:

V3.1 The motor pulsing method was changed for version 3. The old method uses time as the stopping criteria. The new method will use the number of steps as the stopping criteria.

Method change successful on P- command.

V3.2 The method developed in V3.1 was successfully implemented for P+, and the variables in the acceleration routine were changed to be relevant to the new method. The Jogging routine was completed, but the number of steps is limited to 1,000,000,000 for a given jog. The direction controls were also completed.

V4.0 Turning routines are being developed.

V4.1 A simple turning routine has been implemented. The direction and number of degrees of the turn can be specified. The robot wheels turn in opposite directions at the same speed to turn in place.

V4.2 The units for motion are changed from number of pulses to millimeters.

The type of count was also changed from int to long so the robot can move farther in one command.

V5.0 Sonar routines are being added.

V5.1 code to check the distance using sonar is added in the movement section. However, this causes a delay in between the motor steps.

Other alternatives will be explored. This code was removed.

V5.2 A second arduino board will be added to handle the monitoring of the sonar units. Serial communication will be used between

the two controllers. Not added till V5.3.

V5.2.1 Structure is being made more modular.

V5.3 A second arduino board will be added to handle the monitoring of the sonar units. Serial communication will be used between

the two controllers. Digital IO will be used to operate the second Arduino.

V5.3.1 More constants were added to make the program more easily adaptable to different robots.

V5.3.2 Constants were changed for the ProtoBot platform. Some of the pins were changed to make to account for the size of a new base.

V5.4 The method of serial communication is being changed to improve reliability.

V5.5 More changes were made to the serial communication to make it more reliable.

V5.6 Code is being added to operate the RFID scanner and LCD screen.

```
////Libraries////
```

```
#include <LiquidCrystal.h>
```

```
////Constants////
```

```
const float pi = 3.14159265; // the number Pi
```

```
const float wb = 174.625; // the distance from the center of the robot to the center of a turning wheel (mm)
```

```
const float wr = 50.8; // the radius of the drive wheels (mm)
```

```
const float ppr = 819; // the number of pulses per wheel revolution
```

```
////Variables////
```

```
float dly; // stepper pulse delay (microsec)
```

```
float t = 0.01; //time from start of move in (s) - You need to seed the initial time with something > 0 so you don't divide by Zero.
```

```
long count = 0; // count the number of pulses
```

```
int motor_go = 0;
```

```
String incoming_string_0 = ""; // a string to hold incoming data
```

```
String incoming_string_1 = ""; // a string to hold incoming data
```

```
String incoming_string_2 = ""; // a string to hold incoming data
```

```

char test_string = ' '; // for comparison with Serial2 incoming
boolean stringComplete = false; // whether the string is complete
boolean stringComplete_2 = false; // whether the string 2 is complete
float sa = 0; // the number of step while accelerating
float sc = 0; // the number of step durring constant velocity
float sd = 0; // the number of step while decelerating
float thr = 0; // the angle to be turned (rad)
float thd = 0; // the angle to be turned (degrees)
float V_mm = 0; // the velocity in mm/s
float A_mm = 0; // the acceleration in mm/s^2
float D_mm = 0; // the distance in mm
float Pt = 0; // total number of pulses for move (819 steps per rev)
float Vm = 0; // steady state velocity (pulse/s) (500 p/s = 194.63 mm/s With 50.8 wheel radius)
float a = 0; // acceleration (pulses/s^2) (1000 p/s^2 = 389.26 mm/s^2 With 50.8 wheel radius)
float d = 0; //Deceleration
////Settings////
float VmL = 500; // steady state linear velocity (pulse/s) (500 p/s = 194.63 mm/s With 50.8 wheel radius)
float VmT = 500; // steady state turning velocity (pulse/s) (500 p/s = 194.63 mm/s With 50.8 wheel radius)
float aL = 1000; // linear acceleration (pulses/s^2) (1000 p/s^2 = 389.26 mm/s^2 With 50.8 wheel radius)
float aT = 1000; // turning acceleration (pulses/s^2) (1000 p/s^2 = 389.26 mm/s^2 With 50.8 wheel radius)
////Arduino pins////
LiquidCrystal lcd(7, 6, 5, 4, 3, 2); //LCD control pins
//Right Side
#define dirPin 41
#define stepPin 15
//Left Side
#define dirPin2 40
#define stepPin2 14
//Main Relay
#define Start 34
//Sonar
#define Sonar 22
#define stoPin_1 29
#define stoPin_2 26

void setup()
{
  ////initialize serial communication////
  Serial.begin(9600);
  Serial1.begin(9600);
  Serial2.begin(9600);
  ////set up the LCD's number of columns and rows////
  lcd.begin(16, 2);
  ////set initial pin conditions////
  pinMode(dirPin, OUTPUT);
  pinMode(stepPin, OUTPUT);
  pinMode(dirPin2, OUTPUT);
  pinMode(stepPin2, OUTPUT);
  pinMode(Start, OUTPUT);
  pinMode(Sonar, OUTPUT);
  pinMode(stoPin_1, INPUT);
  pinMode(stoPin_2, INPUT);
  ////Variable setup////
  incoming_string_0.reserve(100);
  incoming_string_1.reserve(100);
  incoming_string_2.reserve(100);
  ////confirm setup complete////

```



```

Serial.println(); Serial.println();
Serial.println("Setup Done");
}
void loop()
{
//Serial communication
Serial_Comm_0(); //Command Comm
if(stringComplete) //Run commands if they are present
{
Commands(incoming_string_0);
incoming_string_0 = ""; //Clear string
}
Serial_Comm_1(); //sensor Comm
if(stringComplete) //Run commands if they are present
{
Commands(incoming_string_1);
incoming_string_1 = ""; //Clear string
}
Serial_Comm_2(); //sensor Comm
Move();
}
void Serial_Comm_0()
{
while (Serial.available())
{
// get the new byte:
char inChar = (char)Serial.read();
// : is the end of command
if (inChar == ':')
{
//Serial.println(incoming_string_0);

if (incoming_string == ("S"))
{
Serial.println(incoming_string);
motor_go = 0;
Serial.print ("Motion Stopped!");
Serial.print ("Total steps indexed: "); Serial.println (count);
count=0;
t=0.01;
Pt = 0;
}
////Acceleration and Velocity////
if (incoming_string.startsWith("AL"))
{
Serial.println(incoming_string);
A_mm = stringToLong(incoming_string.substring(2));
aL = A_mm * ppr / (2 * wr * pi);
Serial.println("the new linear acceleration is "); Serial.println(A_mm);
Serial.println("*");
}
if (incoming_string.startsWith("AT"))
{
Serial.println(incoming_string);
A_mm = stringToLong(incoming_string.substring(2));
aT = A_mm * ppr / (2 * wr * pi);
Serial.println("the new turning acceleration is "); Serial.println(A_mm);
}
}
}

```

```

Serial.println("**");
}
if (incoming_string.startsWith("VL"))
{
Serial.println(incoming_string);
V_mm = stringToLong(incoming_string.substring(2));
VmL = V_mm * ppr / (2 * wr * pi);
Serial.println("the new linear velocity is "); Serial.println(V_mm);
Serial.println("**");
}
if (incoming_string.startsWith("VT"))
{
Serial.println(incoming_string);
V_mm = stringToLong(incoming_string.substring(2));
VmT = V_mm * ppr / (2 * wr * pi);
Serial.println("the new Turning velocity is "); Serial.println(V_mm);
Serial.println("**");
}
////Jog////
if (incoming_string == "J+")
{
digitalWrite(dirPin2, HIGH);
digitalWrite(dirPin, LOW);
Vm = VmL;
a = aL;
d = a;
sa = (0.5 * Vm * Vm / a);
sc = 1000000000;
Pt = 1000000000;
motor_go=1;
Serial.println("Jog forward ");
Serial.println("**");
}
if (incoming_string == "J-")
{
digitalWrite(dirPin2, LOW);
digitalWrite(dirPin, HIGH);
Vm = VmL;
a = aL;
d = a;
sa = (0.5 * Vm * Vm / a);
sc = 1000000000;
Pt = 1000000000;
motor_go=1;
Serial.println("Jog backward ");
Serial.println("**");
}
////Turning////
if (incoming_string.startsWith("TL"))
{
Serial.println(incoming_string);
digitalWrite(dirPin, LOW);
digitalWrite(dirPin2, LOW);
thd = stringToLong(incoming_string.substring(2));
thr = thd * pi / 180;
Pt = (wb * thr * ppr)/(2 * wr * pi);

```

```

Vm = VmT;
a = aT;
d = a;
sa = (0.5 * Vm * Vm / a);
sc = (Pt - (Vm * Vm / a));
sd = sa;
motor_go=1;
Serial.println("the new destination is "); Serial.println((incoming_string.substring(2)));
Serial.println("");
}
if (incoming_string.startsWith("TR"))
{
Serial.println(incoming_string);
digitalWrite(dirPin, HIGH);
digitalWrite(dirPin2, HIGH);
thd = stringToLong(incoming_string.substring(2));
thr = thd * pi / 180;
Pt = (wb * thr * ppr)/(2 * wr * pi);
Vm = VmT;
a = aT;
d = a;
sa = (0.5 * Vm * Vm / a);
sc = (Pt - (Vm * Vm / a));
sd = sa;
motor_go=1;
Serial.println("the new destination is "); Serial.println((incoming_string.substring(2)));
Serial.println("");
}
////Arduino communication////
if (incoming_string.startsWith("Comm"))
{
Serial.println(incoming_string);

String CommString = incoming_string.substring(4) + ".";
Serial.println(CommString);
Serial1.println(CommString);
}
if (incoming_string.startsWith("Mes"))
{
Serial.println(incoming_string.substring(3));
Serial.println("");
}
////Start System////
if (incoming_string == ("START"))
{
digitalWrite(Start, HIGH);
Serial.println ("SYSTEM ON!");
}
////Stop System////
if (incoming_string == ("STOP"))
{
digitalWrite(Start, LOW);
Serial.println ("SYSTEM OFF!");
}
////Sonar////
if (incoming_string == ("SON"))
{

```

```

Serial.println(incoming_string);
digitalWrite(Sonar, HIGH);
Serial.println("Sonar is on ");
Serial.println("**");
}
if (incoming_string == ("SOff"))
{
Serial.println(incoming_string);
digitalWrite(Sonar, LOW);
Serial.println("Sonar is off ");
Serial.println("**");
}
incoming_string = ""; // Clear incoming_string
stringComplete = false; // changes stingComplete so that this void is not run until another command is given.
}
void Move()
{
if (motor_go == 1)
{
// Decide which part of the velocity curve your at
if (count < sa) // Acceleration
{
dly = 1 / (2 * a * t);
//Serial.print ("a "); Serial.print (t); Serial.print (": "); Serial.println (dly * 1e6);
}
else if (count >= sa && count < (sa + sc)) // Constant velocity
{
dly = 1/(2*Vm);

// Move stepper one pulse using delay just calculated
digitalWrite(stepPin , HIGH);
digitalWrite(stepPin2 , HIGH);
delayMicroseconds(dly * 1e6);
digitalWrite(stepPin , LOW);
digitalWrite(stepPin2 , LOW);
delayMicroseconds(dly * 1e6);
count ++;
//Serial.println (dly * 1e6);
//Serial.println (count);
// The move is finished

```

### Appendix 3: Sample EMGU CV Code Developed for Eye In The Sky Camera Image Processing

#### -Open CV:

OpenCV (Free Open Source Computer Vision) is a library of programming functions mainly aimed at real time computer vision. It has a BSD license (free for commercial or research use). OpenCV was originally written in C but now has a full C++ interface and all new development is in C++. There is also a full Python interface to the library. Example applications of the OpenCV library are Human-Computer Interaction (HCI); Object Identification, Segmentation and Recognition; Face Recognition; Gesture Recognition; Motion Tracking, Ego Motion, Motion Understanding; Structure From Motion (SFM); Stereo and Multi-Camera Calibration and Depth Computation; Mobile Robotics.

#### - Emgu CV:

[Emgu CV](#) is a cross platform .Net wrapper to the [OpenCV](#) image processing library. Allowing [OpenCV](#) functions to be called from .NET compatible languages such as C#, VB, VC++, IronPython etc. The wrapper can be [compiled in Mono](#) and run on Windows, Linux, Mac OS X, iPhone, iPad and Android devices. [Emgu CV](#) is written entirely in C#. The benefit is that it can be [compiled in Mono](#) and therefore is able to run on any platform Mono supports, including Linux, Mac OS X, iOS and Android. A lot of efforts has been spend to have a pure C# implementation since the headers have to be ported, compared with managed C++ implementation where header files can simply be included. But it is well worth it if you see [Emgu CV running on Fedora 10!](#) Plus it always gives you the comfort knowing that your code is cross-platform. [Emgu CV](#) can be used from several different languages, including C#, VB.NET, C++ and IronPython. On this wiki, we provide [examples](#) for all those languages, which are available from the [Examples section on Tutorial page](#). Our [Discussion Forum](#) is also available if you have any questions related to your favorite programming language.

```
namespace Eye_n_the_Sky.Image_Processor
{
    static class ImageProcessor
    {
        private static bool _robotAssigned = false;
        /* Input: Takes in an image from the camera and a reference to the current robot location
        * Output: It will modify the contents of the robot location variable to the correct
        * new coordinates, also saves all the currently detected obstacles in the obstacle list */
        static public Image<Bgr, byte> DrawBoxs(Image<Bgr, byte> input, ref MCvBox2D robot_loc, ref List<CircleF> obstacles)
        {
            const double cannyThreshold = 180.0;
            const double cannyThresholdLinking = 100.0;
            //image<Gray, Byte> cannyEdges = input.InRange(new Bgr(230, 230, 230), new Bgr(255, 255, 255));
            Image<Gray, Byte> cannyEdges = input.Canny(cannyThreshold, cannyThresholdLinking);
            //cannyEdges = cannyEdges.Canny(cannyThreshold, cannyThresholdLinking);
            //return cannyEdges.Convert<Bgr, byte>();
            Image<Gray, Byte> gray = input.Convert<Gray, Byte>().PyrDown().PyrUp();
            CircleF[] circles = gray.HoughCircles(
                new Gray(180),
                new Gray(100),
                2.0, //Resolution of the accumulator used to detect centers of the circles
                80.0, //min distance
                20, //min radius
                50 //max radius
            )[0]; //Get the circles from the first channel
            List<MCvBox2D> boxList = new List<MCvBox2D>();
            using (MemStorage storage = new MemStorage()) //allocate storage for contour approximation
            for (
                Contour<Point> contours = cannyEdges.FindContours(
                    CHAIN_APPROX_METHOD.CV_CHAIN_APPROX_SIMPLE,
                    RETR_TYPE.CV_RETR_LIST,
                    storage);
                contours != null;
                contours = contours.HNext)
            {
                Contour<Point> currentContour = contours.ApproxPoly(contours.Perimeter * 0.05, storage);
            }
        }
    }
}
```

```

    if (currentContour.Area > 1300 && currentContour.Area < 1400)
    {
        if (currentContour.Total == 4) //The contour has 4 vertices.
        {
            #region determine if all the angles in the contour are within [80, 100] degree
            bool isRectangle = true;
            Point[] pts = currentContour.ToArray();
            LineSegment2D[] edges = PointCollection.PolyLine(pts, true);
            for (int i = 0; i < edges.Length; i++)
            {
                double angle = Math.Abs(
                    edges[(i + 1) % edges.Length].GetExteriorAngleDegree(edges[i]));
                if (angle < 80 || angle > 100)
                {
                    isRectangle = false;
                    break;
                }
            }
            #endregion
            if (isRectangle) boxList.Add(currentContour.GetMinAreaRect());
        }
    }
}

/* Look at each box we detected with some checks to determine if it's near the last
 * known location of the robot */
foreach (MCvBox2D box in boxList)
{
    if (_robotAssigned)
    {
        if ((box.center.X < robot_loc.center.X + 100) && (box.center.X > robot_loc.center.X - 100))
        {
            if ((box.center.Y < robot_loc.center.Y + 100) && (box.center.Y > robot_loc.center.Y - 100))
            {
                input.Draw(box, new Bgr(0, 0, 255), 3);
                robot_loc = box;
            }
        }
    }
    else
    {
        input.Draw(box, new Bgr(0, 0, 255), 3);
        robot_loc = box;
        _robotAssigned = true;
    }
}
obstacles.Clear();
/* Add all the circles to the obstacle list */
foreach (CircleF circle in circles)
{
    input.Draw(circle, new Bgr(Color.LimeGreen), 3);
    obstacles.Add(circle);
}
return input;
}

```

#### Appendix 4: Sample C++ Code Developed for Kinect® Camera Image Processing

```
using System;
using System.Collections.Generic;
using System.ComponentModel;
using System.Data;
using System.Drawing;
using System.Linq;
using System.Text;
using System.Windows.Forms;
using LTT_UIFunctions;
using LTT_UIFunctions.DatabaseInteraction;

namespace FinalUI
{
    public partial class RemoteSupervisor : Form
    {
        #region Data Members
        private LTT_UIBackend _Backend;
        private UserInfo user_to_manipulate;
        #endregion
        #region Constructor
        public RemoteSupervisor()
        {
            InitializeAuthentication();
            _Backend = new LTT_UIBackend();
        }
        #endregion
        #region Path CRUD Functions
        private void btn_New_OnClick(object sender, EventArgs e)
        {
            tc_Paths.TabPages.Add(new PathTabPage(609, 457, 25, 25));
            tc_Paths.SelectedIndex = tc_Paths.TabCount - 1;

            btn_AddNodes.Enabled = true;
            btn_DeleteNodes.Enabled = true;
            btn_EditNodes.Enabled = true;
            btn_Pause.Enabled = true;
            btn_Start.Enabled = true;
            btn_Stop.Enabled = true;

            btn_AddNodes.Invalidate();
            btn_DeleteNodes.Invalidate();
            btn_EditNodes.Invalidate();
            btn_Pause.Invalidate();
            btn_Start.Invalidate();
            btn_Stop.Invalidate();

            tc_Screens.SelectedIndex = 1;
        }
        private void tc_Paths_SelectedIndexChanged(object sender, EventArgs e)
        {
            if (tc_Paths.TabCount != 0)
                lbl_CurrentPath.Text = "Current Path: " + tc_Paths.SelectedTab.Text;
            else

```



```

        lbl_CurrentPath.Text = "Current Path: None";
        lbl_CurrentPath.Invalidate();
    }
    private void btn_Close_OnClick(object sender, EventArgs e)
    {
        if (tc_Paths.TabCount != 0)
            tc_Paths.TabPages.Remove(tc_Paths.SelectedTab);

        if (tc_Paths.TabCount == 0)
        {
            btn_AddNodes.Enabled = false;
            btn_DeleteNodes.Enabled = false;
            btn_EditNodes.Enabled = false;
            btn_Pause.Enabled = false;
            btn_Start.Enabled = false;
            btn_Stop.Enabled = false;

            btn_AddNodes.Invalidate();
            btn_DeleteNodes.Invalidate();
            btn_EditNodes.Invalidate();
            btn_Pause.Invalidate();
            btn_Start.Invalidate();
            btn_Stop.Invalidate();

            btn_AddNodes.Update();
            btn_DeleteNodes.Update();
            btn_EditNodes.Update();
            btn_Pause.Update();
            btn_Start.Update();
            btn_Stop.Update();
        }
    }
    private void btn_Open_OnClick(object sender, EventArgs e)
    {
        PathInfo path_to_open = new PathInfo(((DataGridview)(this.Controls.Find("dgv_PathList", true)[0])).SelectedCells);

        //_Backend.GetPoints(path_to_open);

        tc_Paths.TabPages.Add(new PathTabPage(tc_Paths.Width, tc_Paths.Height, 25, 25));
        tc_Paths.SelectedIndex = tc_Paths.TabCount - 1;

        btn_AddNodes.Enabled = true;
        btn_DeleteNodes.Enabled = true;
        btn_EditNodes.Enabled = true;
        btn_Pause.Enabled = true;
        btn_Start.Enabled = true;
        btn_Stop.Enabled = true;

        btn_AddNodes.Invalidate();
        btn_DeleteNodes.Invalidate();
        btn_EditNodes.Invalidate();
        btn_Pause.Invalidate();
        btn_Start.Invalidate();
        btn_Stop.Invalidate();

        tc_Screens.SelectedIndex = 1;
    }
}

```

```

#endregion
#region Path Manipulation
private void btn_EditNodes_onClick(object sender, EventArgs e)
{
    ((PathTabPage)tc_Paths.SelectedTab).Editable(true);
    ((PathTabPage)tc_Paths.SelectedTab).Addable(false);
    ((PathTabPage)tc_Paths.SelectedTab).Deletable(false);

    btn_EditNodes.Enabled = false;
    btn_DeleteNodes.Enabled = true;
    btn_AddNodes.Enabled = true;

    btn_AddNodes.Invalidate();
    btn_DeleteNodes.Invalidate();
    btn_EditNodes.Invalidate();

    btn_AddNodes.Update();
    btn_DeleteNodes.Update();
    btn_EditNodes.Update();
}
private void btn_AddNodes_onClick(object sender, EventArgs e)
{
    ((PathTabPage)tc_Paths.SelectedTab).Editable(false);
    ((PathTabPage)tc_Paths.SelectedTab).Addable(true);
    ((PathTabPage)tc_Paths.SelectedTab).Deletable(false);

    btn_EditNodes.Enabled = true;
    btn_DeleteNodes.Enabled = true;
    btn_AddNodes.Enabled = false;

    btn_AddNodes.Invalidate();
    btn_DeleteNodes.Invalidate();
    btn_EditNodes.Invalidate();

    btn_AddNodes.Update();
    btn_DeleteNodes.Update();
    btn_EditNodes.Update();
}
private void btn_DeleteNodes_onClick(object sender, EventArgs e)
{
    ((PathTabPage)tc_Paths.SelectedTab).Editable(false);
    ((PathTabPage)tc_Paths.SelectedTab).Addable(false);
    ((PathTabPage)tc_Paths.SelectedTab).Deletable(true);

    btn_EditNodes.Enabled = true;
    btn_DeleteNodes.Enabled = false;
    btn_AddNodes.Enabled = true;

    btn_AddNodes.Invalidate();
    btn_DeleteNodes.Invalidate();
    btn_EditNodes.Invalidate();

    btn_AddNodes.Update();
    btn_DeleteNodes.Update();
    btn_EditNodes.Update();
}

```

```

}
#endregion
#region Path Execution
private void btn_Stop_onClick(object sender, EventArgs e)
{
    _Backend.StopRobot();
    _Backend.RobotInterface.Disconnect();
}
private void btn_Submit_Click(object sender, EventArgs e)
{
    try
    {
        List<AbstractInfo> user_list = _Backend.GetUsers();
        int valid_combo = _Backend.CheckUser(tb_Username.Text, tb_Password.Text, user_list);

        if (valid_combo == 1 || valid_combo == 2)
        {
            InitializeMainScreen();
            if (valid_combo != 1)
                tc_Screens.Controls.RemoveAt(2);
            else
            {
                LoadUsers(user_list);
            }
            List<AbstractInfo> paths = _Backend.GetPaths();
            foreach (PathInfo path in paths)
            {
                if (path.UserID == _Backend.CurrentUser.ID || path.Global || _Backend.CurrentUser.Admin)
                {
                    string owner = "";
                    foreach (UserInfo user in _Backend.GetUsers())
                    {
                        if (path.UserID == user.ID)
                            owner = user.Username;
                    }
                    dgv_PathList.Rows.Add(path.PathID, path.PathName, owner, path.Created, path.Modified);
                }
            }
        }
        else
        {
            lbl_WrongPassword.Visible = true;
            lbl_WrongUsername.Visible = true;
        }
    }
    catch
    {
    }
}
private void btn_Start_Click(object sender, EventArgs e)
{
    PathTabPage pathpage = (PathTabPage)this.tc_Paths.SelectedTab;
    _Backend.ExecutePath(pathpage.Path, new MovementFinishedHandler(ShowFinishedMovement));
}

```

```

        kinect = new KinectDepthViewer.MainWindow(new
KinectDepthViewer.MainWindow.ObjectDetectionHandler(ObjectDetected));
        kinect.Show();
    }
    public void ObjectDetected()
    {
        kinect.ObjectDetection = null;
        kinect.AllClear = AllClear;
        _Backend.StopRobot();
    }
    public void AllClear()
    {
        kinect.ObjectDetection = ObjectDetected;
        kinect.AllClear = null;
        _Backend.ContinuePath();
    }
    public void ShowFinishedMovement(Node n)
    {
        PathTabPage pathpage = (PathTabPage)this.tc_Paths.SelectedTab;
        pathpage.RedrawEclipse(n);
    }
}
#endregion
#region User CRUD Functions
private void btn_EditUser_Click(object sender, EventArgs e)
{
    user_to_manipulate = new UserInfo(((DataGridView)(this.Controls.Find("dgv_UserList", true)[0])).SelectedCells);

    InitializeEditUser(user_to_manipulate);
}
private void btn_AddUser_Click(object sender, EventArgs e)
{
    InitializeAddUser();
}
private void btn_SubmitAdd_Click(object sender, EventArgs e)
{
    string firstname = ((TextBox)this.tab_Administration.Controls.Find("tb_FirstName", true)[0]).Text;
    string lastname = ((TextBox)this.tab_Administration.Controls.Find("tb_LastName", true)[0]).Text;
    string username = ((TextBox)this.tab_Administration.Controls.Find("tb_FirstName", true)[0]).Text +
((TextBox)this.tab_Administration.Controls.Find("tb_LastName", true)[0]).Text;
    string password = ((TextBox)this.tab_Administration.Controls.Find("tb_Password", true)[0]).Text;
    string email = ((TextBox)this.tab_Administration.Controls.Find("tb_Email", true)[0]).Text;
    bool admin = ((CheckBox)this.tab_Administration.Controls.Find("cb_Admin", true)[0]).Checked;
    UserInfo newuser = new UserInfo(firstname, lastname, username, password, email, 0, admin);

    _Backend.AddUser(newuser);
    InitializeAdministrationTab();
    LoadUsers(_Backend.GetUsers());
}
private void btn_CancelEdits_Click(object sender, EventArgs e)
{
    InitializeAdministrationTab();
    LoadUsers(_Backend.GetUsers());
}
private void btn_SubmitEdits_Click(object sender, EventArgs e)
{
    string firstname = ((TextBox)this.tab_Administration.Controls.Find("tb_FirstName", true)[0]).Text;

```

```

        string lastname = ((TextBox)this.tab_Administration.Controls.Find("tb_LastName", true)[0]).Text;
        string username = ((TextBox)this.tab_Administration.Controls.Find("tb_FirstName", true)[0]).Text +
        ((TextBox)this.tab_Administration.Controls.Find("tb_LastName", true)[0]).Text;
        string password = ((TextBox)this.tab_Administration.Controls.Find("tb_Password", true)[0]).Text;
        string email = ((TextBox)this.tab_Administration.Controls.Find("tb_Email", true)[0]).Text;
        bool admin = ((CheckBox)this.tab_Administration.Controls.Find("cb_Admin", true)[0]).Checked;
        UserInfo newuser = new UserInfo(firstname, lastname, username, password, email, user_to_manipulate.ID, admin);

        _Backend.EditUser(user_to_manipulate, newuser);
        InitializeAdministrationTab();
        LoadUsers(_Backend.GetUsers());
    }
    private void btn_DeleteUser_Click(object sender, EventArgs e)
    {
        user_to_manipulate = new UserInfo(((DataGridView)(this.Controls.Find("dgv_UserList", true)[0])).SelectedCells);
        DialogResult messagebox_result = MessageBox.Show("Would you really like to delete the selected user?", "Delete
Confirmation", MessageBoxButtons.YesNo);
        if (DialogResult.Yes == messagebox_result)
            _Backend.DeleteUser(user_to_manipulate.ID);

        LoadUsers(_Backend.GetUsers());
    }
    private void LoadUsers(List<AbstractInfo> user_list)
    {
        ((DataGridView)tab_Administration.Controls.Find("dgv_UserList", true)[0]).Rows.Clear();
        foreach (UserInfo user in user_list)
        {
            string admin = "";
            if (user.Admin)
                admin = "Yes";
            ((DataGridView)tab_Administration.Controls.Find("dgv_UserList", true)[0]).Rows.Add(user.ID, user.Name,
user.Username, user.Password, user.Email, admin);
        }
    }
    #endregion
    KinectDepthViewer.MainWindow kinect;
}
}

```

## Appendix 5: Summary of Expenditures by Category

**OREGON INSTITUTE OF TECHNOLOGY**  
3201 CAMPUS DRIVE, KLAMATH FALLS, OR 97601  
BUSINESS AFFAIRS OFFICE (541) 885-1226  
FEDERAL TAX ID #48-1278527

To:  
Organization for Economic Initiatives  
Attn: Ellen Fuller  
PO Box 866  
Corvallis, OR 97339

Date: October 19, 2012  
  
Invoice Number: 8392  
  
Period : September 30, 2012

Reference: 2010-2012 Northwest Mfg Initiative  
Contract No.: W911NF-11-1-0023  
12/6/10-12/5/12

|                              | This Period | Total Expenses | Budget       | Available    |
|------------------------------|-------------|----------------|--------------|--------------|
| Labor                        | \$0.00      | \$43,784.00    | \$43,784.00  | \$0.00       |
| Student Pay                  | \$0.00      | \$14,178.50    | \$14,544.00  | \$365.50     |
| Other Payroll Expenses (OPE) | \$0.00      | \$12,850.55    | \$13,220.00  | \$369.45     |
| Supplies                     | \$778.46    | \$2,257.53     | \$30.00      | (\$2,227.53) |
| Travel                       | \$0.00      | \$513.40       | \$200.00     | (\$313.40)   |
| Equipment                    | \$0.00      | \$40,678.98    | \$59,100.00  | \$18,421.02  |
| Indirect Charges             | \$0.00      | \$33,908.06    | \$34,122.00  | \$213.94     |
| Total                        | \$778.46    | \$148,171.02   | \$165,000.00 | \$16,828.98  |

### Final Purchases in December, 2012

- 6 new computers for Laser Cutter, Filament Winder, Foam Router, Robot Control Station
- 1 laptop to mount on battle-bot chassis with Kinect 3D cameras
- 3 Megapixel, HD IP camera to mount on manufacturing facility ceiling as Eye In The Sky
- Arduino control, gecco drives, wireless control, electronics to complete 4 mobile robots
- Safety guards, spools of composite filament, electrical box, wiring for custom CNC filament winder
- Materials for product development and prototyping on laser, router, plasma cutter, RP machine
- Cutting tools including milling bits, router bits and drill bits for foam, wood and metal applications

## Appendix 6: Engineering Dean's Newsletter from Spring 2012

### Oregon Tech's Engineering Students Benefit from ARMY Grant that Funds Inter-Disciplinary Robotics Research and Equipment for Composites Manufacturing

As part of a larger 5 year Army Research Lab (ARL) project called the Northwest Manufacturing Initiative, the MMET department at Klamath Falls has greatly increased its' laboratory capabilities and become a regional center for both *Robotics* and *Composite Materials* education (2 very popular and growing areas of focus in industry). In addition to providing new and automated tools that can be used in the future for teaching and hands-on projects, the grant has brought together students and faculty from different departments to investigate problems that are multi-disciplinary by nature. As the project winds down to an end this coming December, it gives us a chance to reflect on the lessons learned and the exciting possibilities in the future.

Up to now, the research and development related to autonomous robot control has been iterative based on experiences and focused on understanding the technology (hardware and software) related to the physical movement of the robot and camera based vision systems used for object recognition and location monitoring. As the pieces of the puzzle come together, students in Prof. Jim Long's junior Software Engineering Technology program will be taking a battle-bot chassis and controls built by students from MMET and adding a 3D image/shape recognition capability using the KINECT systems utilized on the popular X-Box video games. The idea is that the new robot, which will have an onboard CPU, sensors and controls will assist the robot in avoiding obstacles such as fork-lifts, pallets and even humans as it operates in a manufacturing or materials warehouse application. It has been a fun experience so far because each group of students is very interested in what the other group is doing.



Another area that has been positively impacted by the ARMY grant is in new product development, especially with products manufactured using composite materials. This summer, a 4' x 8' computer controlled router was purchased and will be used to efficiently machine molds for composite parts. In addition, a filament winding machine for cylindrical composite parts and a 150W CO2 laser cutter/engraver were installed and are currently in use. As students do projects such as building rockets, UAV's, race cars, bicycles, etc. these additional processes / machines will provide the them with valuable experience and a capability that is similar to what is available in industries such as aerospace, R & D, automotive and manufacturing. As a result of the grant, there has been a positive effect on enrollment of new students after visiting our labs during Tech Trek or Campus Preview Day events and an increased sense of pride and motivation for current students.



Written By: David Culler, Assoc. Prof, MMET  
P.I., ARL010



## **Appendix B – Portland State University Final Report**

## Introduction

Additive surface engineering utilizes materials science and engineering principles and materials processes to create surface regions with tailored engineered properties for new components and for in service dimensional restoration. This research program was directed toward two coatings technologies, physical vapor deposition and secondarily cold metal transfer using gas metal arc welding. Two other deposition technologies, electrospark deposition and electroslag surfacing were the focus of previous detailed studies and production implementation. Collectively these families of surface engineering technologies result in single pass thicknesses ranging from a few microns to approximately 5000 microns. For the PVD technology attention was focused on the structure and properties of the deposited coatings resulting from deposition parameters that limit substrate temperature to 250°C, rather than the typical 350-400°C substrate temperatures.

The physical vapor deposition process, PVD, used a magnetron sputter deposition system, a non substrate melting process that does not develop a heat affected zone. However for this process the entire substrate is normally heated to 400°C or above. Deposition onto fully heat treated ultrahigh strength quench and tempered steels with yield strengths of 1620 MPa, (235ksi) and above effectively further tempers the alloy and reduces the hardness, possibly resulting in a temper embrittled microstructure in addition to not providing the substrate interface hardness capable of supporting very hard coatings. Hence these AISI 4340 type alloys are not coated using PVD techniques if ultrahigh substrate strengths are required. This project studied the effect of low temperature deposition, nominally 250°C, on the structure and properties of high hardness physical magnetron vapor deposited coatings based on Cr, Ti and Zr. Coating thicknesses around 7 microns were deposited, (about 1 hr deposition time) onto HRC 53 steel, 0.5wt% carbon. Characterization of the PVD coatings consisted of microstructural (OPT, SEM, TEM), chemical, erosion, scratch, and mechanical strain to failure.

Electrospark deposition results in a single layer of similar thickness, 4-6 microns, have been previously reported. ESD coatings generally result in a heat affected zone thickness of less than 20 microns, as measured by hardness change, depending on deposition conditions. The second layer only affects about a 6 micron depth of the original substrate, less than a grain diameter, and after the third pass there is no more influence on the substrate.

The second deposition technology considered in this project is a relatively new, emerging process technology designated cold metal transfer, CMT and developed by Fronius. This pulsed gas metal arc welding process, P-GMAW, retracts the wire on each pulse to restrict the arc duration for each pulse. A fully digital computer controlled power supply allows spatter free reduced heat input welding. It is a low heat input arc welding process designed to join very thin gage materials. Hence this study evaluated its low heat input characteristics for application

to thin single layer coatings onto fully hardened steel. In order to study bead profiles and heat affected zone features, the CMT process was used on quenched and flash tempered medium carbon steel, AISI 4142.

The research technical challenges vary with deposition technologies and the substrate properties. Evaluation of the PVD process targeted the properties of several hard coatings compositions deposited under varied parameters, the resulting properties associated with each coating with a common denominator of limiting the substrate temperature to permit deposition onto fully heat treated ultrahigh strength steel. In addition to varying the primary coating deposition element, Cr, Ti, and Zr, the nitrogen gas flow was varied by a factor of two to change the ratio of each element to that of nitrogen. Both conventional PVD as well as Plasma Assisted PVD deposition methods were evaluated. Both employed magnetron sputter targets. The evaluation focused on coating hardness and mechanical durability, through strain to failure, erosion and scratch resistance methods.

Cold Metal Transfer evaluation focused on CMT heat input and the resulting single layer bead height as relating to minimum deposit thickness, and heat affected zone depth and hardness for CMT deposited onto fully hardened 4142 steel. Additionally, the influence of substrate thickness on both single layer deposits and on heat affected zone response.

## **Experimental Procedures**

### **Physical Vapor Deposition**

A series of coatings were deposited on to hardened steel substrates by Dr Ronghua Wei at Southwest Research Institute. SwRI has extensive PVD coating experience with well controlled systems and experienced operators. Additionally they have a modified PVD system that has a plasma assisted PVD capability. Schematics of both SwRI systems are shown in figure 1. Target thickness was 7 microns. Samples provided to SwRI were mechanically polished to a 1 micron surface finish and heat treated to a HRC 52 hardness by isothermally treating the samples at about 270°C, just above the Ms temperature. SwRI maintained the substrate temperature at 250°C for all deposition parameters. Standard precleaning practices were employed and a range of deposition conditions evaluated. Significantly two levels of nitrogen gas flow were use, one 50% of the other to result in an approximately 2x nitrogen level in the coating. This translated into a deposition of TiN and Ti<sub>2</sub>N for example. In all over 40 sample conditions were produced, some for baseline process optimization and others for generating a range of coatings and hardnesses. Chromium, Titanium, Zirconium targets were used. Results are referenced relative to conventional electrolytic hard Cr coatings, an industry standard. Recognized health dangers associated with hexavalent chromium is making hard chromium electroplated coating an increasingly restricted process and the global research community is

seeking alternative technologies. In addition to TiN and ZrN deposits, SwRI deposited Ti and Zr with silicon and carbon to form TiSiCN and ZrSiCN coatings. Measured victor hardness levels ranged from 800 to over 4000 for the coatings and coating deposition conditions evaluated. A summary of key coatings evaluated is shown in table 1. Also include in this table are the resulting micro and nano hardnesses, nano measured modulus, deposit chemistry, and mechanical property data.

### **Cold Metal Transfer GMAW**

Over the past 2 decades PSU has studied, characterized and optimized surface coating technologies ranging from the current PVD/PEMS 7 micron thick coating, electrospark deposition coatings as thin as 5 microns per layer, and 5000micron thick electrosag surfacing deposits. Heat affected zone thicknesses ranged from 12 microns up to 12,500 microns. Cold metal transfer is a new process that fits near the lower end of this spectrum, about 1200 micron thick single layer deposits. A Fronius Cold Metal Transfer (CMT) patented system was used by PSU. This system uses inverter type power supply, is fully digital with a computer programmed logic that established the pulse characteristics. Integral to CMT is a servo motor in the torch that retracts the wire on every pulse, pinching the arc and eliminating current flow for a significant portion of each pulse. This reduces heat input and spatter and allows smooth starting and stopping. The system is preprogrammed by Fronius, limiting the ability to conduct defined R/D trials. Inputting the material type and thickness, gas, and wire information generates the operating conditions. A change in stick out or voltage automatically results in real time computer controlled adjustments to the process conditions. An excellent system for automated production welding, but not as great for R/D conditions where the intent is to define limiting conditions.

PSU configured the CMT torch on a side beam system with automatic travel speed. A fixture was designed to hold coupons for weld trials. In order to measure temperatures during welding, a series of thermocouples were welded to the bottom of the plate to be welded. The TCs were arranged in parallel with a spacing to allow parallel non overlapping independent CMT passes to be made, one pass directly over each of 4 thermocouples. The CMT configuration and plate fixture is shown in figure 2. These thermocouples were connected to a data acquisition system providing real time visual display of all thermocouples and recoding each thermocouple every 0.5 seconds. Each successive pass was started after the coupon temperature was below 150°F (66°C). The weld coupon, a 15mm square plate, was fixed to a x-y positioner which could be precisely positioned for each pass to ensure that each pass traversed directly over a thermocouple. The Weld setup is shown in figure 2 and an example of the thermocouple record for each of 4 separate passes is shown in figure 3. The highest temperature is for the thermocouple directly under the first pass. All thermocouples however were activated for each

pass to record the entire thermal history at each pass location. Interpass times were such that the entire plate was less than 75°C before the next pass was initiated.

**CMT welding procedure:** The final CMT welding parameters, after optimization trials were as follows for the 4 plate thicknesses:

Gas shield: 98-2 Ar-Co<sup>2</sup>

Electrode wire: AWS ER307M. 1.1mm wire diameter

Voltage: 13.8 - 20.7 controlled by Fronius system and adjusted based on thickness, shielding gas and travel speed

Amperage: 118 - 171 controlled by Fronius system and adjusted based on thickness, shielding gas and travel speed

Wire feed speed: 406-660cm/minute controlled by Fronius system and adjusted based on thickness, shielding gas, and travel speed

Torch position: forehand

Travel Speed: 71-147 cm/minute; controlled independently from Fronius

**CMT materials:** 4142 plate material was used for all surfacing tests. The plates were solution heat treated at 850°C, then oil quenched and flash tempered at 200°C for 15 minutes. While not a typical material heat treatment condition. The 4142 steel is sensitive to tempering and the lightly tempered martensite is sensitive to tempering. This made measuring heat affected zone hardness profiles a sensitive method to determine the heat affected zone size based on microhardness. Additionally any HAZ region exhibiting very high hardness would represent a resolution treated and quenched HAZ while hardnesses less than the base material would represent tempered HAZ profiles. Initially tempering the 4142 steel would have reduced the sensitivity of the martensite to tempering and made HAZ determination more difficult.

Plate material was obtained in 4 thicknesses: 6.35mm, 3.17mm, 2mm, and 1.27mm in order to assess how the bead height would be influenced by the plate thickness.

## **Characterization Analysis**

### **Microstructural, Microhardness and Micro-chemical**

Standard optical metallography techniques were used for all coatings. In order to obtain uniformly prepared surfaces all polishing was done using an automated Struers Rotopol configured to hold 6 samples at one time. A Struers Scentis image analysis software program

was used to measure coating thickness. A Struers Duramin automated microhardness test system was used for all hardness profiles. Applied forces ranged from 25gm to 100 gm depending on the hardness being measured. Due to the thickness of the coating only one microhardness indentation could be made across the coating thickness.

A FEI FE-SEM was used for all SEM imaging. Both top and cross section analysis was performed. Due the thickness of the PVD coatings most analysis was done using the SEM on samples in the as polished condition. Transmission electron microscopy was done using an FEI 200kv Tecnai field emission TEM. Samples were prepared using a FEI Dual Beam focused ion beam.

### **Nano indentation characterization**

Nano characterization was done using both Hysitron and CSM nano test instruments and by SwRI. Cross sections of the PVD coatings for indentation analysis were prepared using the Struers Rotopol automated polishing system. Final polished used 0.04 micron silica.

### **Mechanical Strain to Failure**

Various techniques have been used in the literature to try to determine the mechanical strain to failure for coatings. Most use three or four point bend tests or possible axial tension tests. However all these tests suffer from cracking starting from an edge. Indentation tests, usually HRC type tests can cause coating cracking around the indent area but analysis is after the fact and not during loading. PSU developed a non coating contact bulge test technique to uniformly plastically strain the coating without any edge or contact effects. Coupling the test specimen to acoustic emission sensors and recording the acoustic emission as the load increased permitted characterization of the acoustic emission signature during loading, during the hold period, and during unloading when any cracking would produce emission from crack surfaces rubbing during closure.

The mechanical loading system used a 10mm carbide ball in a holding fixture like that in a Brinell hardness test system. The ball was fixtured and aligned in an Instron test system that could program a loading ramp rate, constant load hold period and a programmed unloading rate. Sensors monitored the entire cycle for acoustic emission with the intent of detection the onset of cracking, its amplitude and the overall quantity of acoustic emission. The carbide ball indented the opposite side of the sample from the coated side. The sample was positioned on a soft aluminum anvil with a small indent directly under the ball (the depression was made by pressing the carbide ball into the anvil to a depth equal to  $\frac{1}{2}$  of the ball diameter and then retracting the ball and inserting the test coupon and then conducting the indent load sequence from the back side. The depression in the anvil provided clearance for the coated side to deform due to the ball indentation on the back side and yet the budged coating did not contact

the anvil relief depression. At the same time the surrounding anvil area provided support for the coupon. The test setup positioned in the Instron is shown in figure 4. Two acoustic emission sensors are shown, one coupled to the coated coupon and the other coupled directly to the ball indenting fixture. An example of the strained coating is shown in figure 5 for electrolytic hard chrome. In addition to acoustic emission analysis, the deformed coatings were examined under both optical and scanning electron microscopy to characterize the extent of cracking. Up to 6 indents were made on each coating at up to 6 load levels, between 100-3000kg, and characterized after each load application in order to develop a rating basis for cracking resistance.

### **Erosion testing**

The test procedure was modeled after the procedure used in the ASTM G76-07 – The Standard Test Method for Conducting Erosion Tests by Solid Particle Impingement Using Gas Jets. Preliminary erosion tests were conducted to establish test parameters that could be applied to the entire range of samples to be tested. The gas used was compressed air with a back pressure of 55 psi and a 55 CFM flow rate. A particle feed rate of 2 grams/min was used. The particle feed rate was accurately controlled and monitored by using a particle feed metering system used in plasma spray systems, figure 6. Particle feed rates were verified by directing the nozzle into a container, collecting the alumina erodent in the container and weighing the amount collected after one minute. A rotating double disk apparatus was used to calculate a particle velocity of 90 m/s using these conditions. The erodent was 50 micron alumina powder.

Samples were cleaned in acetone filled beakers in an ultrasonic cleaner for 5 minutes and weighed before testing. A balance with an accuracy of  $10^{-5}$  g was used. Samples were tested for 4 minutes at 30° and between 30 seconds and 4 minutes at 90°. A custom fabricated specimen holder was used to orient the samples at 30°. The nozzle was 20 mm from the surface of the sample. The specimen holder can be seen in figure 7 with the nozzle positioned over the 30° orientation.

### **Scratch testing**

Scratch tests were done using a PSU scratch test system as well as scratch test systems at Hysitron and CSM. The system utilizes a programmable progressive load applied using pneumatic pressure onto a HRC diamond indenter while the test coupon is translated at a programmable rate. The traversing rate was 10mm/minute and the load increase rate was 100newton/minute. The load force was determined recording the air pressure used to apply the load to the diamond indenter and also by inserting a load cell in the load train above the indenter. An x-y positioner allowed parallel 10mm long scratches to be made at a distance of



three scratch widths from each scratch. Five parallel scratches were made on each test coupon. The scratch width as a function of load, load to initiate damage, and the nature of the damage was determined using optical metallography analysis.

## Results

**Coating microstructure and hardness** The PVD/PEMS coatings microstructures and hardnesses were studied in detail due to their ultrafine complex microstructures widely varying hardnesses and sensitivity to deposition parameters. The focus of the cold metal transfer GMAW coatings was on single layer thicknesses and resulting heat affected zone hardness modifications in the hardened steel substrate rather than on the microstructure or hardness of the deposit. The deposition alloy, AWS ER- 307M stainless steel alloy, was chosen in order to easily delineate the fusion boundary profile and is also widely used for corrosion resistance applications.

**PVD/PEMS** coating thickness was targeted at 7 microns. Table 1 lists the coatings deposited, deposition method, thickness, micro and nano measured properties and a summary of the mechanical property evaluation results. It presents a summary analysis of coating hardness and key comparative physical property behavior. Representative optical images for TiN and Cr<sub>2</sub>N are presented in figures 8 and 9. The first at 3,400 x magnification using a Hirox digital imaging microscope and the second a conventional research metallograph using Nomarski imaging in the as-polished condition. The hard coating combined with final polishing using a 0.04micron alumina on a nap cloth rather than on a diamond wheel results in coating surface relief, not evident under bright field imaging but clearly delineated under interference contrast imaging conditions. These images provide an overall uniformity evaluation but cannot reveal fine structure. Figures 10-16 and 18-20 are high resolution scanning electron microscopy images obtained using a FE-SEM. Both top view and cross section views were studied for all coatings. These figures are representative of the various coating morphologies from a top view and fine growth morphology structure in cross section. Typically physical vapor deposition of hard metal nitride coatings is initiated without nitrogen additions as the softer single element metal deposit bonds better to the steel than does a much harder nitride deposit. After initial deposition without nitrogen, the nitrogen gas is introduced into the chamber. This introduction results in transition microstructure change (visible in TEM) and a hardness change which when polished to 0.04 micron alumina results in a surface which can delineate the transitions due to gas additions. If the gas flow rate is changed, as deliberately done for these coatings, the hardness changes remarkably. Generally, lower amounts of N<sub>2</sub> result in increased hardness as TiN becomes Ti<sub>2</sub>N when the nitrogen flow level is reduced by a factor of 2x. A gradient of transitions resulted from manually adjusting the gas flow in increments rather than instantaneously increasing the gas flow in one step.

The deposition process results in aligned columnar growth, figure 11, and depending on deposition conditions and elements significant inter-columnar defects can result. Figure 12, titanium nitride with reduced nitrogen gas resulted in a much finer columnar deposit with correspondingly much finer inter-columnar defects. Defects are not only a function of the element being deposited and the deposition conditions, substrate conditions directly influence coating defects including those that can initiate at the steel substrate and in some cases propagate to the top of the coating, figure13. The surface conditions representative of that shown in figure 13 were prepared by chemical milling rather than mechanical polishing. The coatings tend to very conformal even to chemical milling induced surface roughness and better surface finishes result in improved coating uniformity.

Deposition of TiSiCN or ZrSiCN coatings was more complex with multiple gas additions which results in multiple transition regions between the substrate and the final TiSiCN coating. These are visible in figures 14-15, a comparison of TiSiCN deposited using PVD conditions and PEMS conditions respectively. The PVD results in an extremely fine coating with very fine inter-columnar defects. The PEMS deposition results in a more rapidly deposited coating and a correspondingly coarse columnar structure.

Figure16, a Cr deposition illustrates the influence of deposition parameters relative to the fineness of the deposit. Significantly larger columnar grains with substrate influence on nucleation and growth conditions result with PVD under low bias voltage conditions. Increasing the bias results in a much finer, more uniform deposition. AFM imaging, figure 17 of the same two deposits as in figure 16 confirms the greater uniformity and reduced peak to valley variations. The influence of the plasma assisted magnetron sputtered deposition, PEMS, is evident in figures18-19 and suggests that the combination of bias voltage and plasma can result in the finest and most structure when deposited onto properly prepared surfaces. The influence of low bias voltage during deposition is confirmed in figure 20 for TiN as well.

While high resolution SEM imaging can reveal morphology and process change induced variations, the fine structure was resolved using transmission electron microscopy. Examination of the 7 micron coating and the coating interface presented sample preparation challenges. Conventional methods were not effective due to the thickness of the coatings and sharp chemical variations and major hardness variations between the substrate, initial coating deposit chemistry and the final coating chemistry and hardness. To bypass these issues PSU used a dual beam focused ion beam workstation to ion mill from the top of the deposit across the substrate interface, then ion milled the canyon, cut a section from the cut, transferred the section to a TEM washer, attached the sample to the washer by ion beam deposition of PT to weld the sample to the TEM washer. This was done insitu within the FIB. Once attached the specimen was further ion beam milled to electron transparency thickness with progressively finer milling

action to reduce milling damage, then transferred to a 200kV field emission STEM for analysis. Representative high resolution images at the interface with the substrate, in the coating and revealing microstructural transitions associated with changing gas flows and types during are shown in figures 21-25. For each coating the initial substrate coating interface was deposited without nitrogen gas to result in just a Ti, Cr, or Zr metal, deposit which is considered to provide the best adherence. Then as the deposition continues gas is added and a structural transition or transitions occurs depending on how much and how fast the increase in the gas flow.

Collectively the TEM analysis revealed each transition interface, the absence of any precipitates, ultrafine nano grain sizes, extremely fine voids, and in some cases an amorphous deposit after the transitions have occurred. The ZrSiCN deposit revealed the presence of at least three transition zones before reaching final amorphous coating structure.

In order to verify that the transition structures were due to chemical variations in the deposit samples were analyzed in a LECO Glow Discharge Spectrometer. The coating was sputter depth profiled. The results, shown in figures 26 and 27 confirm the chemical gradients beginning at the iron substrate as well as post deposition oxidation on the coating surface after removal from the PVD system.

**PVD Coating hardness** Coating hardness was determined using both Knoop and victors indenters and by nano indentation measurements on deposit cross sections. For the softer deposits lower indentation loads were required. Each method gave similarly ordered results. Hardness results are shown in the summary table 1. The hardness varied overall by a factor of five. By coating type the CrN coatings were the softest, followed by TiN coatings. Low nitrogen gas flow resulted in much harder deposits than for higher gas flow. Zirconium coatings tended to be the hardest. Overall the hardest coating type was the amorphous zirconium silicon carbide, ZrSiCN. Generally decreasing the N<sub>2</sub> flow rate increased deposition rate and hardness. The Zr coatings had the highest hardness, the highest deposition rates, use a low cost target and are expected to demonstrate high corrosion resistance. Offsetting these advantages in certain applications is the brittle nature of the coating. Of all the coatings the ZrSiCN and ZrN exhibited the least resistance to spalling and cracking at least when deposited at low substrate temperatures, typically about 150°C below conventional temperatures. Nano indentation analysis demonstrated the increased modulus of the coatings relative to the substrate, figure 28. The results of nano indentation measurements are provided in the summary table 1.

**PVD Mechanical strain to failure** Strain to failure is difficult to evaluate without introduction edge crack initiation bias in the test method. PSU's non contact, no edge type of test provided solutions to these problems and allowed just the mechanical strain to failure to be considered. Acoustic emission, optical and SEM analysis of the strained coatings was carried out. Optical metallography is possible but very slow and time consuming requiring extensive image

processing before any quantitative analysis can be conducted. SEM analysis is excellent but requires long hours on the instrument to obtain sufficient data sets at varying strain levels. Additionally quantitative analysis requires extensive post processing image analysis. Overall however it was considered the best approach. Real time acoustic emission analysis during the loading sequence provides AE as a function of both time and load/Strain conditions and is the only practical method for quality control or rapid analysis. For Acoustic emission analysis the number of events, the energy and the amplitude of events were considered. Mechanical induced crack sensitivity was evaluated for baseline uncoated hardened substrates to isolate load train and rubbing acoustic signatures, on baseline electrolytic hard chrome coatings and on PVD deposited Cr, ZrN, ZrSiCN, TiN, and TiSiCN coatings.

The base metal acoustic emission, AE, results showed that AE events were predominantly less than 50db in amplitude and that the amplitude decreased with increasing load. Hence threshold event detection was able to be set above 50db amplitude. For Cr coatings all the AE were above 50db with major increase in AE between 500 and 1000lb load. For the electrolytic hard chromium coating the AE signature contained saturated events above 500lbs representing major high energy crack events at relatively low strains. The coatings were ranked, filtered base on uncoated coupon signatures, and using event amplitude and even energy as ranking criteria. The ranked coating order and the coating hardness was as follows

Lowest AE activity: TiN ( 1400HV)      ZrN ( 1600HV)      and TiSiCN ( 3400HV)

Mid Range AE activity: TiN (1270Hv) Cr (420Hv)

High Range AE Activity: ZrN (4260HV), ZrSiCN (3032 & 1560HV), and TiN (1710Hv)

Highest AE activity: Electrolytic hard chromium (greater than 10 times the others)

Table 1 contains a summary of these findings together with other ranking methods. Figures 29 and 30 are examples of the load-AE response for base metal and for the electrolytic hard chromium deposits. The figures show the incremental load steps, ramp loading, hold time, and ramp unloading schedules. Each incremental load step was done on a new indent and each indent then evaluated optically and using the SEM. The base metal AE signature was stripped from the coated sample AE by filtering based on AE amplitude. The AE assessment provided the most straightforward, fastest, and simplest approach to evaluating mechanical strain to failure thresholds for the coatings and could be adapted to a quality control method using small evaluation coupons prepared concurrently with coatings deposited onto components. This non contact no edge effect on coating crack initiation approach would be applicable to evaluation of all classes of coatings, whether thermal sprayed, cold spray or CVD/PVD.

These samples were then examined in the SEM. Representative images, figures 31-36 were acquired at constant positions relative to the center of the indent and at fixed distances from the center at 0, 90, 18, 270 degrees around the indent. This permitted evaluation at fixed strain levels which were determined using FEA analysis of the deformation induced by a 10mm ball pushed into the opposite side of the 2.5mm thick test coupon. Analysis of the extent of cracking resulted in the following coating rankings divided into most and least crack sensitive. The coating rankings are based on SEM analysis of cracking

| <u>Most crack sensitive</u> | <u>Least crack sensitive</u> |
|-----------------------------|------------------------------|
| Electrolytic Hard Chrome    | ZrSiCN                       |
| TiN                         | ZrN                          |
| TiSiCN                      |                              |

These results are included in the summary table 1 together with other comparative results for select coatings.

#### **PVD Erosion results**

Erosion results were measured in terms of mass loss and also volume loss for erosion impingement angles of 30° and 90°. A sample of the erosion wear scars for 30 degree angle is shown in figure 37. Select coating mass loss data results for both angles are included in the summary comparative table 1. Additionally all the coating results are rank ordered for both angles with the least mass loss ranked #1, in table 4. In some cases multiple coupons for the same coating were tested. Coating deposited using conventional PVD and the Plasma assisted, PEMS, deposition are identified. The impingement angle and the deposition conditions influence the rank order for the specific erodant particle size employed. The PEMS generally resulted in finer columnar growth which would result in more columnar interfaces than for the PVD coatings. The electrolytic hard chromium coatings, EHC, serve as the comparative baseline. For these tests the EHC was in the middle of the rank order. Most of the top 8 ranked coatings were silicon carbo-nitride and especially for the 30 degree impingement angle the pure metals, as expected, performed the worst. The rank order clearly depends on test conditions and could likely depend on erodant particle size and other test factors as well.

#### **PVD Scratch results**

Scratch tests were conducted using PSU's scratch test system. Hysitron and CSM also conducted scratch and nano wear tests on select coatings. The coatings exhibited a full range of scratch test characteristics ranging from no damage to extensive coating failure. Figure 38 shows representative examples of both behaviors. The very hard coatings exhibited spalling and

cracking at the lowest applied scratch loads. Baseline electrolytic hard chromium did not exhibit any coating failure up to the maximum applied load, 100 Newtons. The baseline hardened (HRC53) carbon steel exhibited the widest scratch width and hence scratch depth relative to any of the coatings. Comparative nano wear tests done by traversing a nano indenter to form a wear scratch pad on a baseline uncoated HRC50 Custom 465 steel and on a very hard TiSiCN coating were imaged using an Atomic Force Microscope, figure 39. The coating demonstrated significantly improved wear resistance consistent with scratch test results, figure 40.

A subset of all the PVD coatings was selected for scratch testing. The results are provide in table 3 and ranked from best to worst relative to the critical load to result in damage. The best performance was the ZrN deposited onto chemically etched surface and deposited to result in the maximum hardness of those coatings selected for scratch testing. The baseline electrochemically cleaned (etched) substrate with the electrolytic hard chrome deposit also did not exhibit any cracking up to the maximum applied load. Representative scratch test images for PVD deposited Chromium exhibited no damage, figure 41, and PEMS deposited TiSiCN, little damage, figure 42. The PEMS deposited Zr<sub>2</sub>N coating exhibited spalling failure, figure 43.

### **Cold Metal Transfer**

The Fronius cold metal transfer pulsed GMAW weld system represents the state of art precision low heat input fully digital computer controlled welding system. Designed for robotic welding of thin gage materials with little or no spatter. While normally an automated system, the CMT is now available in a hand held torch. For this project the torch was attached to a controlled travel speed side beam carriage configured with controlled y- motion and a micrometer based x- adjustment. More than 50 weld passes each representing different weld parameters or plate thicknesses were made for the purpose of establishing the minimum heat inputs and single layer thicknesses on 4 different fully hardened 4142 steel plate material - 1.27mm, 2.0mm, 3.2mm, 6.35mm. Overall the range in welding parameters covered the following ranges

|                   |                                      |
|-------------------|--------------------------------------|
| Plate thickness   | 1.27 - 6.35mm                        |
| Electrode wire    | AWS ER 307M (constant)               |
| Shielding gas     | 90-10% and 98-2% Ar- CO <sup>2</sup> |
| Voltage           | 11.9 -21.6 volts                     |
| Amperage          | 106- 171 amperage                    |
| Wire feed speed   | 457 - 660 cm/min                     |
| Weld travel speed | 71 - 142 cm/min                      |
| Heat Input        | 0.066 - 0.283 Kj/mm                  |

Analysis of all welding conditions and plate thicknesses resulted in the following single pass bead sizes and shapes

bead height varied from 1.22 - 2.24 mm

bead width varied from 4.32 - 7.62 mm

bead height/width ratio varied from 5.1 - 12.3 mm

The minimum and maximum bead penetrations were obtained for the following two sets of conditions

|                   | <b>Minimum penetration</b> | <b>Maximum penetration</b> |
|-------------------|----------------------------|----------------------------|
| bead penetration  | 0.127mm                    | 2.29mm                     |
| plate thickness   | 2mm                        | 2mm                        |
| electrode wire    | AWS ER 307M (constant)     |                            |
| shielding gas     | 98-2% Ar- CO <sup>2</sup>  | 90-10% Ar- CO <sup>2</sup> |
| voltage           | 11.9 volts                 | 16.7 volts                 |
| Amperage          | 108 amperage               | 168 amperage               |
| Wire feed speed   | 457 cm/min                 | 660cm/min                  |
| Weld travel speed | 1 16 cm/min                | 711cm/min                  |
| Heat Input        | 0.066 Kj/mm                | 0.235Kj/mm                 |

The penetration versus heat input response is shown in figure 44. All plate thicknesses are included in the figure. The figure shows a wide range of heat inputs versus penetration and wide range of penetration for a fixed heat input. This is due to the range of plate thicknesses included in the figure and also the preprogrammed CMT logic, is not operator controllable. The CMT process is computer controlled and preprogrammed by Fronius. Operator inputs include plate material and thickness, wire chemistry, and shielding gas. Preprogrammed logic sets the voltage, wire feed speed in response to system data acquisition during welding. If the operator varies the travel speed or stick out, the system responds instantly to attempt to maintain optimum welding conditions. Operators have very minimal ability to adjust voltage or wire feed rates. At the outset this limited operator ability to independently adjust parameters such as the pulse rate or pulse duration for welding research purposes was unclear. This level of welding optimization and study would require a CMT R/D development system and not a commercial

system with preprogrammed weld optimization integral to the operating control system. Alternatively a selectable program logic, one for joining and one optimized for surfacing would enable optimized systems for both applications.

Figure 45 is a summary figure for all weld passes for all thicknesses. The data is arranged to show increasing bead height from left to right, since a primary objective was to establish the minimum thickness layer that might be achieved using CMT. Assessing maximum productivity as considered by weld travel speed while also considering heat input can also be done using this figure. The amount of tabular data for these welds and that was used to generate these figures is extensive and not practical to include individual results tables in this report.

In addition to bead height, penetration depth and profile of CMT deposits as an indicators of the potential for CMT surfacing for corrosion, wear, or dimensional tolerance restoration, figures 46 and 47 provide hardness depth profiles on 2mm and 6.35mm thick 4142 hardened plate, HK<sub>500gm</sub>530. These were the thinnest and thickest plated studied. In all cases the austenitic weld metal was soft as expected. The near fusion line heat affected zone was solution heat treated and rapidly quenched due to the low heat input nature of the CMT process. For even the thinnest section martensite formed in the heat affected zone, HK<sub>500gm</sub> over 520, at a depth at least equivalent to the depth in the thickest plate. Thus even though the thin plate would normally cool the slowest and require less preheat to avoid martensite, the thinnest plate experienced a heat affected zone cooling rate at least as fast as the thicker plate and would require the same preheat as would thick plate when being surfaced in order to avoid martensite in the HAZ. Representative images of the hardened AISI 4142 and the CMT induced coarse and fine grained microstructures are provided in figure 48 and 49. A representative cross section image of a 6 pass single layer surface deposit is presented in figure 50. A heat affected zone hardness profile parallel to the plate surface and taken along the line marked by the horizontal line in the HAZ is superimposed on the weld image. The substrate was A36 steel in this case and the HAZ hardness profile was consistent with the variable HAZ depth between adjacent weld passes.

## Summary

This project considered two surfacing technologies, one utilizing magnetron sputtering physical vapor deposition, PVD, and the other an emerging advanced low heat input gas metal arc welding, patented by Fronius, named Cold Metal Transfer, CMT. The PVD process traditionally heats the substrate to about 400°C, precluding PVD on fully hardened low alloy steels. This project considered a range of PVD hard coatings and deposition conditions, including plasma assisted, all at substrate temperatures of 250°C. At this temperature the initial substrate hardness, HRC 52 was maintained. One potential application of this reduced



substrate temperature is as a replacement for electrolytic hard chrome coatings. Evaluation of the properties of the PVD coatings was benchmarked to traditional hexavalent deposited chromium. Coatings were deposited by Southwest Research Institute under Dr Ronghua Wei's leadership. In addition to conventional PVD, coatings were deposited using plasma enhanced magnetron sputtering, PEMS. Coatings were evaluated chemically, microstructurally and mechanically via scratch, erosion, and mechanical strain induced failure. Coating hardness varied from HK400 to about HK4000. The coatings were ranked by each evaluation criteria and the results for select coatings included in a summary table. The optimum coating choice depends in part on which specific evaluation criteria is most important. Some of the coatings performed better than the chromium benchmark. The results indicate that deposition and coating types can be tailored using the low temperature PVD and PEMS process can be considered for replacement of traditional hard chrome coatings for wear and corrosion resistance.

The CMT patented low heat input pulsed GMAW welding process is designed for spatter free joining of very thin metals including aluminum and titanium. Its uniquely designed features suggest its potential application for low heat input surfacing. A range of process deposition parameters were evaluated by deposition onto quench and tempered AISI 4142 steel, HK<sub>500gm</sub> 533 with thicknesses between 2mm and 6.35mm. Single pass layer thicknesses ranged from 1-2mm. The CMT's preprogrammed digital computer based control system presented challenges for establishing the minimum potential heat input and layer thickness. The preprogrammed logic is designed for joining, not surfacing and optimization for surfacing would benefit by permitting the end user access to control algorithms that could lead to thinner single layer deposits with even lower heat input than achieved in this effort, 0.065Kj/mm, (1.65Kj/in).

Table 1, Summary table for coating evaluation

| Select coatings comparative assessment |  |  |  |  |  |  |  |  |  |  |  |  |  |  |  |  |  |  |  |  |  |  |  |  |  |  |  |  |  |  |  |  |  |  |  |  |  |  |  |  |  |  |  |  |  |  |  |  |  |  |  |  |  |  |  |  |  |  |  |  |  |  |  |  |  |  |  |  |  |  |  |  |  |  |  |  |  |  |  |  |  |  |  |  |  |  |  |  |  |  |  |  |  |  |  |  |  |  |  |  |  |  |  |  |  |  |  |  |  |  |  |  |  |  |  |  |  |  |  |  |  |  |  |  |  |  |  |  |  |  |  |  |  |  |  |  |  |  |  |  |  |  |  |  |  |  |  |  |  |  |  |  |  |  |  |  |  |  |  |  |  |  |  |  |  |  |  |  |  |  |  |  |  |  |  |  |  |  |  |  |  |  |  |  |  |  |  |  |  |  |  |  |  |  |  |  |  |  |  |  |  |  |  |  |  |  |  |  |  |  |  |  |  |  |  |  |  |  |  |  |  |  |  |  |  |  |  |  |  |  |  |  |  |  |  |  |  |  |  |  |  |  |  |  |  |  |  |  |  |  |  |  |  |  |  |  |  |  |  |  |  |  |  |  |  |  |  |  |  |  |  |  |  |  |  |  |  |  |  |  |  |  |  |  |  |  |  |  |  |  |  |  |  |  |  |  |  |  |  |  |  |  |  |  |  |  |  |  |  |  |  |  |  |  |  |  |  |  |  |  |  |  |  |  |  |  |  |  |  |  |  |  |  |  |  |  |  |  |  |  |  |  |  |  |  |  |  |  |  |  |  |  |  |  |  |  |  |  |  |  |  |  |  |  |  |  |  |  |  |  |  |  |  |  |  |  |  |  |  |  |  |  |  |  |  |  |  |  |  |  |  |  |  |  |  |  |  |  |  |  |  |  |  |  |  |  |  |  |  |  |  |  |  |  |  |  |  |  |  |  |  |  |  |  |  |  |  |  |  |  |  |  |  |  |  |  |  |  |  |  |  |  |  |  |  |  |  |  |  |  |  |  |  |  |  |  |  |  |  |  |  |  |  |  |  |  |  |  |  |  |  |  |  |  |  |  |  |  |  |  |  |  |  |  |  |  |  |  |  |  |  |  |  |  |  |  |  |  |  |  |  |  |  |  |  |  |  |  |  |  |  |  |  |  |  |  |  |  |  |  |  |  |  |  |  |  |  |  |  |  |  |  |  |  |  |  |  |  |  |  |  |  |  |  |  |  |  |  |  |  |  |  |  |  |  |  |  |  |  |  |  |  |  |  |  |  |  |  |  |  |  |  |  |  |  |  |  |  |  |  |  |  |  |  |  |  |  |  |  |  |  |  |  |  |  |  |  |  |  |  |  |  |  |  |  |  |  |  |  |  |  |  |  |  |  |  |  |  |  |  |  |  |  |  |  |  |  |  |  |  |  |  |  |  |  |  |  |  |  |  |  |  |  |  |  |  |  |  |  |  |  |  |  |  |  |  |  |  |  |  |  |  |  |  |  |  |  |  |  |  |  |  |  |  |  |  |  |  |  |  |  |  |  |  |  |  |  |  |  |  |  |  |  |  |  |  |  |  |  |  |  |  |  |  |  |  |  |  |  |  |  |  |  |  |  |  |  |  |  |  |  |  |  |  |  |  |  |  |  |  |  |  |  |  |  |  |  |  |  |  |  |  |  |  |  |  |  |  |  |  |  |  |  |  |  |  |  |  |  |  |  |  |  |  |  |  |  |  |  |  |  |  |  |  |  |  |  |  |  |  |  |  |  |  |  |  |  |  |  |  |  |  |  |  |  |  |  |  |  |  |  |  |  |  |  |  |  |  |  |  |  |  |  |  |  |  |  |  |  |  |  |  |  |  |  |  |  |  |  |  |  |  |  |  |  |  |  |  |  |  |  |  |  |  |  |  |  |  |  |  |  |  |  |  |  |  |  |  |  |  |  |  |  |  |  |  |  |  |  |  |  |  |  |  |  |  |  |  |  |  |  |  |  |  |  |  |  |  |  |  |  |  |  |  |  |  |  |  |  |  |  |  |  |  |  |  |  |  |  |  |  |  |  |  |  |  |  |  |  |  |  |  |  |  |  |  |  |  |  |  |  |  |  |  |  |  |  |  |  |  |  |  |  |  |  |  |  |  |  |  |  |  |  |  |  |  |  |  |  |  |  |  |  |  |  |  |  |  |  |  |  |  |  |  |  |  |  |  |  |  |  |  |  |  |  |  |  |  |  |  |  |  |  |  |  |  |  |  |  |  |  |  |  |  |  |  |  |  |  |  |  |  |  |  |  |  |  |  |  |  |  |  |  |  |  |  |  |  |  |  |  |  |  |  |  |  |  |  |  |  |  |  |  |  |  |  |  |  |  |  |  |  |  |  |  |  |  |  |  |  |  |  |  |  |  |  |  |  |  |  |  |  |  |  |  |  |  |  |  |  |  |  |  |  |  |  |  |  |  |  |  |  |  |  |  |  |  |  |  |  |  |  |  |  |  |  |  |  |  |  |  |  |  |  |  |  |  |  |  |  |  |  |  |  |  |  |  |  |  |  |  |  |  |  |  |  |  |  |  |  |  |  |  |  |  |  |  |  |  |  |  |  |  |  |  |  |  |  |  |  |  |  |  |  |  |  |  |  |  |  |  |  |  |  |  |  |  |  |  |  |  |  |  |  |  |  |  |  |  |  |  |  |  |  |  |  |  |  |  |  |  |  |  |  |  |  |  |  |  |  |  |  |  |  |  |  |  |  |  |  |  |  |  |  |  |  |  |  |  |  |  |  |  |  |  |  |  |  |  |  |  |  |  |  |  |  |  |  |  |  |  |  |  |  |  |  |  |  |  |  |  |  |  |  |  |  |  |  |  |  |  |  |  |  |  |  |  |  |  |  |  |  |  |  |  |  |  |  |  |  |  |  |  |  |  |  |  |  |  |  |  |  |  |  |  |  |  |  |  |  |  |  |  |  |  |  |  |  |  |  |  |  |  |  |  |  |  |  |  |  |  |  |  |  |  |  |  |  |  |  |  |  |  |  |  |  |  |  |  |  |  |  |  |  |  |  |  |  |  |  |  |  |  |  |  |  |  |  |  |  |  |  |  |  |  |  |  |  |  |  |  |  |  |  |  |  |  |  |  |  |  |  |  |  |  |  |  |  |  |  |  |  |  |  |  |  |  |  |  |  |  |  |  |  |  |  |  |  |  |  |  |  |  |  |  |  |  |  |  |  |  |  |  |  |  |  |  |  |  |  |  |  |  |  |  |  |  |  |  |  |  |  |  |  |  |  |  |  |  |  |  |  |  |  |  |  |  |  |  |  |  |  |  |
|--|--|--|--|--|--|--|--|--|--|--|--|--|--|--|--|--|--|--|--|--|--|--|--|--|--|--|--|--|--|--|--|--|--|--|--|--|--|--|--|--|--|--|--|--|--|--|--|--|--|--|--|--|--|--|--|--|--|--|--|--|--|--|--|--|--|--|--|--|--|--|--|--|--|--|--|--|--|--|--|--|--|--|--|--|--|--|--|--|--|--|--|--|--|--|--|--|--|--|--|--|--|--|--|--|--|--|--|--|--|--|--|--|--|--|--|--|--|--|--|--|--|--|--|--|--|--|--|--|--|--|--|--|--|--|--|--|--|--|--|--|--|--|--|--|--|--|--|--|--|--|--|--|--|--|--|--|--|--|--|--|--|--|--|--|--|--|--|--|--|--|--|--|--|--|--|--|--|--|--|--|--|--|--|--|--|--|--|--|--|--|--|--|--|--|--|--|--|--|--|--|--|--|--|--|--|--|--|--|--|--|--|--|--|--|--|--|--|--|--|--|--|--|--|--|--|--|--|--|--|--|--|--|--|--|--|--|--|--|--|--|--|--|--|--|--|--|--|--|--|--|--|--|--|--|--|--|--|--|--|--|--|--|--|--|--|--|--|--|--|--|--|--|--|--|--|--|--|--|--|--|--|--|--|--|--|--|--|--|--|--|--|--|--|--|--|--|--|--|--|--|--|--|--|--|--|--|--|--|--|--|--|--|--|--|--|--|--|--|--|--|--|--|--|--|--|--|--|--|--|--|--|--|--|--|--|--|--|--|--|--|--|--|--|--|--|--|--|--|--|--|--|--|--|--|--|--|--|--|--|--|--|--|--|--|--|--|--|--|--|--|--|--|--|--|--|--|--|--|--|--|--|--|--|--|--|--|--|--|--|--|--|--|--|--|--|--|--|--|--|--|--|--|--|--|--|--|--|--|--|--|--|--|--|--|--|--|--|--|--|--|--|--|--|--|--|--|--|--|--|--|--|--|--|--|--|--|--|--|--|--|--|--|--|--|--|--|--|--|--|--|--|--|--|--|--|--|--|--|--|--|--|--|--|--|--|--|--|--|--|--|--|--|--|--|--|--|--|--|--|--|--|--|--|--|--|--|--|--|--|--|--|--|--|--|--|--|--|--|--|--|--|--|--|--|--|--|--|--|--|--|--|--|--|--|--|--|--|--|--|--|--|--|--|--|--|--|--|--|--|--|--|--|--|--|--|--|--|--|--|--|--|--|--|--|--|--|--|--|--|--|--|--|--|--|--|--|--|--|--|--|--|--|--|--|--|--|--|--|--|--|--|--|--|--|--|--|--|--|--|--|--|--|--|--|--|--|--|--|--|--|--|--|--|--|--|--|--|--|--|--|--|--|--|--|--|--|--|--|--|--|--|--|--|--|--|--|--|--|--|--|--|--|--|--|--|--|--|--|--|--|--|--|--|--|--|--|--|--|--|--|--|--|--|--|--|--|--|--|--|--|--|--|--|--|--|--|--|--|--|--|--|--|--|--|--|--|--|--|--|--|--|--|--|--|--|--|--|--|--|--|--|--|--|--|--|--|--|--|--|--|--|--|--|--|--|--|--|--|--|--|--|--|--|--|--|--|--|--|--|--|--|--|--|--|--|--|--|--|--|--|--|--|--|--|--|--|--|--|--|--|--|--|--|--|--|--|--|--|--|--|--|--|--|--|--|--|--|--|--|--|--|--|--|--|--|--|--|--|--|--|--|--|--|--|--|--|--|--|--|--|--|--|--|--|--|--|--|--|--|--|--|--|--|--|--|--|--|--|--|--|--|--|--|--|--|--|--|--|--|--|--|--|--|--|--|--|--|--|--|--|--|--|--|--|--|--|--|--|--|--|--|--|--|--|--|--|--|--|--|--|--|--|--|--|--|--|--|--|--|--|--|--|--|--|--|--|--|--|--|--|--|--|--|--|--|--|--|--|--|--|--|--|--|--|--|--|--|--|--|--|--|--|--|--|--|--|--|--|--|--|--|--|--|--|--|--|--|--|--|--|--|--|--|--|--|--|--|--|--|--|--|--|--|--|--|--|--|--|--|--|--|--|--|--|--|--|--|--|--|--|--|--|--|--|--|--|--|--|--|--|--|--|--|--|--|--|--|--|--|--|--|--|--|--|--|--|--|--|--|--|--|--|--|--|--|--|--|--|--|--|--|--|--|--|--|--|--|--|--|--|--|--|--|--|--|--|--|--|--|--|--|--|--|--|--|--|--|--|--|--|--|--|--|--|--|--|--|--|--|--|--|--|--|--|--|--|--|--|--|--|--|--|--|--|--|--|--|--|--|--|--|--|--|--|--|--|--|--|--|--|--|--|--|--|--|--|--|--|--|--|--|--|--|--|--|--|--|--|--|--|--|--|--|--|--|--|--|--|--|--|--|--|--|--|--|--|--|--|--|--|--|--|--|--|--|--|--|--|--|--|--|--|--|--|--|--|--|--|--|--|--|--|--|--|--|--|--|--|--|--|--|--|--|--|--|--|--|--|--|--|--|--|--|--|--|--|--|--|--|--|--|--|--|--|--|--|--|--|--|--|--|--|--|--|--|--|--|--|--|--|--|--|--|--|--|--|--|--|--|--|--|--|--|--|--|--|--|--|--|--|--|--|--|--|--|--|--|--|--|--|--|--|--|--|--|--|--|--|--|--|--|--|--|--|--|--|--|--|--|--|--|--|--|--|--|--|--|--|--|--|--|--|--|--|--|--|--|--|--|--|--|--|--|--|--|--|--|--|--|--|--|--|--|--|--|--|--|--|--|--|--|--|--|--|--|--|--|--|--|--|--|--|--|--|--|--|--|--|--|--|--|--|--|--|--|--|--|--|--|--|--|--|--|--|--|--|--|--|--|--|--|--|--|--|--|--|--|--|--|--|--|--|--|--|--|--|--|--|--|--|--|--|--|--|--|--|--|--|--|--|--|--|--|--|--|--|--|--|--|--|--|--|--|--|--|--|--|--|--|--|--|--|--|--|--|--|--|--|--|--|--|--|--|--|--|--|--|--|--|--|--|--|--|--|--|--|--|--|--|--|--|--|--|--|--|--|--|--|--|--|--|--|--|--|--|--|--|--|--|--|--|--|--|--|--|--|--|--|--|--|--|--|--|--|--|--|--|--|--|--|--|--|--|--|--|--|--|--|--|--|--|--|--|--|--|--|--|--|--|--|--|--|--|--|--|--|--|--|--|--|--|--|--|--|--|--|--|--|--|--|--|--|--|--|--|--|--|--|--|--|--|--|--|--|--|--|--|--|--|--|--|--|--|--|--|--|--|--|--|--|--|--|--|--|--|--|--|--|--|--|--|--|--|
|--|--|--|--|--|--|--|--|--|--|--|--|--|--|--|--|--|--|--|--|--|--|--|--|--|--|--|--|--|--|--|--|--|--|--|--|--|--|--|--|--|--|--|--|--|--|--|--|--|--|--|--|--|--|--|--|--|--|--|--|--|--|--|--|--|--|--|--|--|--|--|--|--|--|--|--|--|--|--|--|--|--|--|--|--|--|--|--|--|--|--|--|--|--|--|--|--|--|--|--|--|--|--|--|--|--|--|--|--|--|--|--|--|--|--|--|--|--|--|--|--|--|--|--|--|--|--|--|--|--|--|--|--|--|--|--|--|--|--|--|--|--|--|--|--|--|--|--|--|--|--|--|--|--|--|--|--|--|--|--|--|--|--|--|--|--|--|--|--|--|--|--|--|--|--|--|--|--|--|--|--|--|--|--|--|--|--|--|--|--|--|--|--|--|--|--|--|--|--|--|--|--|--|--|--|--|--|--|--|--|--|--|--|--|--|--|--|--|--|--|--|--|--|--|--|--|--|--|--|--|--|--|--|--|--|--|--|--|--|--|--|--|--|--|--|--|--|--|--|--|--|--|--|--|--|--|--|--|--|--|--|--|--|--|--|--|--|--|--|--|--|--|--|--|--|--|--|--|--|--|--|--|--|--|--|--|--|--|--|--|--|--|--|--|--|--|--|--|--|--|--|--|--|--|--|--|--|--|--|--|--|--|--|--|--|--|--|--|--|--|--|--|--|--|--|--|--|--|--|--|--|--|--|--|--|--|--|--|--|--|--|--|--|--|--|--|--|--|--|--|--|--|--|--|--|--|--|--|--|--|--|--|--|--|--|--|--|--|--|--|--|--|--|--|--|--|--|--|--|--|--|--|--|--|--|--|--|--|--|--|--|--|--|--|--|--|--|--|--|--|--|--|--|--|--|--|--|--|--|--|--|--|--|--|--|--|--|--|--|--|--|--|--|--|--|--|--|--|--|--|--|--|--|--|--|--|--|--|--|--|--|--|--|--|--|--|--|--|--|--|--|--|--|--|--|--|--|--|--|--|--|--|--|--|--|--|--|--|--|--|--|--|--|--|--|--|--|--|--|--|--|--|--|--|--|--|--|--|--|--|--|--|--|--|--|--|--|--|--|--|--|--|--|--|--|--|--|--|--|--|--|--|--|--|--|--|--|--|--|--|--|--|--|--|--|--|--|--|--|--|--|--|--|--|--|--|--|--|--|--|--|--|--|--|--|--|--|--|--|--|--|--|--|--|--|--|--|--|--|--|--|--|--|--|--|--|--|--|--|--|--|--|--|--|--|--|--|--|--|--|--|--|--|--|--|--|--|--|--|--|--|--|--|--|--|--|--|--|--|--|--|--|--|--|--|--|--|--|--|--|--|--|--|--|--|--|--|--|--|--|--|--|--|--|--|--|--|--|--|--|--|--|--|--|--|--|--|--|--|--|--|--|--|--|--|--|--|--|--|--|--|--|--|--|--|--|--|--|--|--|--|--|--|--|--|--|--|--|--|--|--|--|--|--|--|--|--|--|--|--|--|--|--|--|--|--|--|--|--|--|--|--|--|--|--|--|--|--|--|--|--|--|--|--|--|--|--|--|--|--|--|--|--|--|--|--|--|--|--|--|--|--|--|--|--|--|--|--|--|--|--|--|--|--|--|--|--|--|--|--|--|--|--|--|--|--|--|--|--|--|--|--|--|--|--|--|--|--|--|--|--|--|--|--|--|--|--|--|--|--|--|--|--|--|--|--|--|--|--|--|--|--|--|--|--|--|--|--|--|--|--|--|--|--|--|--|--|--|--|--|--|--|--|--|--|--|--|--|--|--|--|--|--|--|--|--|--|--|--|--|--|--|--|--|--|--|--|--|--|--|--|--|--|--|--|--|--|--|--|--|--|--|--|--|--|--|--|--|--|--|--|--|--|--|--|--|--|--|--|--|--|--|--|--|--|--|--|--|--|--|--|--|--|--|--|--|--|--|--|--|--|--|--|--|--|--|--|--|--|--|--|--|--|--|--|--|--|--|--|--|--|--|--|--|--|--|--|--|--|--|--|--|--|--|--|--|--|--|--|--|--|--|--|--|--|--|--|--|--|--|--|--|--|--|--|--|--|--|--|--|--|--|--|--|--|--|--|--|--|--|--|--|--|--|--|--|--|--|--|--|--|--|--|--|--|--|--|--|--|--|--|--|--|--|--|--|--|--|--|--|--|--|--|--|--|--|--|--|--|--|--|--|--|--|--|--|--|--|--|--|--|--|--|--|--|--|--|--|--|--|--|--|--|--|--|--|--|--|--|--|--|--|--|--|--|--|--|--|--|--|--|--|--|--|--|--|--|--|--|--|--|--|--|--|--|--|--|--|--|--|--|--|--|--|--|--|--|--|--|--|--|--|--|--|--|--|--|--|--|--|--|--|--|--|--|--|--|--|--|--|--|--|--|--|--|--|--|--|--|--|--|--|--|--|--|--|--|--|--|--|--|--|--|--|--|--|--|--|--|--|--|--|--|--|--|--|--|--|--|--|--|--|--|--|--|--|--|--|--|--|--|--|--|--|--|--|--|--|--|--|--|--|--|--|--|--|--|--|--|--|--|--|--|--|--|--|--|--|--|--|--|--|--|--|--|--|--|--|--|--|--|--|--|--|--|--|--|--|--|--|--|--|--|--|--|--|--|--|--|--|--|--|--|--|--|--|--|--|--|--|--|--|--|--|--|--|--|--|--|--|--|--|--|--|--|--|--|--|--|--|--|--|--|--|--|--|--|--|--|--|--|--|--|--|--|--|--|--|--|--|--|--|--|--|--|--|--|--|--|--|--|--|--|--|--|--|--|--|--|--|--|--|--|--|--|--|--|--|--|--|--|--|--|--|--|--|--|--|--|--|--|--|--|--|--|--|--|--|--|--|--|--|--|--|--|--|--|--|--|--|--|--|--|--|--|--|--|--|--|--|--|--|--|--|--|--|--|--|--|--|--|--|--|--|--|--|--|--|--|--|--|--|--|--|--|--|--|--|--|--|--|--|--|--|--|--|--|--|--|--|--|--|--|--|--|--|--|--|--|--|--|--|--|--|--|--|--|--|--|--|--|--|--|--|--|--|--|--|--|--|--|--|--|--|--|--|--|--|--|--|--|--|--|--|--|--|--|--|--|--|--|--|--|--|--|--|--|--|--|--|--|--|--|--|--|--|--|--|--|--|--|--|--|--|--|--|--|--|--|--|--|--|--|--|--|--|--|--|--|--|--|--|--|--|--|--|--|--|--|--|--|--|--|--|--|--|--|--|--|--|--|--|--|--|--|--|--|--|--|--|--|--|--|--|

Table 2 ranked erosion volume loss per gram erodant

|      | Coating | 30 degree<br>volume loss ranking, 1 = least loss | 90 degree<br>volume loss ranking, 1 = least loss |
|------|---------|--|--|
| PEMS | TiSiCN  | 1  | 4  |
| PVD  | ZrN     | 2  | 2  |
| PVD  | ZrSiCN  | 3  | 8  |
| PEMS | ZrN     | 4  | 37   |
| PVD  | TiSiCN  | 5  | 11   |
| PEMS | ZrSiCN  | 6  | 3  |
| PVD  | TiSiCN  | 7  | 1  |
| PEMS | ZrSiCN  | 8  | 31   |
| PVD  | ZrN     | 9  | 5  |
| PVD  | TiN     | 10   | 9  |
|      | EHC     | 11   | 42   |
| PEMS | TiSiCN  | 12   | 20   |
| PVD  | ZrN     | 13   | 30   |
| PEMS | CrN     | 14   | NA   |
| PEMS | TiN     | 15   | 28   |
| PVD  | ZrSiCN  | 16   | 38   |
| PEMS | ZrSiCN  | 17   | 40   |
| PVD  | Ti      | 18   | 29   |
| PEMS | Cr2N    | 19   | NA   |
| PVD  | Cr      | 20   | NA   |
| PEMS | Cr      | 21   | 35   |
| PVD  | Cr2N    | 22   | 32   |
| PEMS | Cr      | 23   | 24   |
|      | EHC     | 24   | 34   |
|      | EHC     | 25   | 44   |
| PEMS | Cr      | 26   | 15   |
| PVD  | TiN     | 27   | 38   |
| PEMS | TiN     | 28   | 37   |
| PVD  | CrN     | 29   | 45   |
| PVD  | ZrSiCN  | 30   | 43   |
| PVD  | Ti      | 31   | 33   |
| PEMS | Ti      | 32   | 6  |
| PEMS | Ti      | 33   | 36   |
| PVD  | Ti      | 34   | 18   |
|      | DLC     | 35   | 14   |
| PEMS | Zr      | 36   | 25   |
| PVD  | Zr      | 37   | 8  |
| PEMS | Zr      | 38   | 22   |
| PEMS | Zr      | 39   | 27   |
| PEMS | TiN     | 40   | NA   |
|      |         |  |  |
|      |         |  |  |

Table 3, Scratch test for select coatings ranked by critical load to result in coating failure

| ID & surface prep | coating | AVG,mm | STD DEV,mm | Scratch width, mm | HV   | Critical Load, Newtons |
|-------------------|---------|--------|------------|-------------------|------|------------------------|
| 20 ECM            | ZrN     | 0      | 0.00       | 0.3               | 4260 | >100                   |
| 33 Polished       | Ti      | 0      | 0.00       | 0.35              | 440  | >100                   |
| 31 Polished       | Ti      | 0      | 0.00       | 0.4               | 370  | >100                   |
| 5 ECM             | Cr      | 0      | 0.00       | 0.4               | 365  | >100                   |
| 17 ECM            | Zr      | 0.64   | 1.34       | 0.4               | 445  | 94                     |
| 17 Polished       | Zr      | 1.17   | 2.15       | 0.4               | 445  | 88                     |
| 9 ECM             | Cr2N    | 1.27   | 1.48       | 0.5               | 810  | 87                     |
| 3 Polished        | Cr      | 1.77   | 1.09       | 0.5               | 425  | 82                     |
| 21 ECM            | ZrN     | 2.74   | 4.06       | 0.4               | 1640 | 73                     |
| 3 ECM             | Cr      | 2.8    | 2.82       | 0.4               | 445  | 72                     |
| 40 ECM            | TiSiCN  | 2.96   | 1.69       | 0.3               | 2000 | 70                     |
| 31 ECM            | Ti      | 3.47   | 1.76       | 0.4               | 370  | 65                     |
| 37 Polished       | TiN     | 4.1    | 4.34       | 0.3               | 1400 | 59                     |
| 32 ECM            | Ti      | 4.37   | 5.44       | 0.4               | 385  | 56                     |
| 26 ECM            | ZrSiCN  | 4.63   | 3.59       | 0.4               | 3950 | 54                     |
| 10 Polished       | CrN     | 6.88   | 3.09       | 0.5               | 810  | 31                     |
| 26 Polished       | ZrSiCN  | 7.23   | 1.68       | 0.45              | 3950 | 28                     |

notes: ECM = electrochemically milled; polished = 1 micron finish  
10mm scratch length with linear progressive load 0-100 newtons

AVG = averaged distance, mm, from end of scratch marking the start of coating adhesive/spalling failure

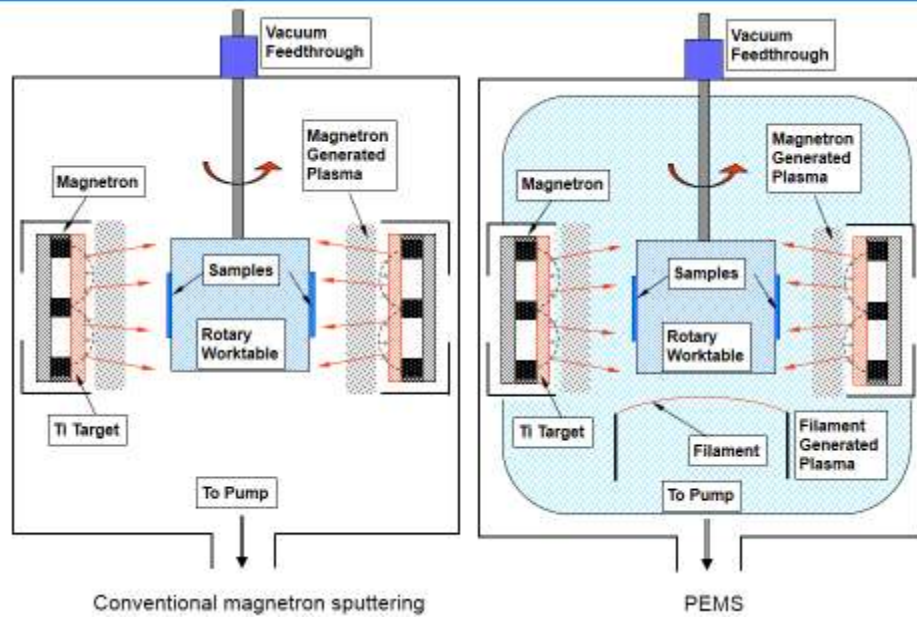


Figure 1, conventional magnetron sputtered and plasma assisted magnetron sputtered, PEMS used at Southwest Research Institute



Figure 2, (a) CMT weld configuration with CMT GMAW torch (b) welded coupon held in fixture with thermocouple wires welded to bottom of plate

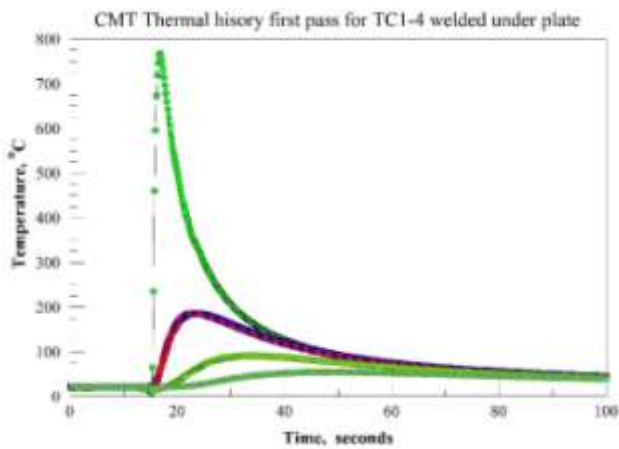


Figure 3, thermocouple record under .125" thick plate; 4 TCs highest temperature is directly under first pass; TC 2-4 located under next 3 pass positions showing peak temperatures due to adjacent passes to be less than the plate tempering thermal history

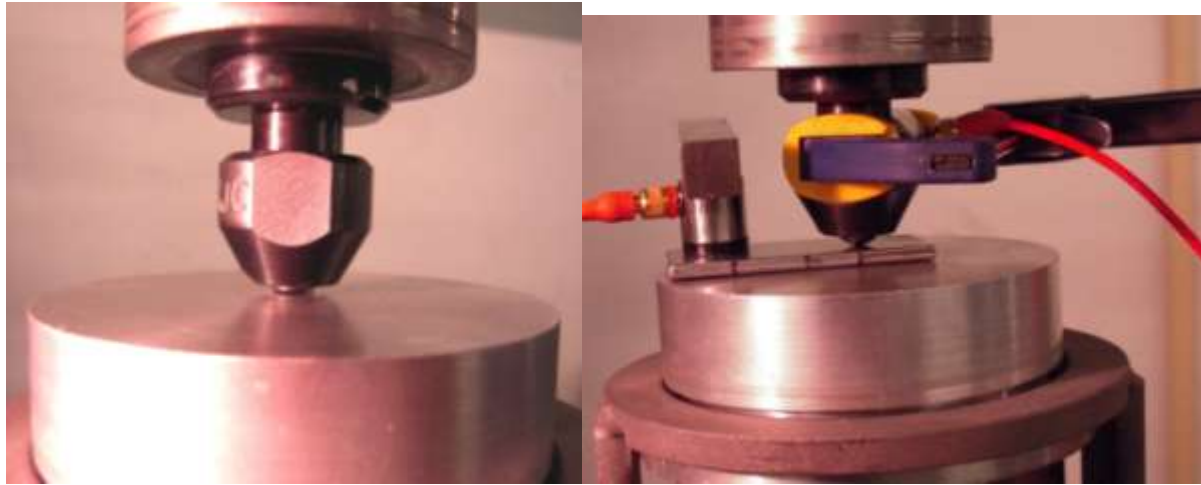


Figure 4, Back side bulge test fixture; 10mm carbide ball indenting 100 alloy aluminum to create deep impression; after retracting indenter the test coupon was placed in position and loaded to predetermined load level; back side bulge formed in the aluminum dimple which was much larger and deeper than the coated hardened steel ( HRC 53); load applied using computer controlled 200kip Instron load frame; load, displacement, acoustic emission on sample and indenter and time recorded for each test

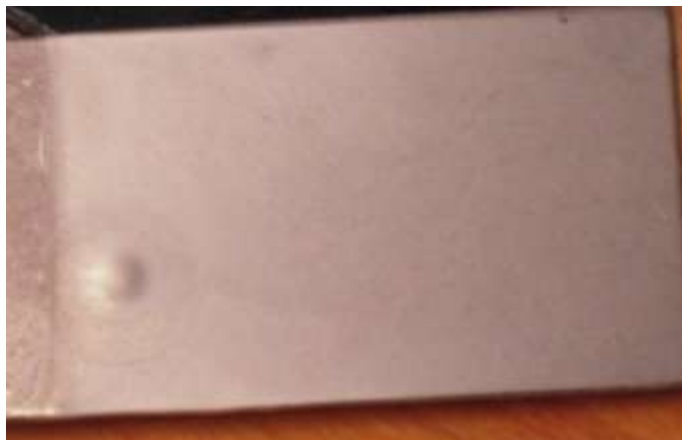


Figure 5, Backside of bulge indent showing uniform non contact deformation of electrolytic hard chrome coating



Figure 6, Mass erodant particle flow controller



Figure 7, Erosion test setup with 30 degree impingement





Figure 8, TiN optical image using HIROX microscope, 3,400x



Figure 9, Cr<sub>2</sub>N PEMS deposit, Optical interference contrast image 1,000x

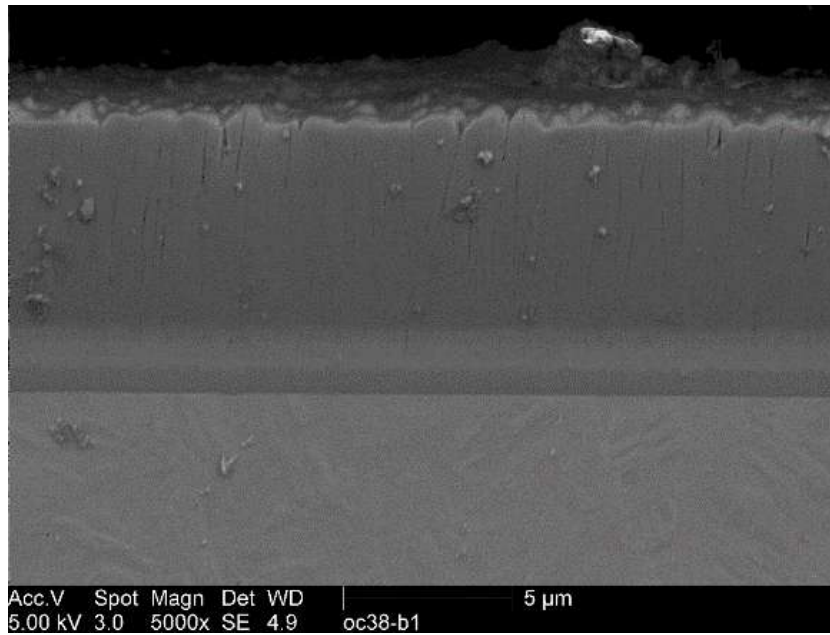


Figure 10, TiN PEMS, SEM cross section image, 5,000x

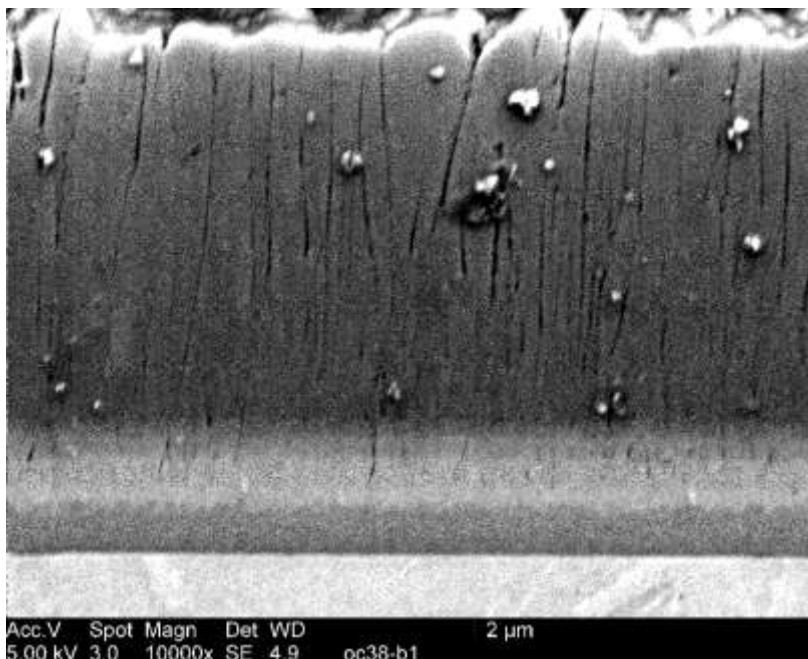


Figure 11, TiN PEMS cross section SEM image, 10,000x

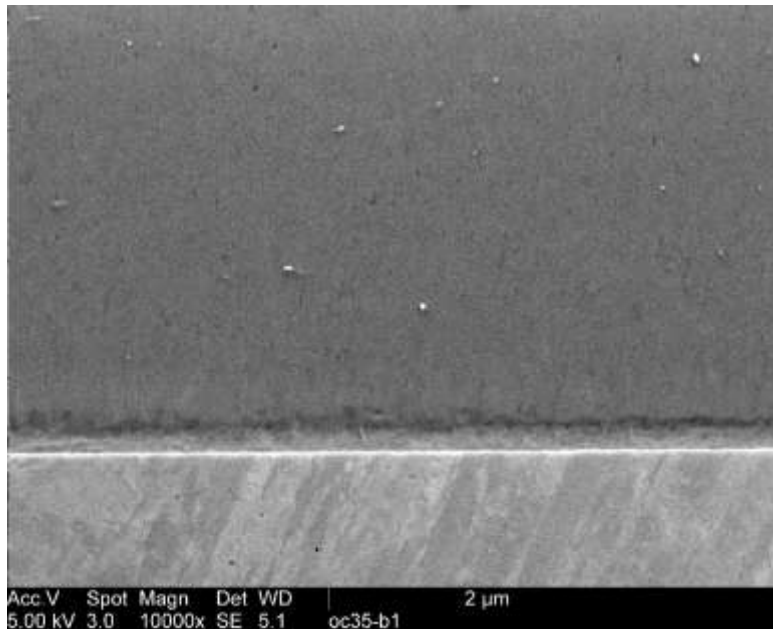


Figure 12, Ti<sub>2</sub>N PVD, cross section SEM image, chemical attack during final chemical mechanical polishing using 0.04micron silica, 10,000x original magnification

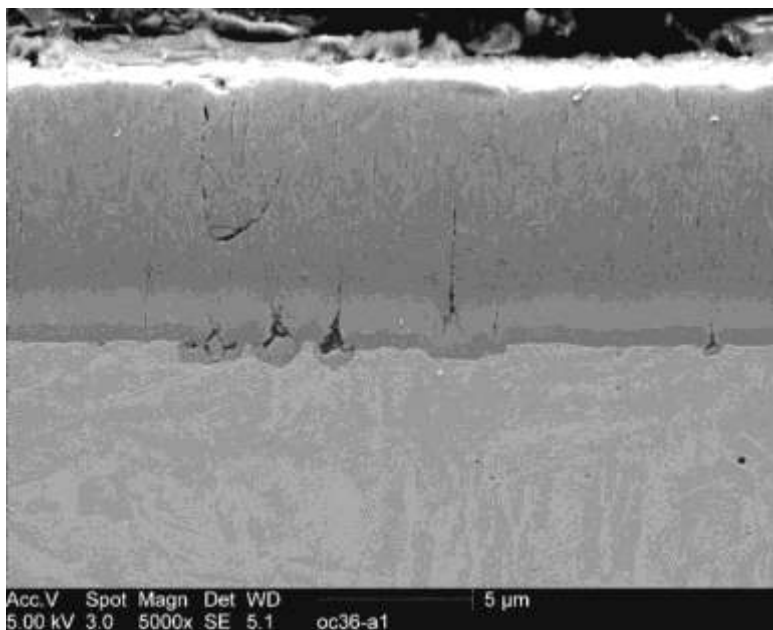


Figure 13, TiN deposit onto chemically milled surface preparation, defects growing from surface irregularities, 5,000x original magnification

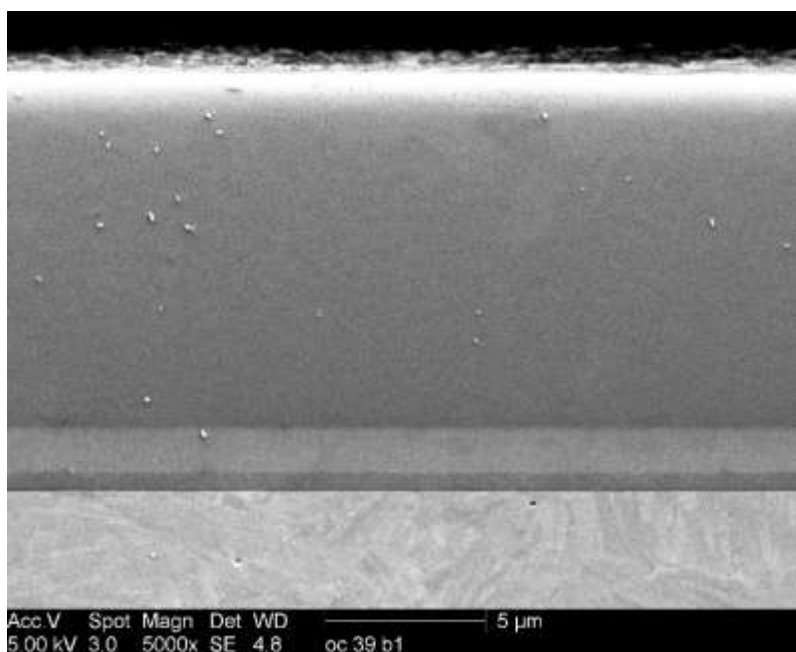


Figure 14a, TiSiCN PVD low nitrogen flow, cross section SEM image, 5,000x original magnification

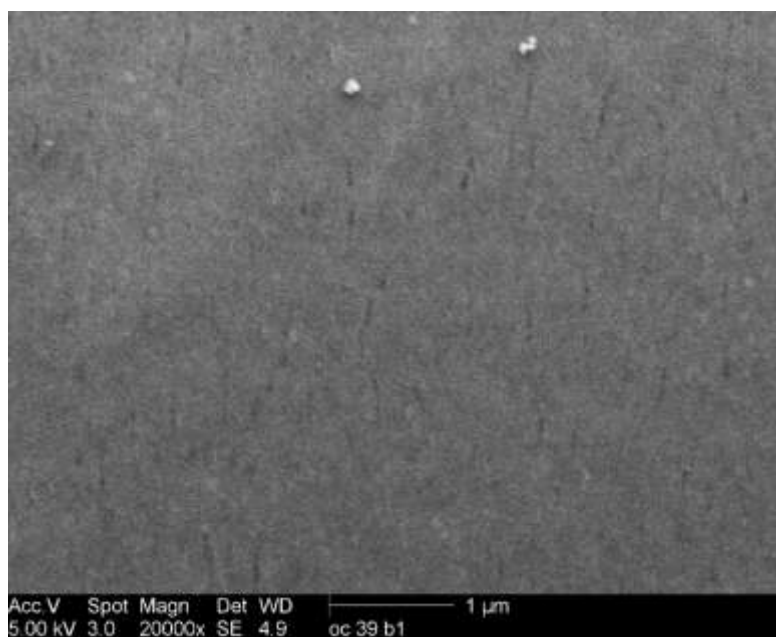


Figure 14b, TiSiCN PVD low nitrogen flow, cross section SEM image 20,000x original magnification

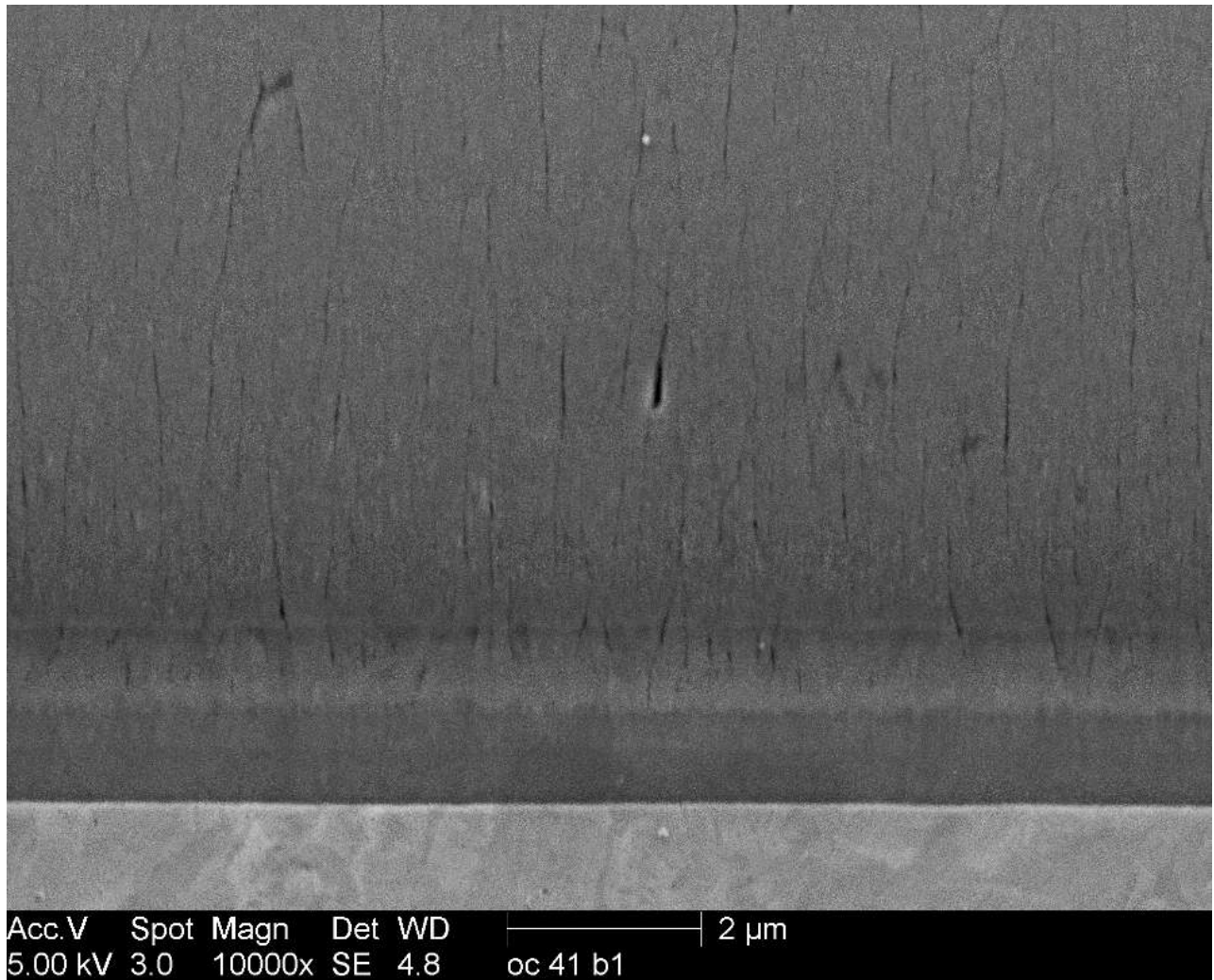


Figure 15, TiSiCN PEMS low nitrogen flow, cross section SEM image, 10,000x original magnification

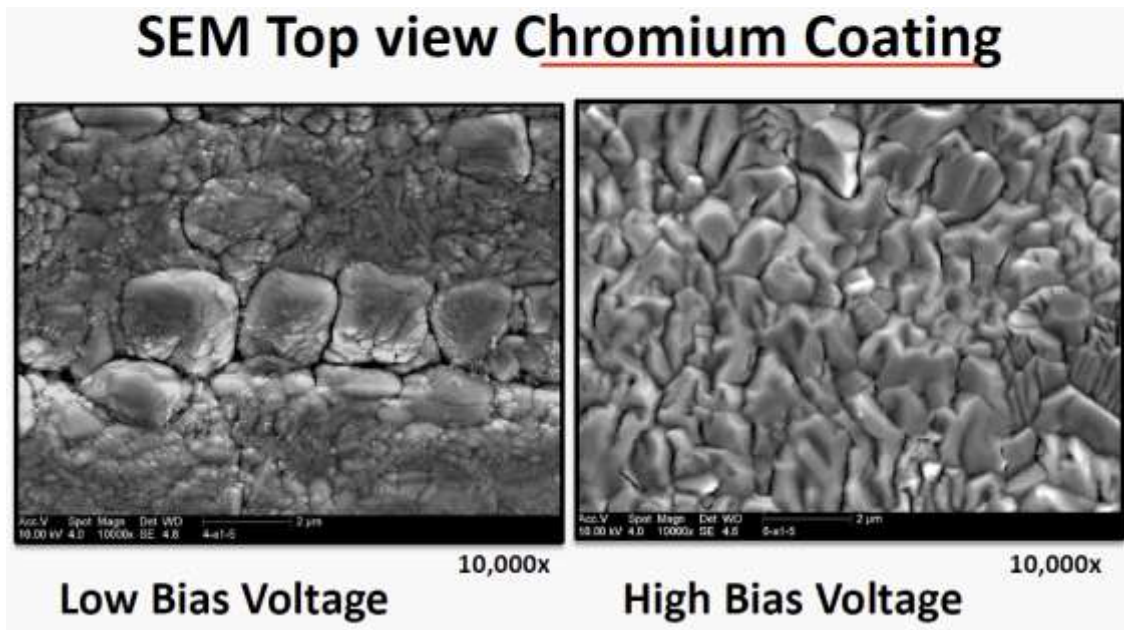


Figure16, Influence of deposition parameters on the columnar morphology of deposits; increased bias voltage results in more uniform higher density coating

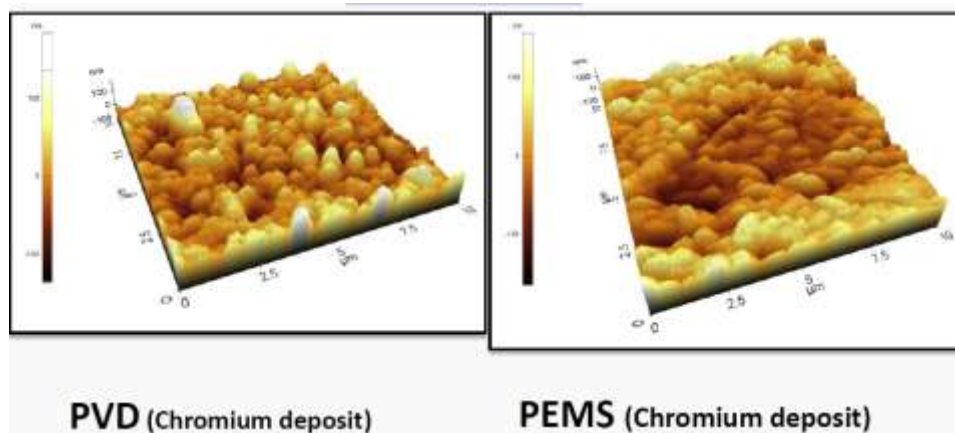


Figure 17, Atomic force microscopy images of CR PVD and POEMS depositions; finer more uniform deposit characteristically results from PEMS process



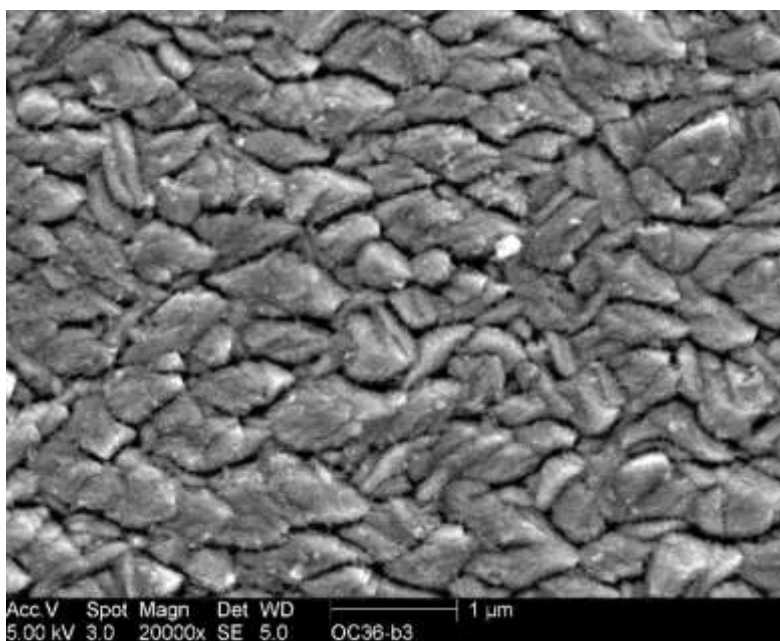


Figure 18, TiN, PEMS top view SEM image, 20,000x original magnification

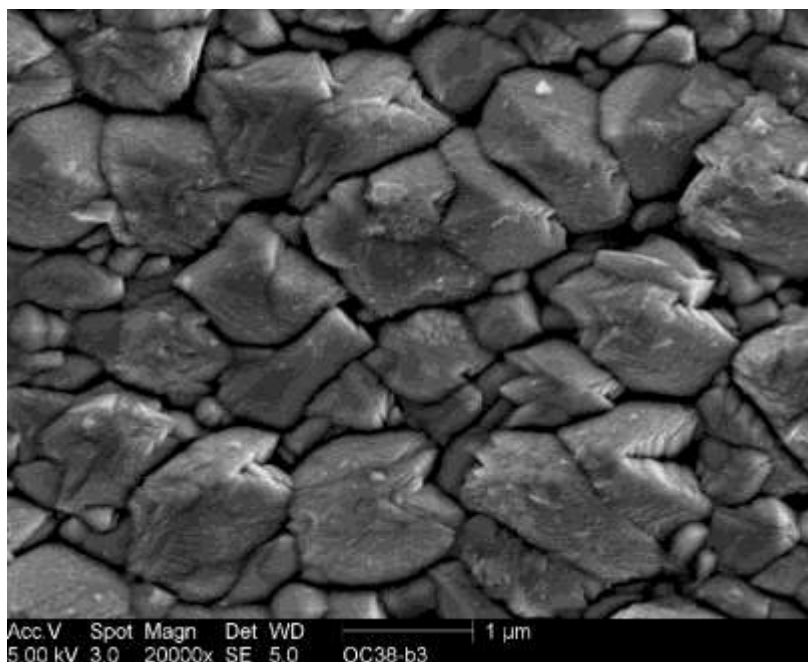


Figure 19, TiN PVD top view SEM image, 20,000x original magnification

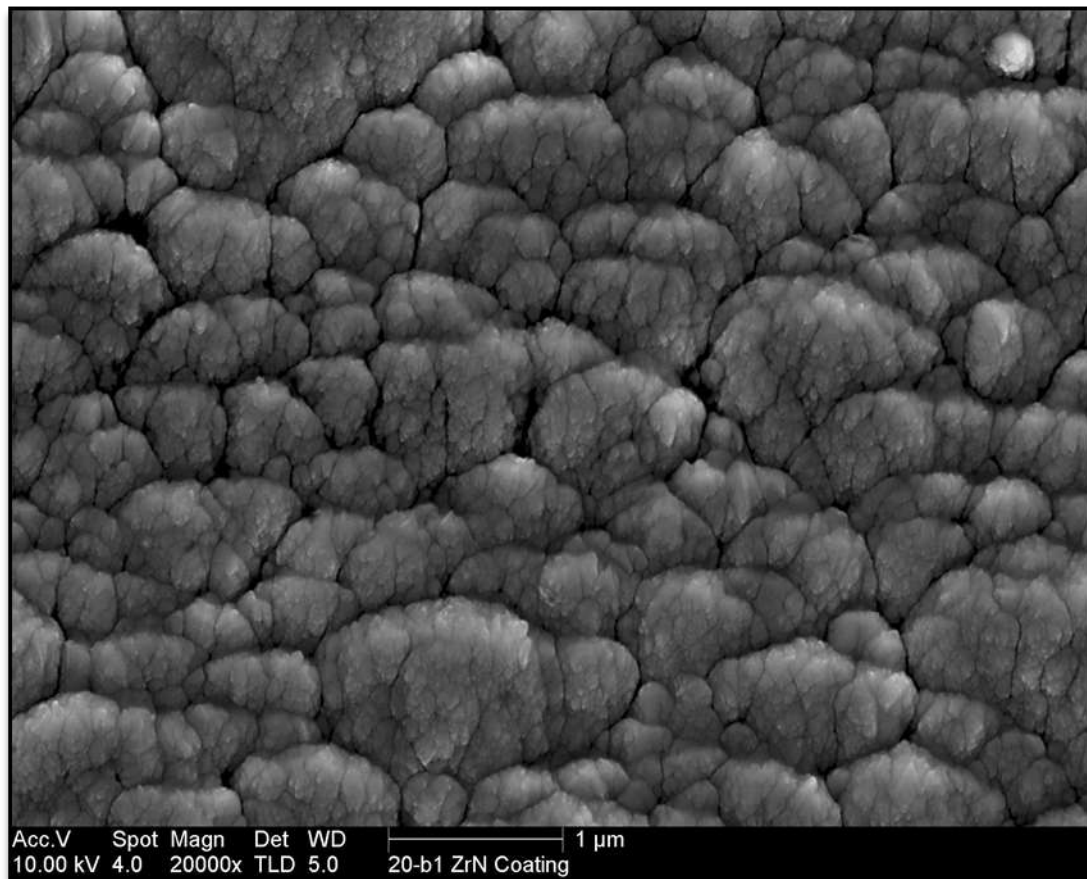


Figure 20, PVD ZrN, 0 bias voltage, 20,000x original magnification



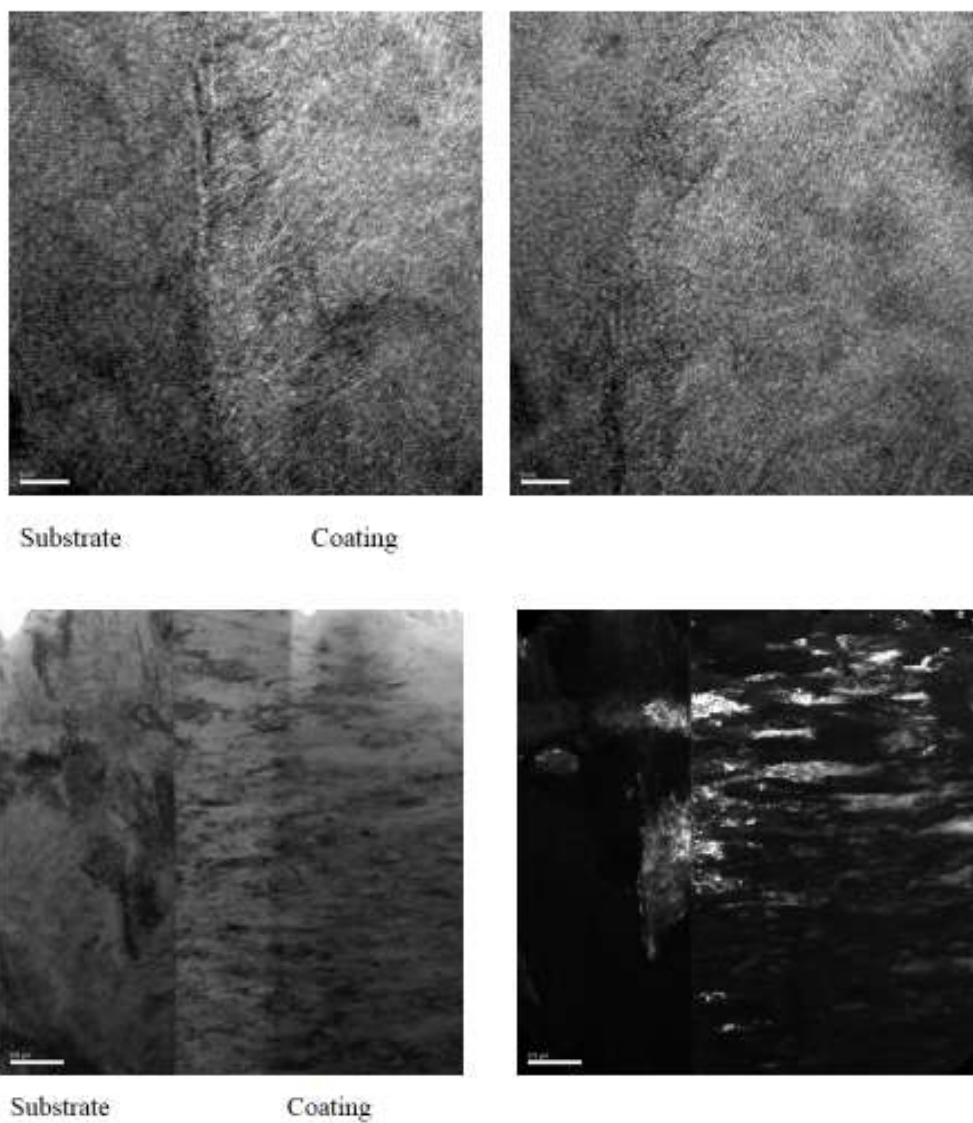


Figure 21, TEM images: (a) bright field, (b)dark field, (c&d) bright field images of TiN COATING at the substrate coating interface

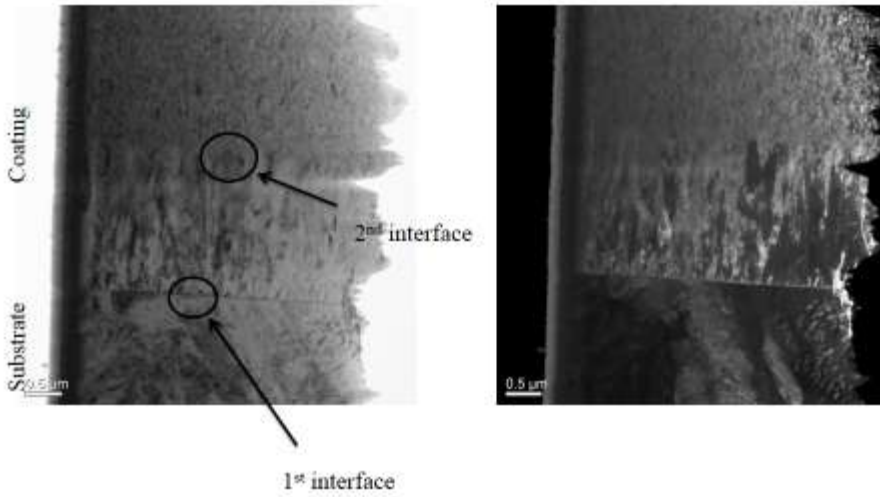


Figure 22, (a) bright field, (b) TEM images: TiSiCN PVD coatings showing two coating transitions

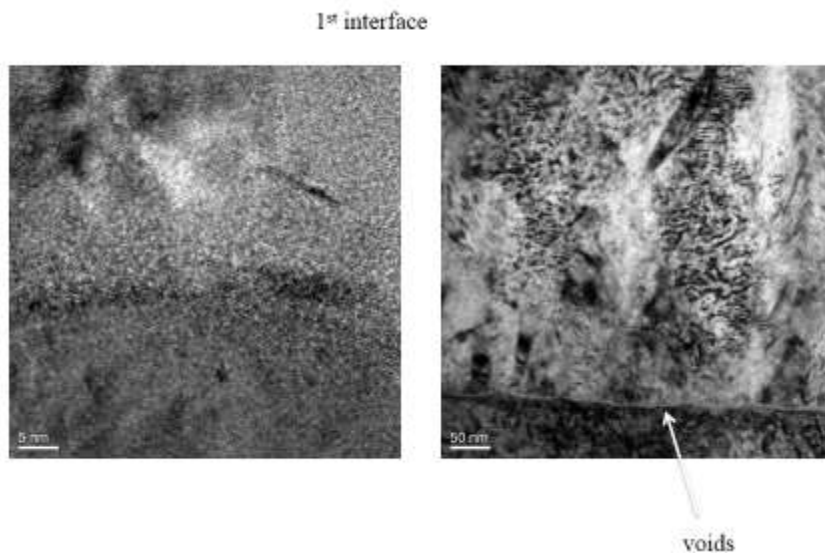


Figure 22 continued, (c & d) first interface transition; void present at substrate- coating interface

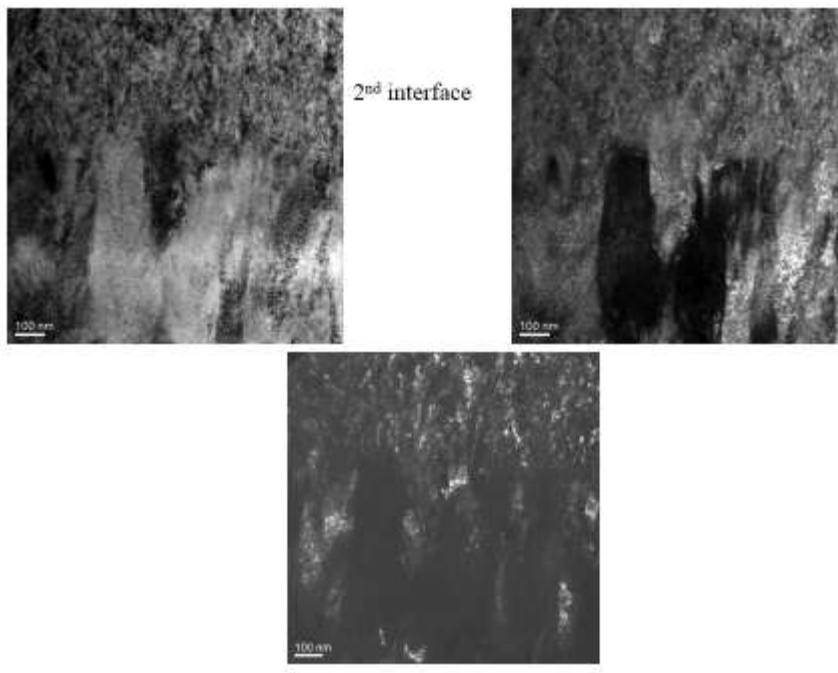


Figure 22 continued, (e & f) bright field image of 2<sup>nd</sup> (g) dark field image of (f) growth direction near the first substrate coating interface



Figure 22 continued, (h) nano voids aligned with transition within the coating

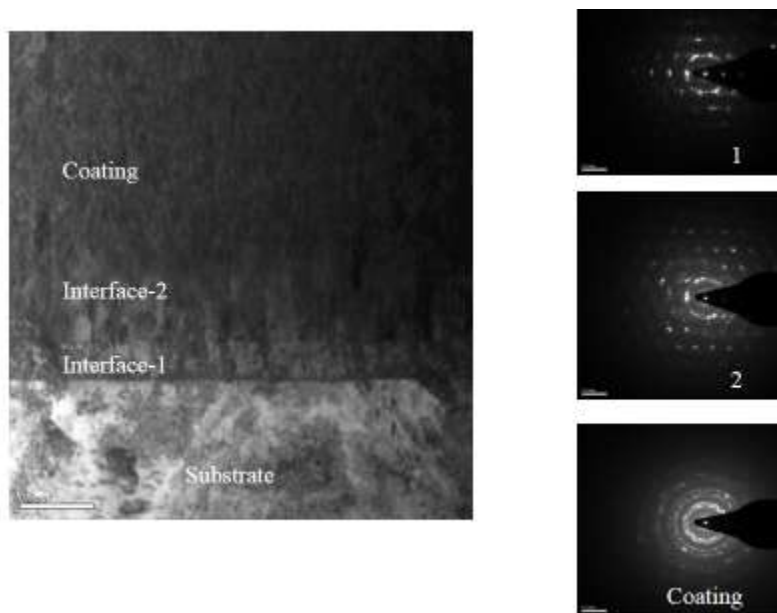


Figure 23, TEM images TiN using PVD (a) bright field image with multiple interfaces, (b-d) SAD images of each region in (a) showing transition from crystalline structure at the substrate Interface to nanocrystalline structure after the 2<sup>nd</sup> coating transition

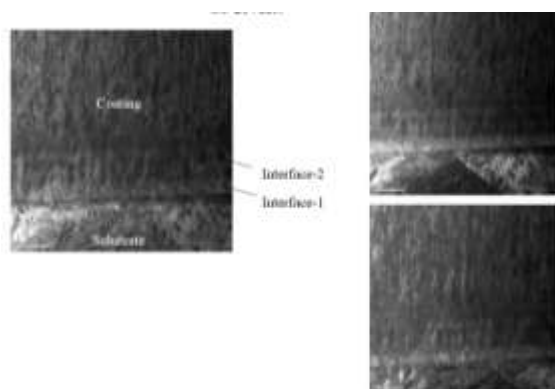


Figure 24, TEM image TiN using PEMS, (a) substrate-coating interface, (b & c) enlarged areas shown in (a)

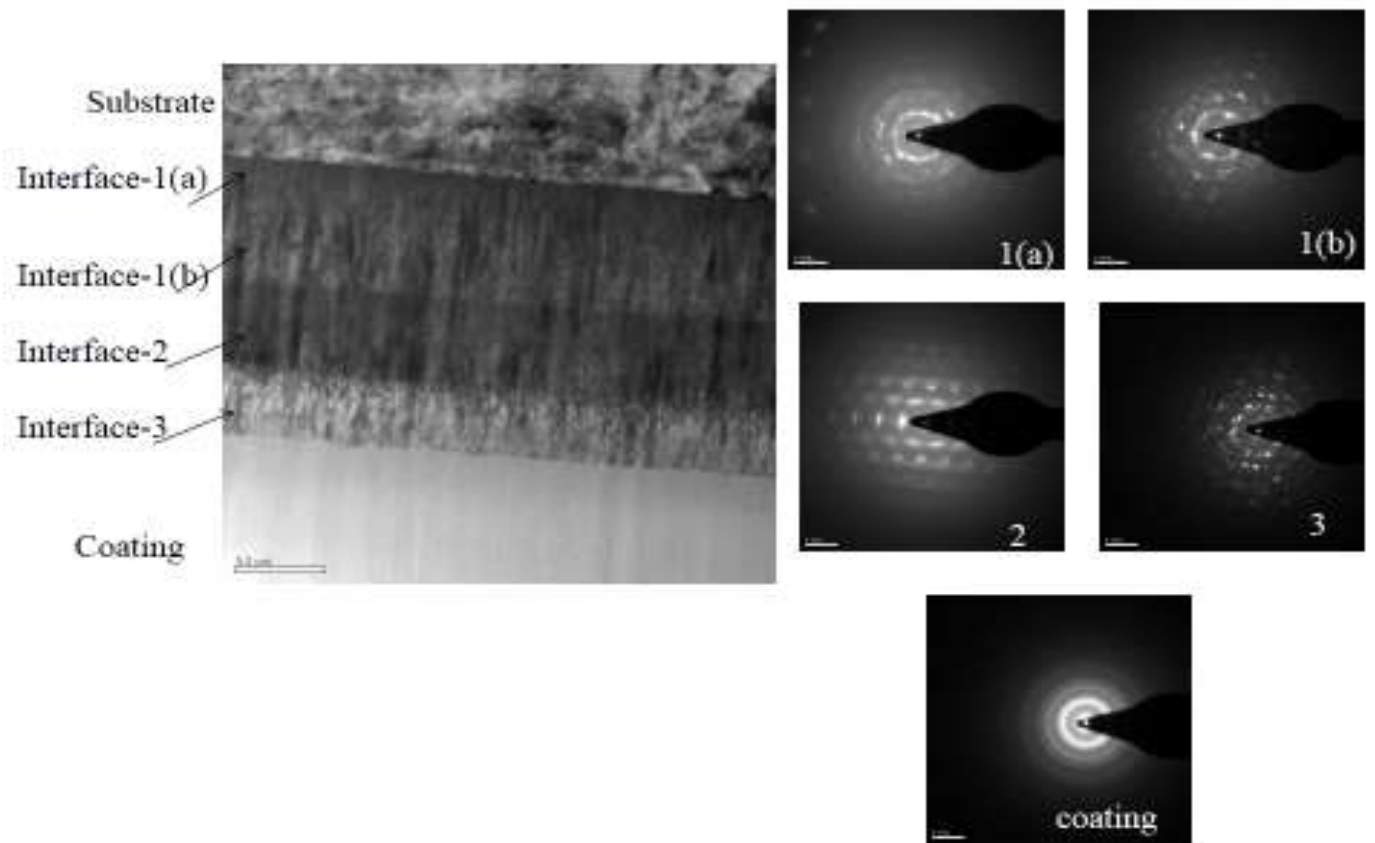


Figure 25, TEM images of ZrSiCN deposited using PEMS, (a) revealing 4 transition interfaces, (b) SAD patterns showing transition from nanocrystalline structure to amorphous coating

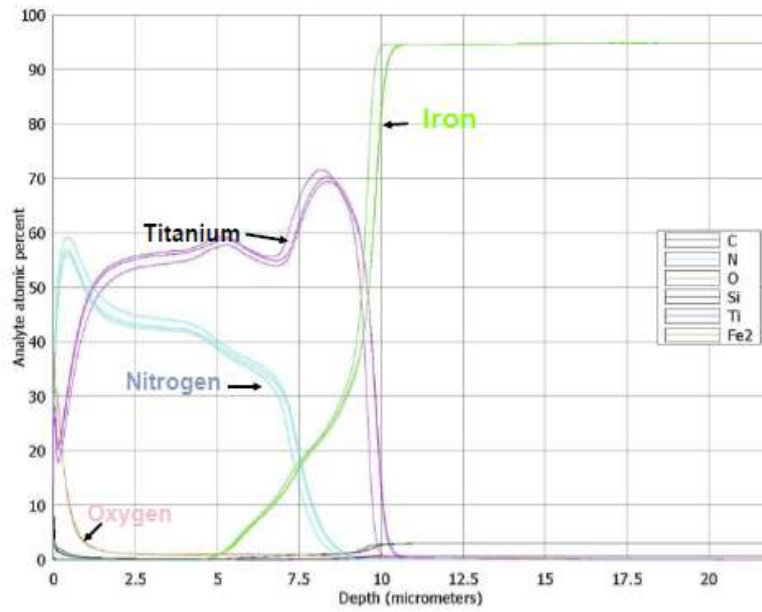


Figure 26, Glow discharge spectrometer depth profile of TiN PVD coating

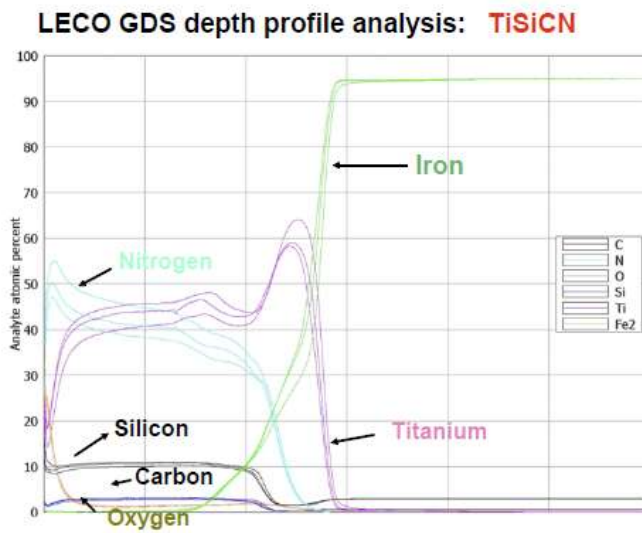


Figure 27, Glow discharge spectrometer depth profile of TiSiCN PEMS coating

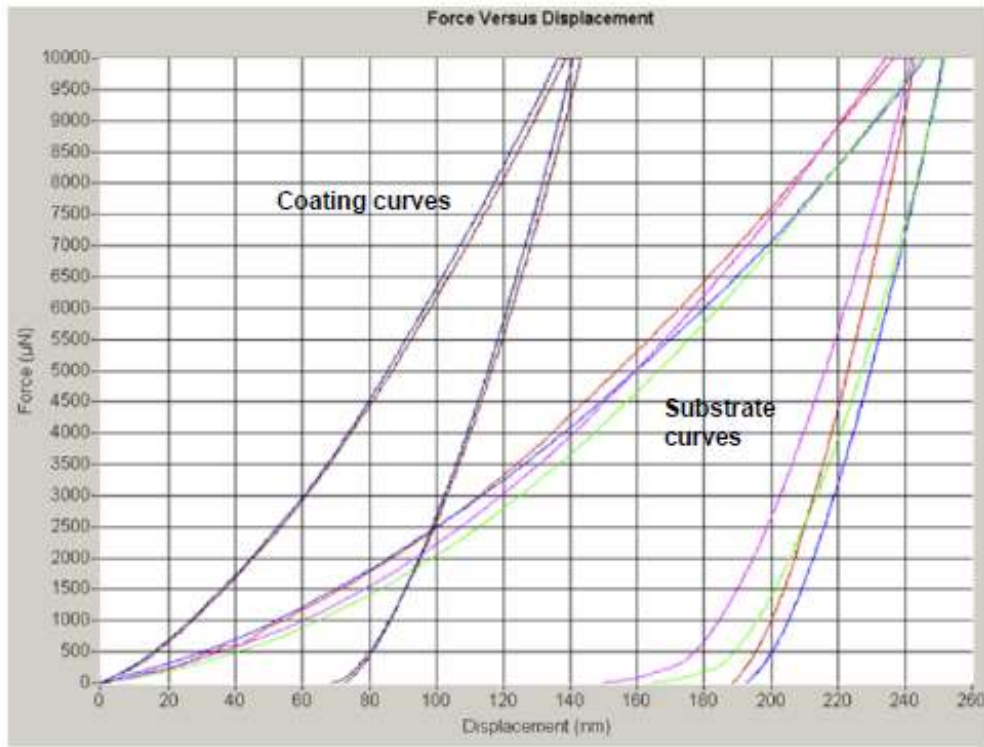


Figure 28, Nano indentation force displacement curve for TiN coating and uncoated HRC 54 Steel substrate



## AE results

> base metal  
> incremental  
loads:  
500-4,000lbs

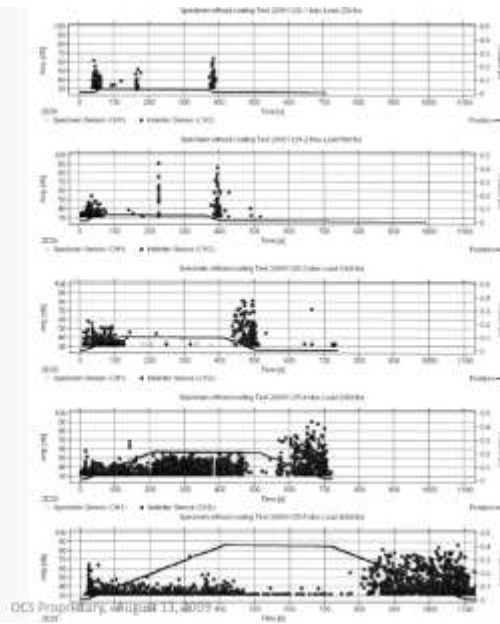


Figure 29, Acoustic emission analysis resulting from incremental load steps; beginning and ending AE are due to loading and unloading rubbing of indenter on test coupon

## AE output Examples

\* EHC [OC44b]  
\* incremental  
loads:  
500-4,000lbs

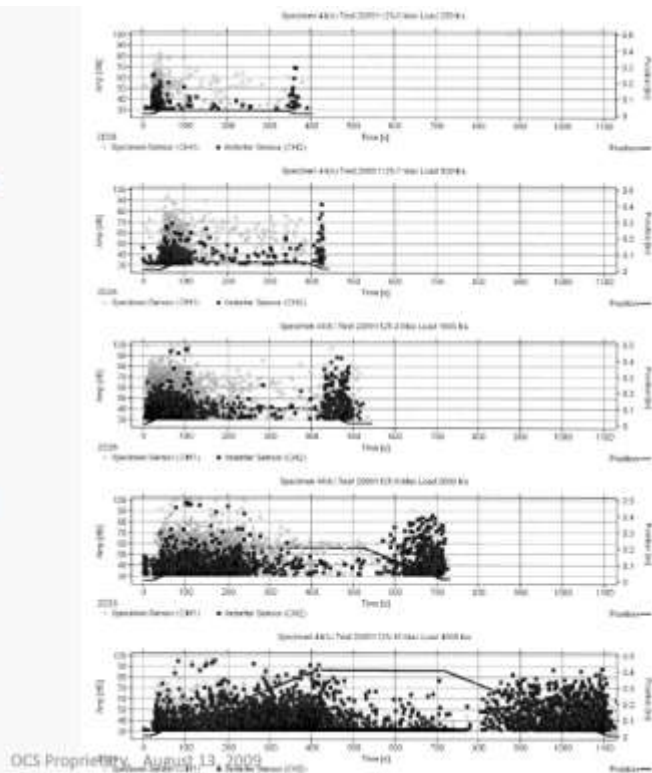


Figure 30, bulge test acoustic emission results for 7 micron thick electrolytic hard chrome for each of 5 applied incremental loads



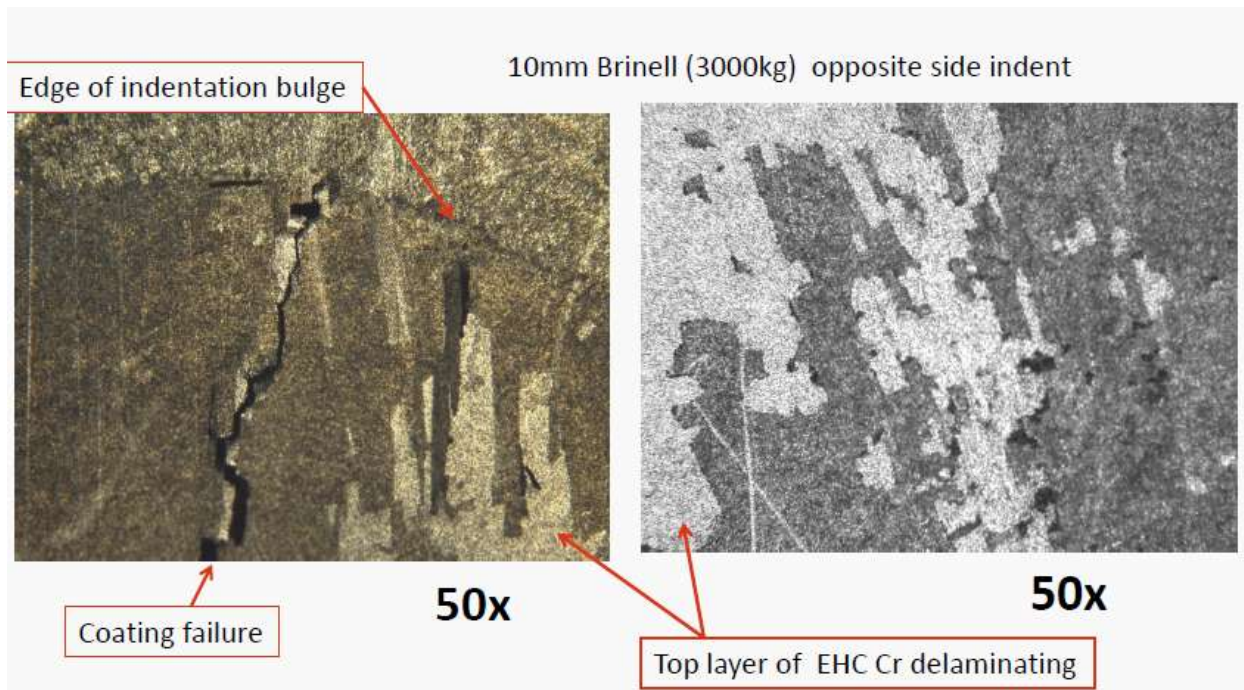
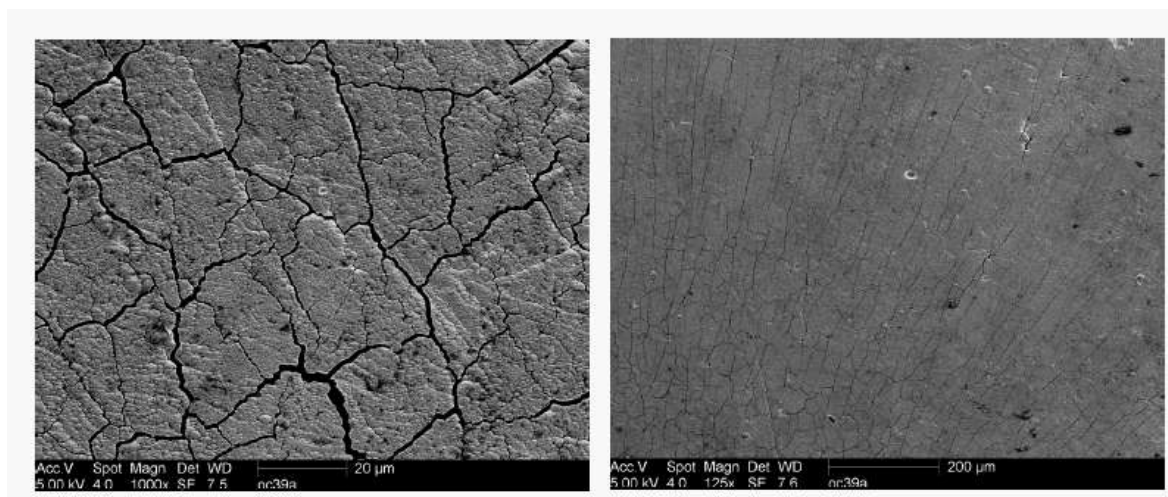


Figure 31, back side bulge deformation strain to failure; 7 micron thick electrolytic hard chrome; 3000kg load using 10mm ball indenter on opposite side



1,000x original magnification

12,500x original magnification

Figure 32, SEM images; sample 39a-PEMS TiSiCN after 3,000kg (6612lb); center of bulge dome with radial and circumferential cracking present

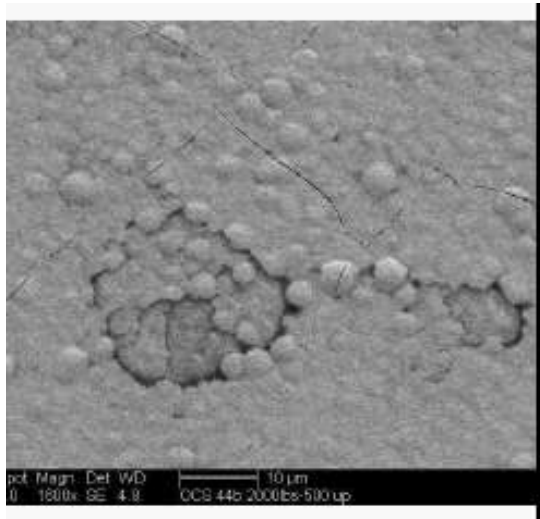


Figure 33, EHC bulge failure, 907kg load; fine cracks present and area of cohesive coating failure

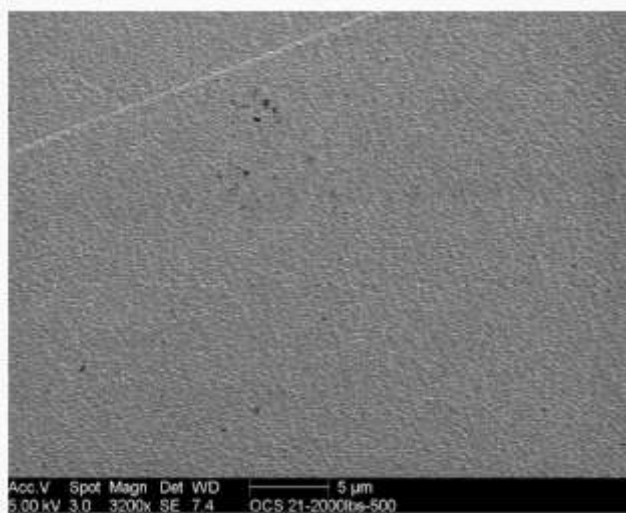


Figure 34, ZrN PVD coating; SEM image of bulge center after 907kg (2000LB) load; no cracking present

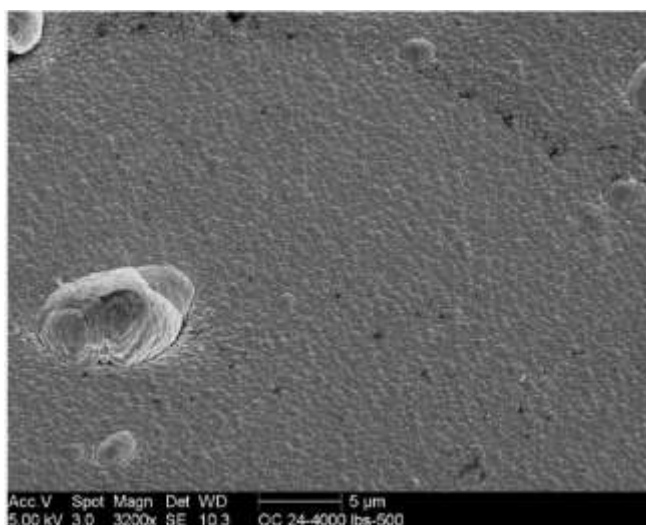


Figure 35, ZrSiCN-PVD coating: SEM image at bulge center after 907kg (2000LB) load; no cracking present

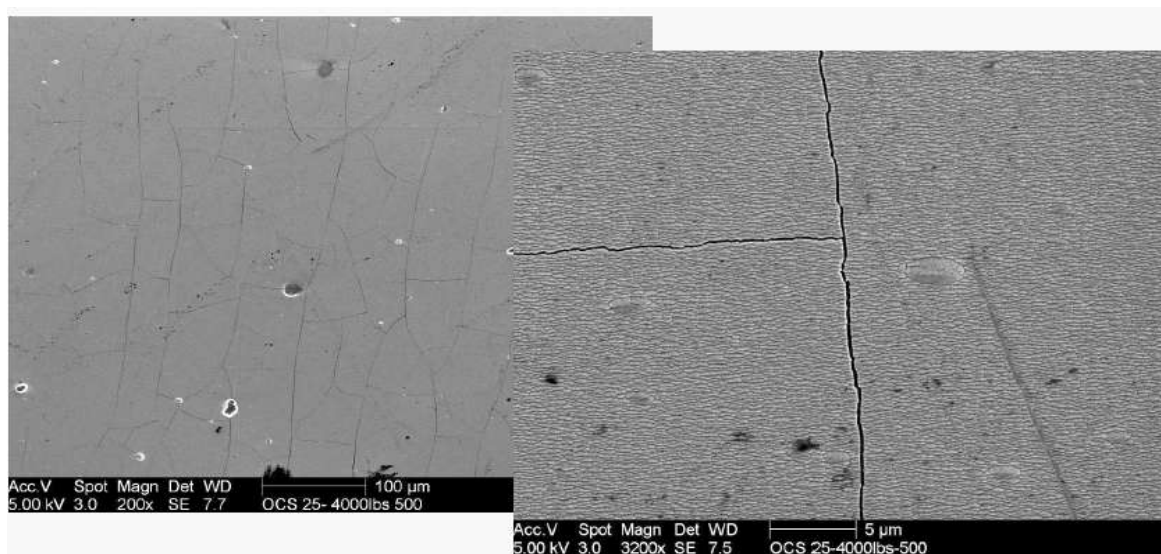


Figure 36, ZrSiCN- PEMS coating; SEM image at bulge center after 1814kg (4000LB) load; radial and circumferential cracking present

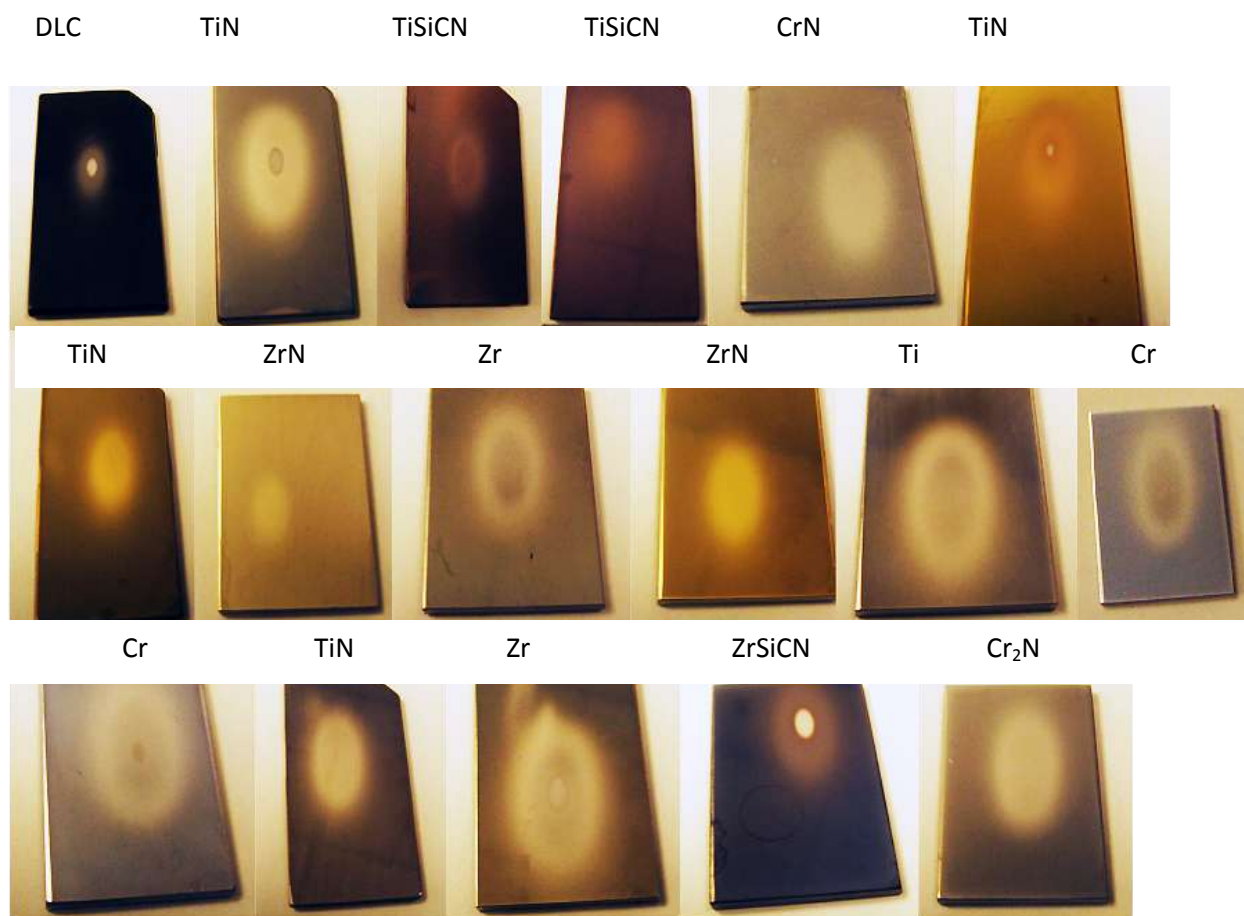


Figure 37, PVD Erosion test sample examples for tests done with a 30degree impingement angle

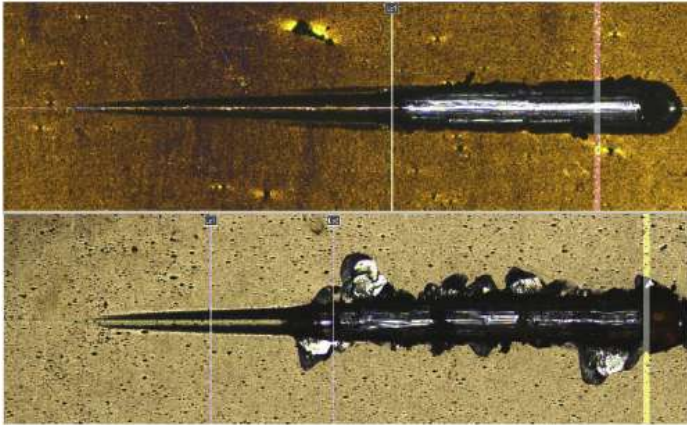


Figure 38, nano scratch adhesion test of TiN (top) and TiSiCN (lower) PEMS coatings, same loading conditions

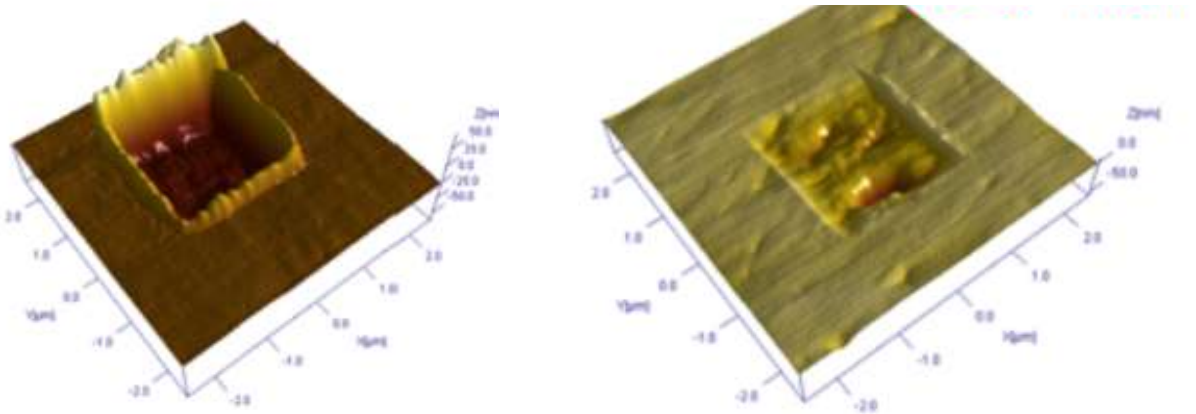
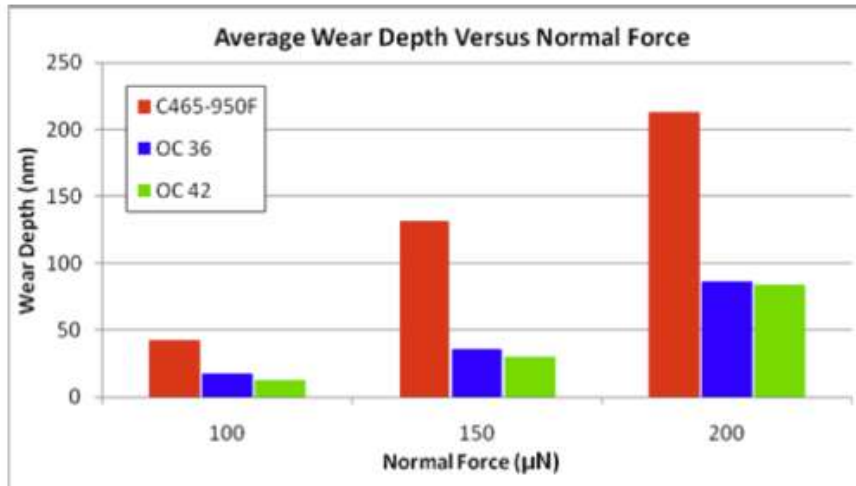


Figure 39, nano scratch wear test of (a) HRC50 C465PH and (b) TiSiCN PEMS coating





| Normal F<br>(microN) | Wear Depth (nm) |        |        |
|----------------------|-----------------|--------|--------|
|                      | C465            | OCS 36 | OCS 42 |
| 100                  | 42              | 17     | 13     |
| 150                  | 131             | 36     | 30     |
| 200                  | 213             | 86     | 84     |

(0.213 microns)

Figure 40, comparative wear depth profiles for Custom 465 PH steel (HRC50), TIN-PVD (OC36 middle column), and TiSiCN PEMS coating (OC42 right column)

Results from nano wear scratch test, figure 39

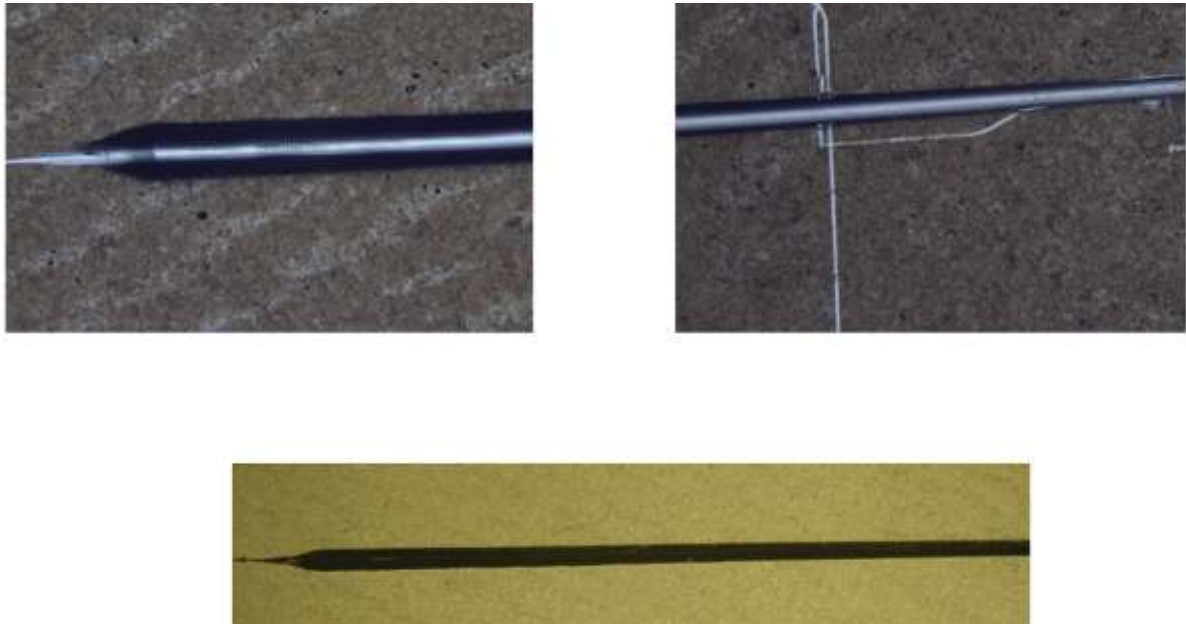


Figure 41, Scratch test PVD Cr deposit, Hv425; bottom image progressive load increase from right to left. Top left scratch end at 100 newton load, no failure, top right, middle section of scratch

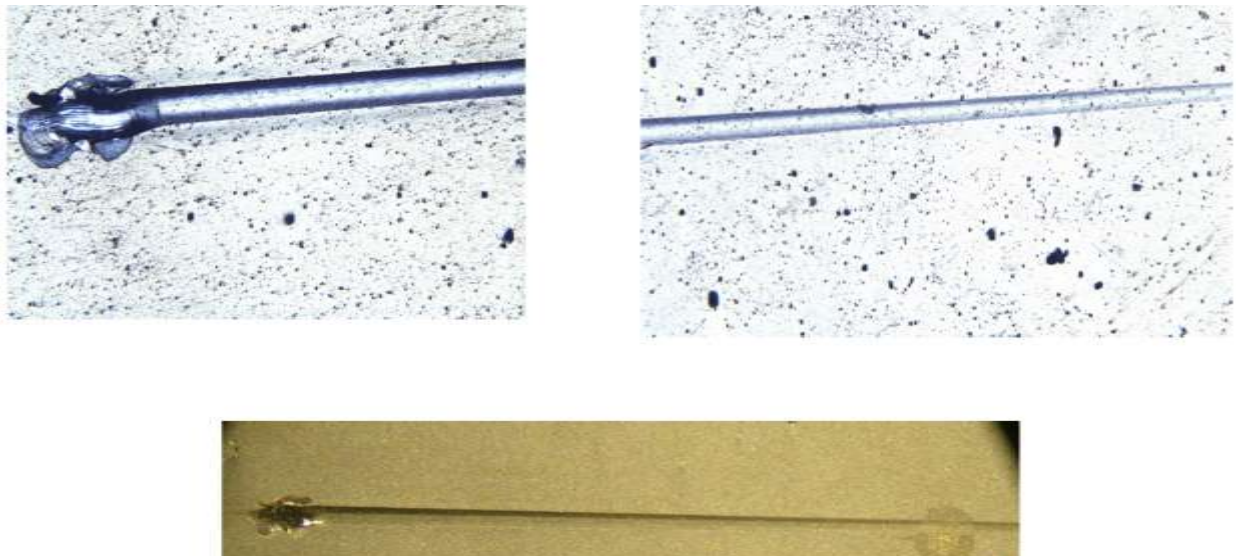


Figure 42, Scratch test PEMS TiSiCN deposit HV3950; bottom image progressive load increase from right to left showing coating failure near end of scratch; top left – enlarged view of bottom left; top right enlarged view of midsection of scratch

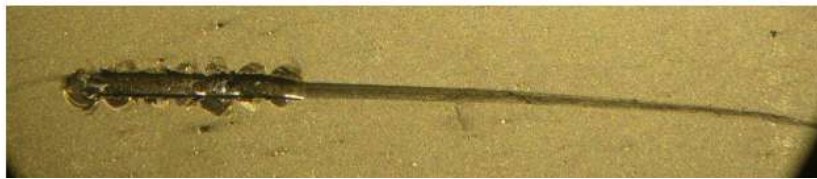
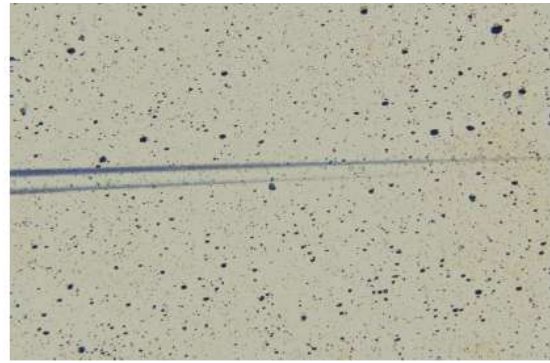


Figure 43, Scratch test; PEMS Zr<sub>2</sub>N deposit with low nitrogen gas flow; Hv 4370; bottom image progressive increasing load from right to left showing coating spalling adhesive failure; top images enlarged view of spalling failure portion and pre-damage scratch zone.

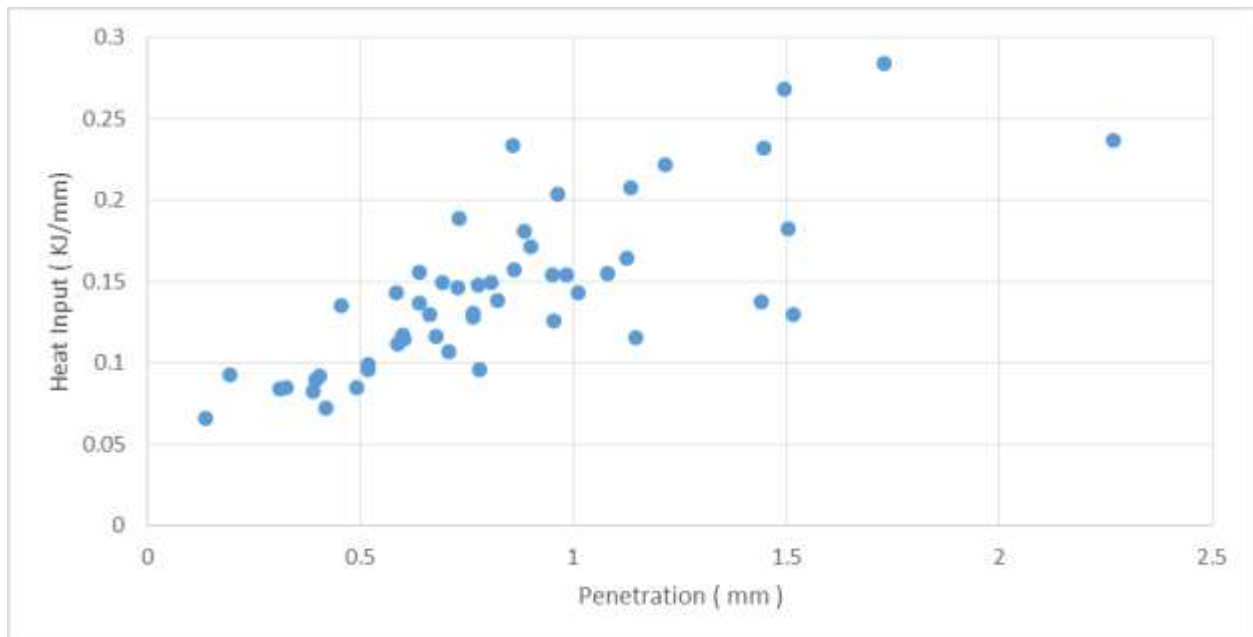


Figure 44, heat input–penetration relationship; data includes all plate thicknesses



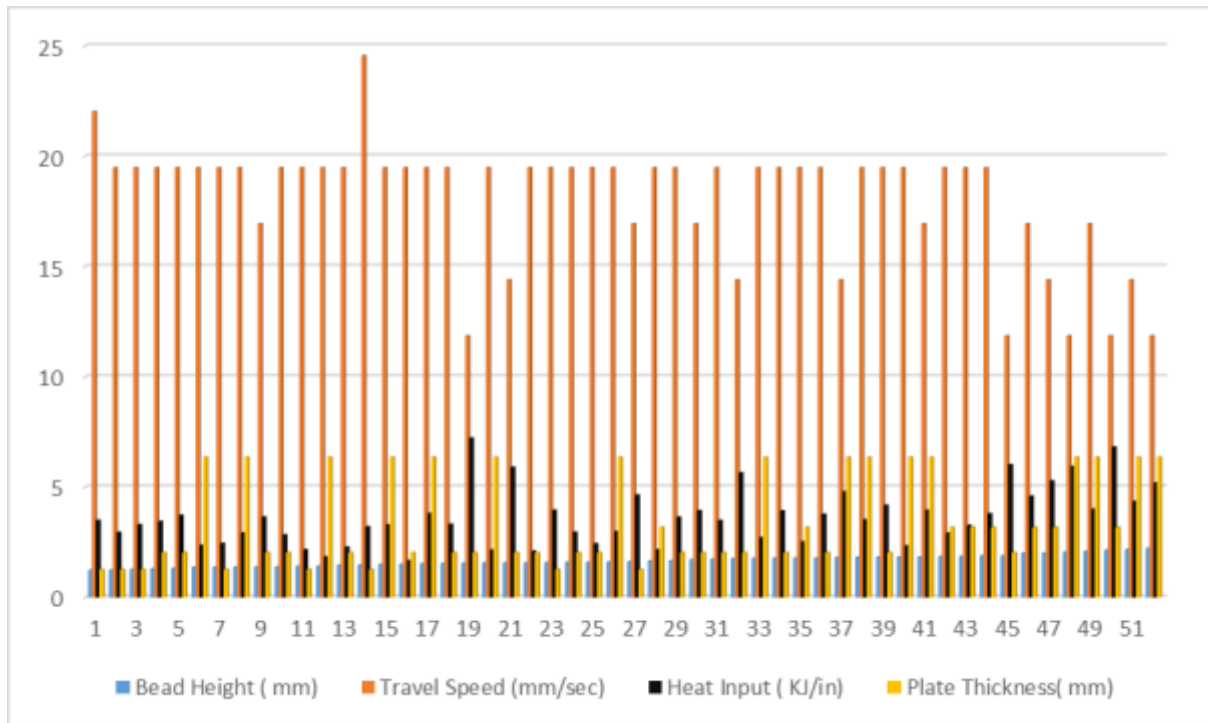


Figure 45, summary CMT weld data showing composite bead height, travel speed, heat input and plate thickness for all weld trials; data is presented in order of increasing height or minimum layer thickness.

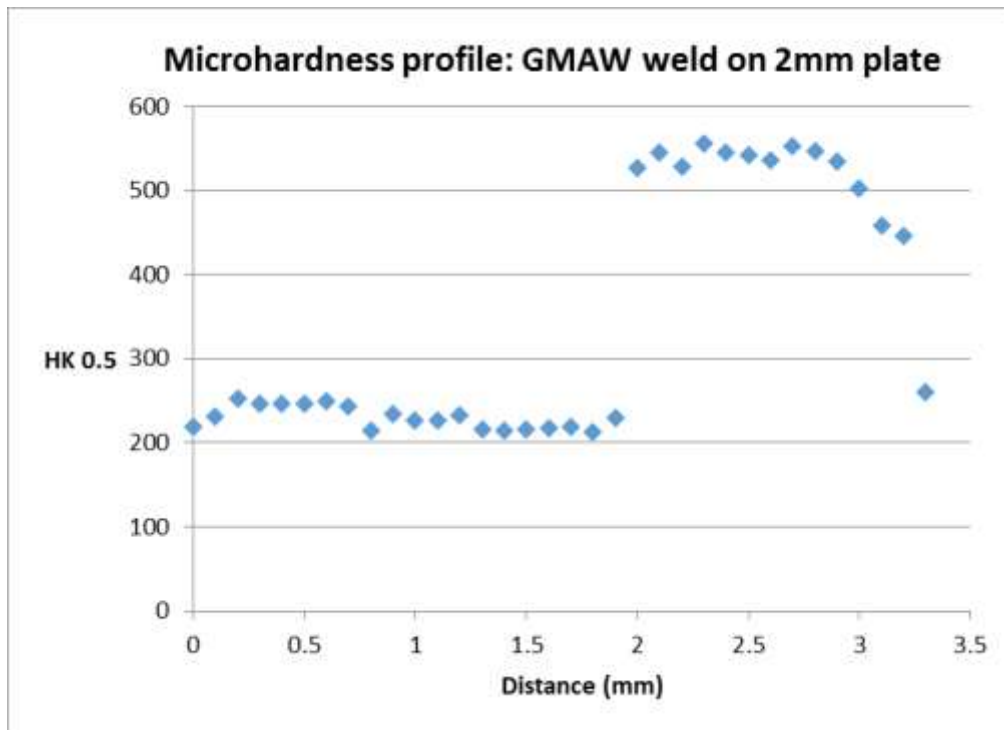


Figure 46, Microhardness profile from top of weld bead through weld and into HAZ. 1-2mm represents 307M weld metal, then HAZ area solution heat treated and quenched due to low H.I. then transition to steel tempering.

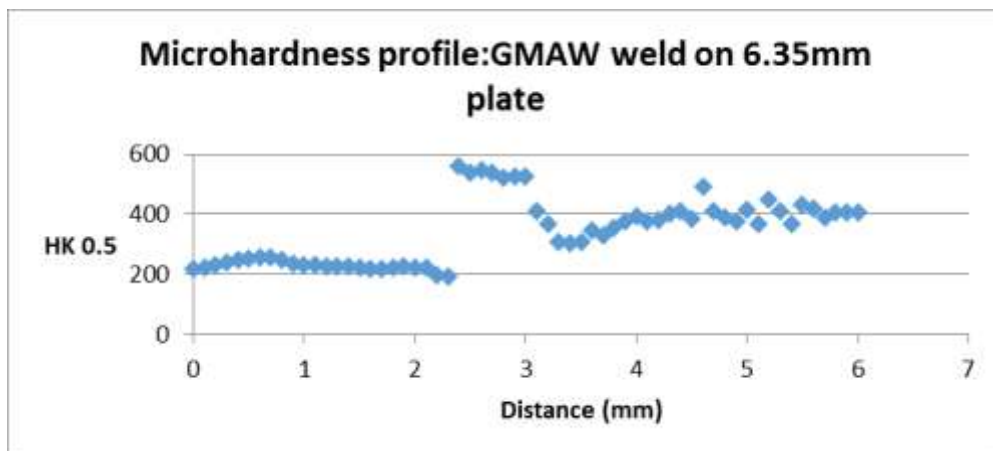


Figure 47, Microhardness profile from top of weld bead through weld and into HAZ. 1-2mm represents 307M weld metal, then HAZ area solution heat treated and quenched due to low H.I. then transition to steel tempering.

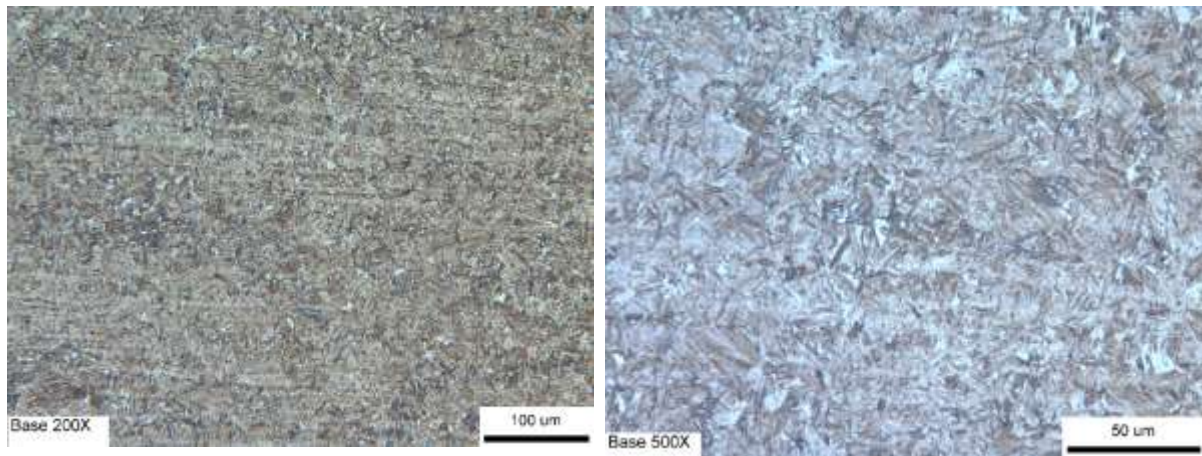


Figure 48, Base metal quench and tempered 4142, martensite tempered at 190°C, HK<sub>500gm</sub> 533 hardness

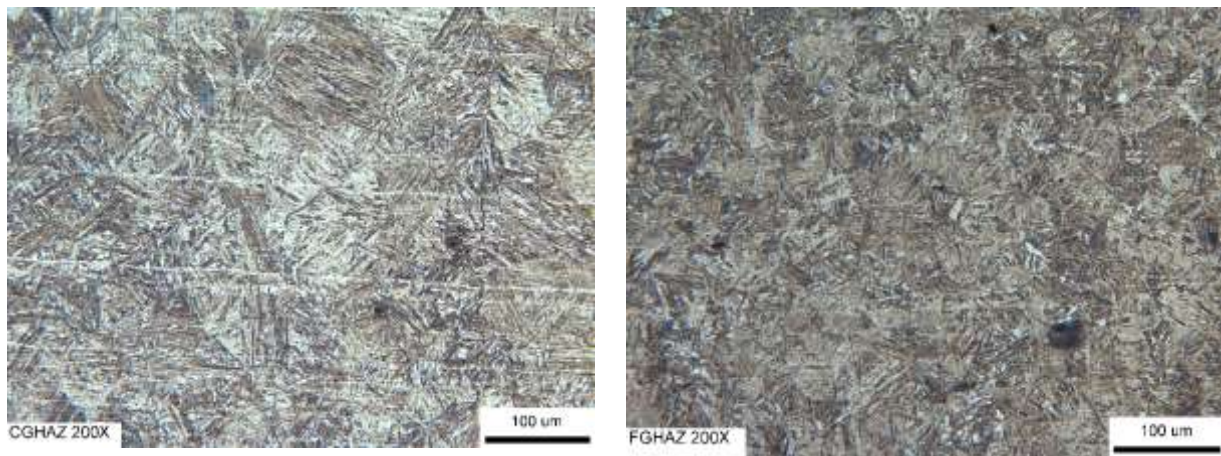


Figure 49, Coarse grain heat affected zone (left hand image) and fine grain heat affected zone (right hand image)

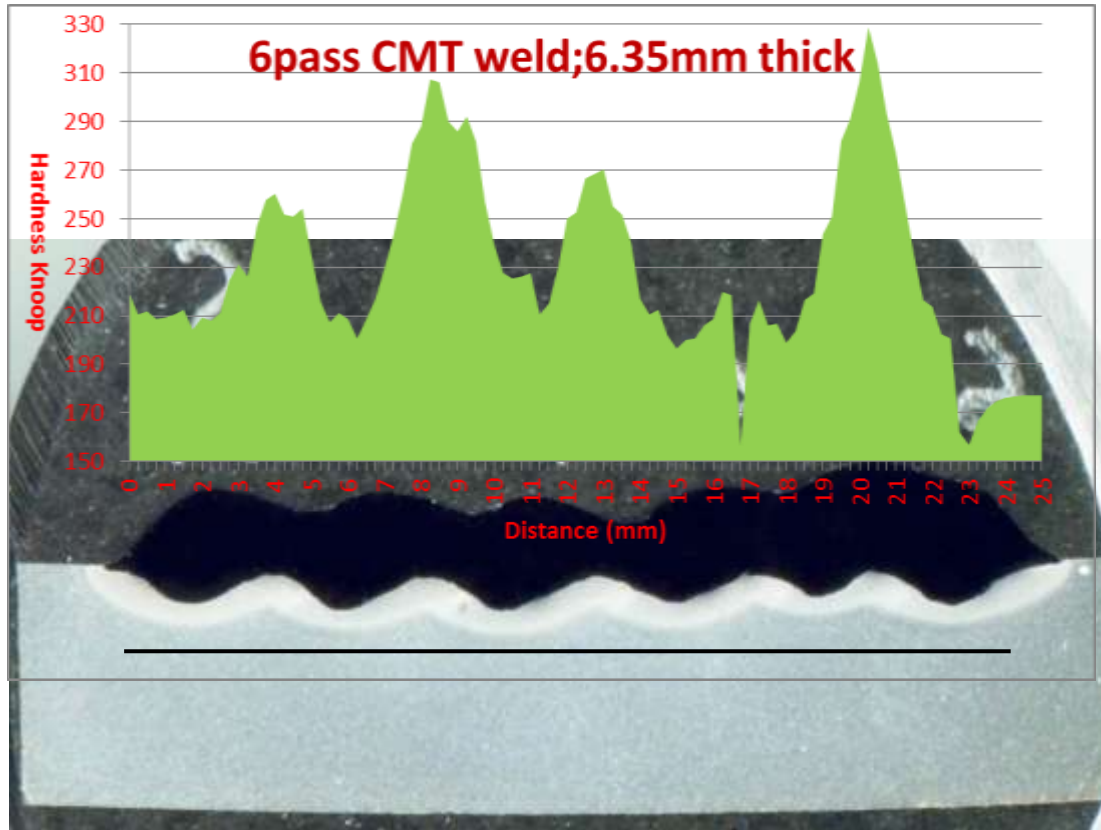


Figure 50, CMT 6 overlay pass weld profile on 6.35mm thick AISI 4142 with Heat affected zone hardness line profile (black line in HAZ marks actual hardness indent line location. Light etching zone immediately under weld metal is the martensite transformation band.

## **Appendix C – Washington State University Final Report**

**WSU proposed research:** Targeted areas: Production and structural integrity improvement of fiber reinforced plastic (FRP) composite materials for defense systems components.

## **WSU-TASK 1: DEFECT-FREE HOLE PRODUCTION ON FRP MATERIALS.**

### **1 INTRODUCTION**

Composite materials are used in a variety of applications. The aerospace, maritime and automotive industries increasingly rely on these materials for structural and aesthetic (compartmental) applications. One of the most common composite materials for aerospace applications is carbon fiber reinforced plastics (CFRP). CFRP is used for a variety of applications because of its high strength to weight ratio and stiffness. The material properties and shape of a CFRP material can be tailored for a specific application. This makes them popular materials with designers and engineers, however the manufacturing and machining of these materials can be challenging. The high strength and abrasive nature of the material cause excessive tool wear and often result in poor work piece quality [1]. In machining of CFRP perhaps the most common operation is drilling holes. In the construction of only one wing of a large aircraft may involve drilling in the vicinity of 45,000 holes. Because of the CFRP's abrasive nature, tool life is significantly reduced [2-3]. The resulting holes often have delamination damage around the entry and exit and uncut fibers or other defects that may require post processing.

Industry is acutely aware of these issues and several studies were performed as a result. These studies have investigated the relationships between machining parameters such as feed, speed and coolant to the resulting drilling forces, tool wear and hole quality[4-9]. Tsao [7] found that with an increase in cutting speed thrust force decreased, thus resulting in less tool wear. The disadvantage to increasing cutting speed is that this increases the delamination damage factor [8]. It is also found that lowering the feed rate decreased delamination but greatly extended machining time. The fundamental characteristics behind CFRP drilling have already been well established through these studies. With so many types and materials for the drills available, many of these investigations are rather limited. Many of these studies are conducted with HSS or carbide drills, and only few examined some coated drills among a large variety of coated drills available in the market.

The coatings are expected to increase the tool life have a potential to improve cutting conditions and improve hole quality [9-12]. Brinksmeier and Janssen found that the quality of holes improved with the use of tool coatings of  $TiB_2$  or diamond [10]. Zitoun et al. found that in drilling of CFRP with a nanocomposite CrAlN coated tools had 30% improvement in surface roughness [11]. Shyha et al conducted a study in drilling CFRP and metallic stacks with coated tools; uncoated, C7 coated (nano-crystalline AlTiN grains embedded in  $Si_3N_4$  matrix), and CVD diamond. They found that C7 coated drills produced less hole roundness errors in CFRP over other drills and CVD diamond coated drills produced the lowest surface roughness [12]. Many of these studies focus on diamond coated drills and more studies on other coatings are desperately needed to see if a more cost-effective coating is available. This study attempts to investigate the effect that coated tools have in changing hole quality.

## 2. EXPERIMENTAL METHODS

### 2.1 Materials

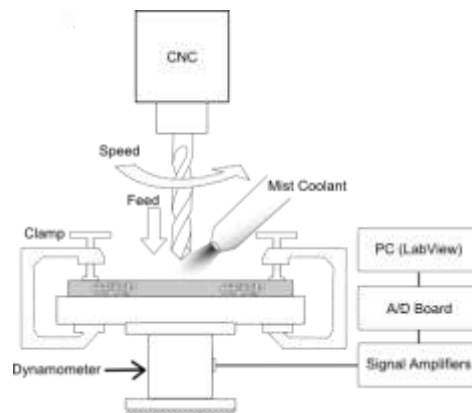
The Boeing Co. provided the CFRP plates made of multidirectional quasi-isotropic composite of Toray carbon fibers in an epoxy matrix. The CFRP had a plate thickness of 7.54 mm with an average ply thickness of 0.1885 mm.

### 2.2 Tools

Four types of drills were used in the drilling tests; uncoated, diamond coated, AlTiN coated and nanocomposite coated carbides. The diamond coating was applied through a chemical vapor deposition (CVD) process and had a thickness of 12.5  $\mu\text{m}$ . The AlTiN and nanocomposite coatings each had a thickness of 3  $\mu\text{m}$ . The nanocomposite coating has a matrix structure comprised of  $\text{Si}_3\text{N}_4$  and AlTiN. Both the AlTiN and nanocomposite coatings were applied by Unimerco, Inc. (Saline, MI, USA). The base drill material before coating was a micrograin carbide. The base drill had a 3/8" cutting diameter with a 3/8" shank diameter. The overall length of the drills was 3-1/2" and the flute length was 1-1/2". The drills have two flutes with a helix angle of 25 degrees in a right hand spiral, right hand cut (RHS/RHC). The point angle of the drill was 135 degree with a faceted split point per NAS907 P-3.

### 2.3 Drilling Experiments

The drilling operation was conducted using a 3-axis CNC vertical mill (MiniMill, HAAS, USA). The CFRP laminates were clamped to a fixture that mounted to a dynamometer (TRS-1K-OPT-THR, Transducer Techniques, USA). The fixture was a 1/4" thick aluminum plate with 1/2" clearance holes to allow for a through hole in the CFRP laminate plates. The CFRP laminates were clamped directly to the fixture so that the forces generated during drilling are accurately measured by the dynamometer. The signals from the dynamometer were transmitted to signal amplifiers, then to an A/D board (NI USB-6251, National Instruments (NI), USA) and recorded on a personal computer (PC) using the data acquisition software (LabView 7.1, NI, USA). The experimental step is shown in schematic form in Fig. 1.



**Figure 1.** Schematics of drilling set up and drilling force acquisition.

The same drilling conditions were used for all the drills; the speed was 6000 RPM and the feed rate was 0.0762 mm/rev. A water soluble cutting fluid coolant is used in the experiment, applied as a

mist with a constant flow rate of 16mL/min. The drilling experiments were conducted until each drill produced 120 holes or failed. The AlTiN coated drill failed early not from wear but due to a machine error.

## **2.4 Wear evolution analysis**

A Scanning Electron Microscope (SEM) provided the high magnification pictures of the wear patterns. SEM images in Figure 5 show the progression of coating and tool wear.

## **2.5 Hole Quality Assessment**

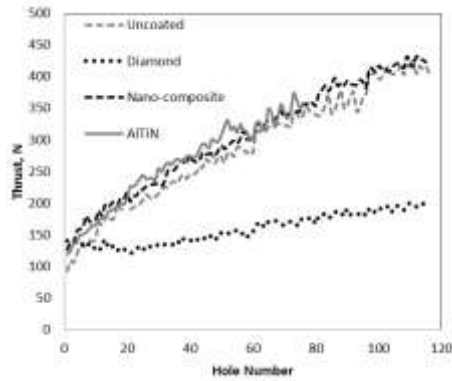
The hole quality was measured through various methods and with various machines. The diameter and roundness of the hole was measured using a Brown & Sharpe gage 2000 Coordinate Measuring Machine (CMM). The hole diameter and roundness was measured at the midpoint of the plate. This was at a depth of 12.7 mm from the surface of the CFRP. The diameter and roundness were measured with 8 data points per hole. The hole surface roughness was measured with a Time T200 roughness tester. The cutoff length for each test was 8 mm and the tester had a number of cut offs as 5 and an RC filter for data filtering. For each hole, two data points of roughness were collected. The roughness was measured axially near the midpoint of the plate. Lastly the delamination was observed using a Nixon DXM 1200 optical microscope. The length of the delamination was measured using a Quadra-chek 200 measurement system attached to the microscope.

# **3. EXPERIMENT RESULTS**

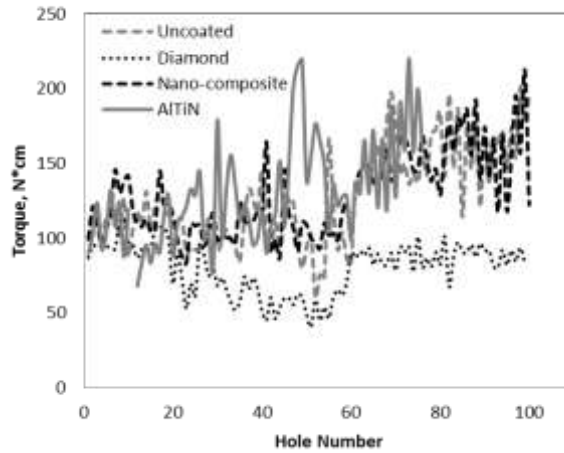
## **3.1 Drilling forces, torques and tool wear**

The maximum drilling thrust force and torque measured are shown in Figure 2. An increase in correlates with an increase in thrust force. There is a correlation for all coated tools with drilling thrust force and tool wear. The diamond coated drill showed the best performance of all the tools, with the lowest maximum thrust while uncoated, diamond and nanocomposite coated tools performed similarly and had higher thrust forces. For the drills other than diamond coated tool, maximum torque values are also increasing with increasing hole number. However, they do not seem to be as sensitive to tool wear as thrust values. Diamond coated drill provide relatively consistent maximum torque over the holes.





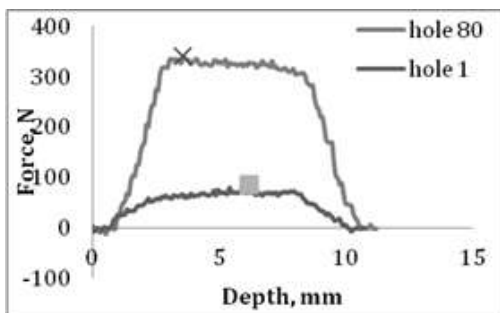
(a) Maximum Thrust Force



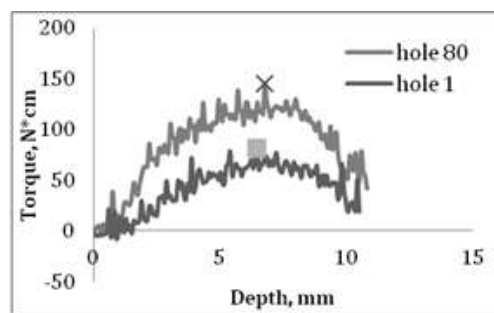
(b) Maximum Torque

**Figure 2.** Changes in Drilling Forces and Torques as a function of Hole Number for Various Tool Coatings

The depth of the drill into the hole and drilled hole number affected the magnitude of the cutting thrust force and torque. All the coatings exhibited a similar force profile with varying magnitudes as shown in Figure 4. There are three distinct phases for the thrust force. The first phase is the sharp increase in thrust force as the chisel edge engages with the top ply of the laminate. Possible problems for this stage are skidding, wandering or deflection of the drill bit which can affect the hole quality. The next phase is a constant phase as the cutting lips are fully engaged with the workpiece. The maximum thrust and torque generally occur during this phase. In the decreasing phase the thrust force lowers as the chisel and cutting edges break through the back of the laminate. Note that while the thrust returns to zero after cutting the torque does not. This residual torque is due to uncut fibers and to the plastic return of the material after drilling.

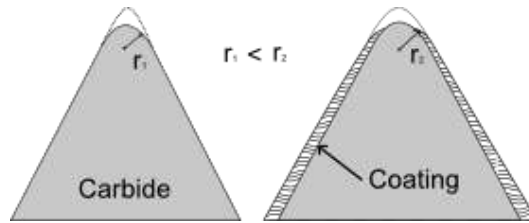


(a) Recorded Thrust Force for Uncoated Drill

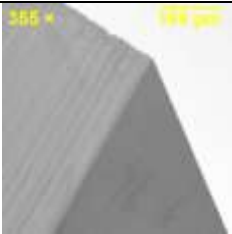
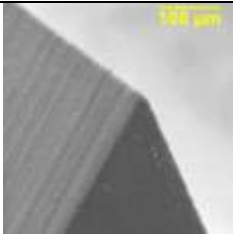

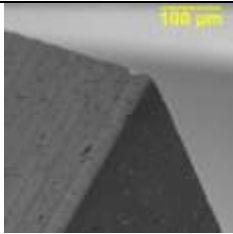
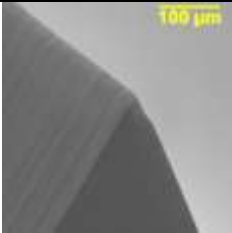
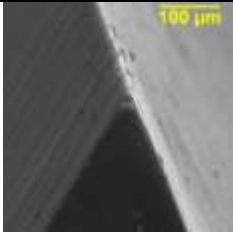
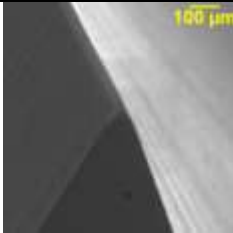
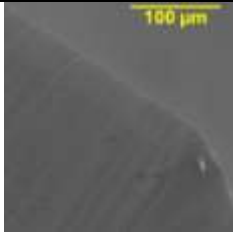
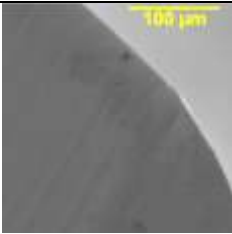
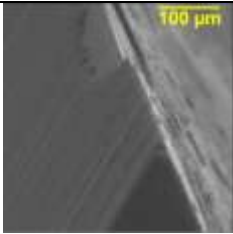
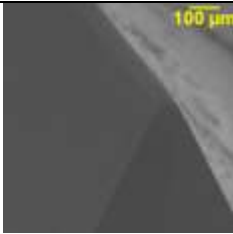
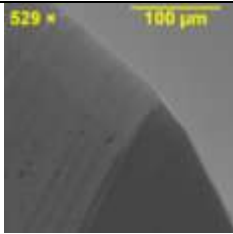
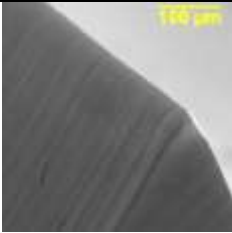

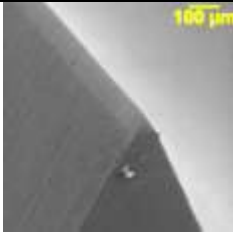
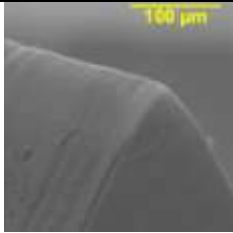

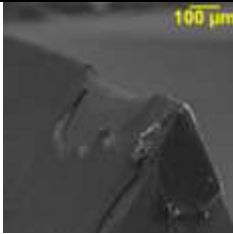
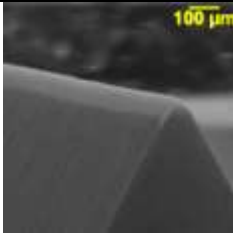
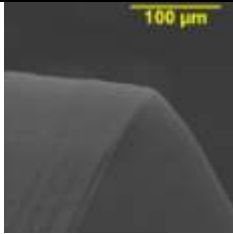


(b) Recorded Torque for Uncoated Drill

**Figure 3.** Drilling Thrust and Torque vs. Hole Depth



**Figure 4.** The main wear pattern of WC and coated WC tools when drilling CFRP

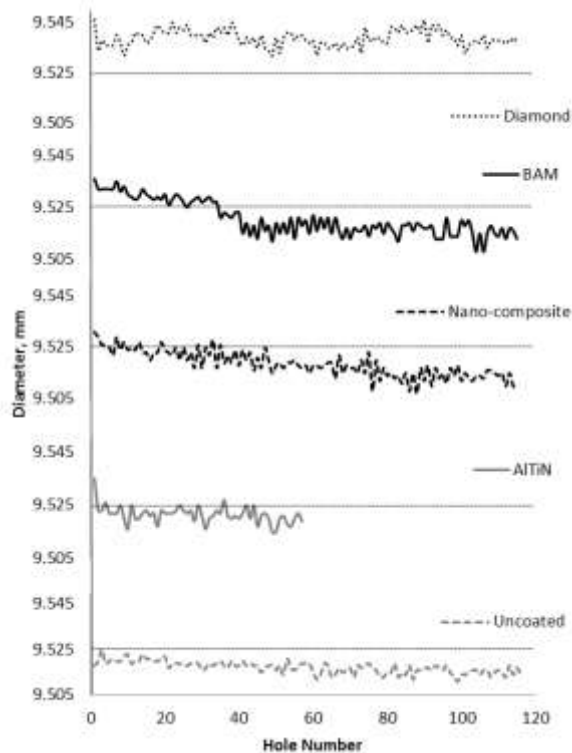
|         | Uncoated  | Diamond   | Nanocomposite  | AlTiN   |
|---------|---|---|--|---|
| Hole 0  |    |    |    |    |
| Hole 20 |    |    |    |    |
| Hole 40 |  |  |  |  |
| Hole 60 |  |  |  |  |
| Hole 80 |  |  |  |  |

**Figure 5.** SEM pictures of uncoated, diamond, nanocomposite and AlTiN coated drill margins

The main wear pattern was found to be edge rounding for all types of drills. This is due to the brittle nature of CFRP and the absence of a stagnation zone which is common to most types of metal machining [9]. This caused a rapid dulling of the cutting edge. The resistance to edge rounding wear varied with the coatings. The non-diamond coating wears faster than the carbide substructure. Figure 4 shows that the coating protects the carbide but this increases the cutting edge radius. Diamond coating showed the best results with a significant reduction in wear while AlTiN coatings provide no benefit in protecting the drill. Figure 5 shows the SEM pictures of the drill cutting edge at the corners every 20 holes.

### 3.2 Hole Size and Hole Roundness

Overall, the uncoated drills produced undersized holes (compared to the tool size of 9.525 mm) even from the first hole. This has been reported in drilling of plastics and FRP materials, where springback occurs after the tool cut the surface [13]. This means the drills pushed the CFRP material down resulting in thrust force during machining and elastic recovery occurred at CFRP after cutting. As shown in Figure 5, the average undersize amount of the uncoated drill is approximately 4  $\mu\text{m}$  for the first 20 holes. Diamond coating alone consistently produced a hole over the drill size with little change in hole diameter with an increase in hole number. The amount of hole diameter over drill diameter ranges from 5  $\mu\text{m}$  to 20  $\mu\text{m}$ . This is simply because the diamond coating thickness is 12.5  $\mu\text{m}$ . Because diamond had superior tool wear resistance, no significant trend can be observed with the change of hole size.

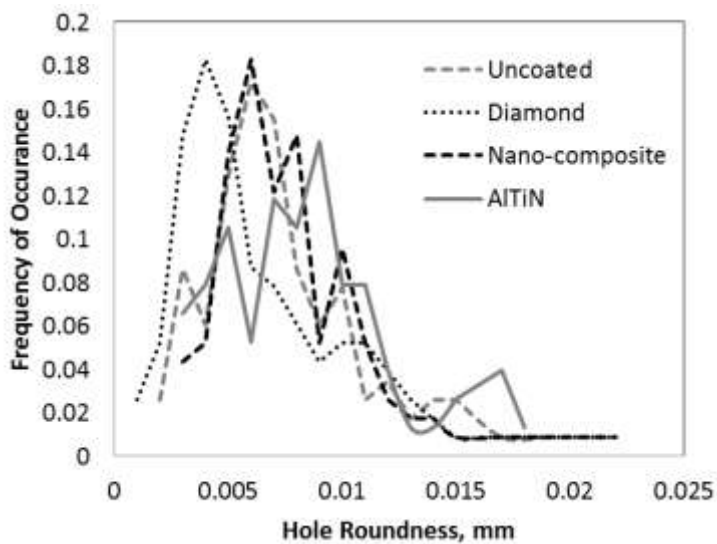


**Figure 6.** Comparison of Hole Diameter as a function of Hole Number for various coated tools.(the dotted line = the original drill diameter of 9.525 mm)

The uncoated drill and other coated tools show a decreasing trend in hole diameter due to tool wear. The average diameter of the uncoated drill is approximately 9.521 mm for the first 20 holes and

becomes 9.512 mm at the 110th hole. The hole size decreased steadily with increasing hole number. The rate of hole size reduction is close to 0.08  $\mu\text{m}$  per hole drilled.

Unlike the uncoated drill, the AlTiN and nanocomposite coated tools show a two-phase change in hole diameter with tool wear. The hole diameter decreased rapidly up to approximately 50 holes. For the nanocomposite drill, the rate of hole size reduction from the 1<sup>st</sup> hole to the 50<sup>th</sup> hole is close to 0.15  $\mu\text{m}$  per hole drilled. After the 60<sup>th</sup> hole, the hole size is very similar to that produced by the uncoated drill. The change in hole diameter corresponds for the initial wear pattern to the coating thickness. For nanocomposite coating the hole diameter initially starts at 9.530 mm and linearly decreases to 9.522 mm after 50 holes. This change is just over twice the nanocomposite thickness of 3.5  $\mu\text{m}$ . The change is twice the coating thickness as the coating is worn off of both margins of the drills. The similar trend was evident in the AlTiN coated drill up to 60 holes, but there are not enough data to explain beyond the 60th hole due to drill failure.



**Figure 7.** Hole Roundness as a function of Frequency for various coated tools.

A statistical presentation of the hole roundness is shown in Fig. 6. This shows the various coatings compared to the overall performance in hole roundness for the entire holes. Wear of the coating was found to progress very little in the hole roundness value. The diamond coated drill produced the greatest overall lower hole roundness. Highest roundness occurred at 5  $\mu\text{m}$ . The uncoated and nanocomposite coated drills have similar results where the highest roundness peak was 7  $\mu\text{m}$ . This may be due to the similar wear patterns that all drills except the diamond coated drill exhibited.

### 3.3 Surface Roughness

The mean roughness, Ra, and the maximum height of the profiles, Rt, rose slightly with tool wear, as shown in Table 1. Of the various coatings tested the diamond coated drill showed the slightly better performance overall. However, the Ra values for holes drilled regardless of the coating conditions range from 0.89  $\mu\text{m}$  to 2.35  $\mu\text{m}$ . When looking at the Rt values, the diamond coated tool showed consistently lower surface roughness than other drills. This is due to its superior wear resistance and sharp edge remaining over the holes. The other drills showed a similar rise in surface roughness with tool wear.

**Table 1.** Surface roughness in  $\mu\text{m}$  for various coated tools up to 80 holes

| Hole #         |    | 1-10       | 11-20      | 21-30      | 31-40      | 41-50      | 51-60      | 61-70      | 71-80       |
|----------------|----|------------|------------|------------|------------|------------|------------|------------|-------------|
| Uncoated       | Ra | 1.73±0.3   | 2.13±0.35  | 1.72±0.36  | 1.65±0.26  | 1.64±0.25  | 1.49±0.36  | 1.87±0.58  | 2.16±0.45   |
|                | Rt | 24.36±5.1  | 25.46±3.98 | 20.94±6.58 | 21.39±5.18 | 18.52±3.6  | 16.33±5.21 | 24±6.78    | 31.72±10.04 |
| Diamond        | Ra | 0.9±0.11   | 1.4±0.2    | 1.59±0.19  | 1.61±0.24  | 1.44±0.08  | 1.57±0.16  | 1.56±0.3   | 1.41±0.24   |
|                | Rt | 8.12±1.81  | 10.69±2.07 | 12.11±2.2  | 12.53±2.34 | 11.58±1.28 | 12.88±2.94 | 14.26±3.69 | 13.52±2.79  |
| Nano-composite | Ra | 1.82±0.21  | 2.35±0.4   | 1.62±0.39  | 1.91±0.16  | 1.79±0.18  | 1.44±0.14  | 1.93±0.61  | 1.74±0.2    |
|                | Rt | 28.99±8.41 | 28.34±7.58 | 18.95±6.42 | 22.79±2.07 | 24.4±5.95  | 15.36±1.76 | 25.66±12   | 22.3±7.54   |
| AlTiN          | Ra | 1.14±0.19  | 1.3±0.38   | 0.91±0.14  | 1.05±0.26  | 0.89±0.21  | 1.17±0.39  | 1.95±0.33  |             |
|                | Rt | 13.53±4.21 | 13.4±5.25  | 10±2.48    | 11.37±2.8  | 10.2±2.56  | 14.34±6.49 | 23.02±6.38 |             |

**Table 2.** Entry Delamination Factor ( $F_d$ ) for hole numbers and various tool coatings up to 80 holes

| Hole #         | 1-10      | 11-20     | 21-30     | 31-40     | 41-50     | 51-60     | 61-70     | 71-80     |
|----------------|-----------|-----------|-----------|-----------|-----------|-----------|-----------|-----------|
| Uncoated       | 1.35±0.1  | 1.41±0.15 | 1.47±0.09 | 1.46±0.19 | 1.53±0.18 | 1.51±0.12 | 1.42±0.1  | 1.44±0.13 |
| Diamond        | 1.28±0.15 | 1.38±0.13 | 1.5±0.16  | 1.69±0.12 | 1.55±0.16 | 1.53±0.21 | 1.74±0.2  | 1.55±0.12 |
| Nano-composite | 1.2±0.08  | 1.19±0.04 | 1.33±0.17 | 1.18±0.05 | 1.28±0.05 | 1.2±0.08  | 1.23±0.11 | 1.47±0.22 |
| AlTiN          | 1.3±0.07  | 1.4±0.03  | 1.39±0.09 | 1.38±0.11 | 1.34±0.14 | 1.24±0.07 | 1.25±0.05 | 1.26±0.01 |

### 3.4 Entry Delamination

Delamination factor ( $F_d$ ) was used to assess entry delamination quantitatively.  $F_d$  can be defined as the ratio of the maximum entry delamination diameter to the hole diameter. Figure 7 shows the method of assessing  $F_d$ .

$$F_d = \frac{D_{max}}{D} \quad (1)$$

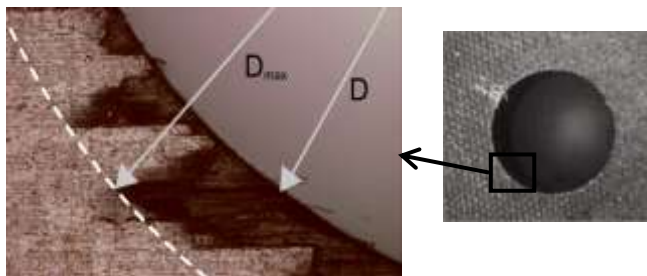
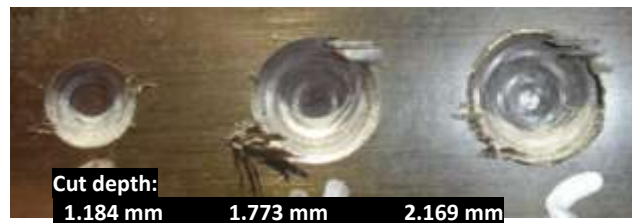
**Figure 8.** Demonstration of entry delamination variables: hole diameter ( $D$ ) and delamination diameter ( $D_{max}$ ).

Table 2 shows the change in entry delamination factor with hole number. Overall, delamination factor increases with increasing hole number due to tool wear. Regardless of the tools, average delamination factors for the first ten holes are slightly lower than following holes. It means tool wear may affect entry delamination. However, entry delamination doesn't increase with increasing hole number. Entry delamination ranges approximately 1.2 to 1.7 mm regardless of hole number and drill type. This result agrees well with the previous study conducted by Khashaba et al [6] that entry delamination did not increase with the amount of drill pre-wear regardless of the drilling feed rate.

Note that the diamond coated drill did not show less entry delamination than other drills. Uncoated, and AlTiN coated showed slight increases, though less than diamond coated, in entry delamination. The nanocomposite coated drill showed the lowest delamination damage. One of the main causes of entry delamination is peel-up [6]. With peel-up the cutting edge of the drill first abrades the laminate. Then by moving forward tends to pull the abraded material way along the flute. The surface plies are separated and severely bent leading to Mode III fracture [15]. This tends to separate and severe bend the surface plies leading to its fracture under Mode III loading. The material spirals up before it is machined completely. This peels the fibers upwards to separate from the work piece. This is why entry delamination occurs mostly where the angle between fibers and cutting direction becomes negative [16]. In order to investigate the entry delamination formation mechanism, drilling experiments with multiple depths were conducted with uncoated, diamond coated, and nanocomposite coated drills. All the drills used were worn after making 120 holes. Various drill penetration depths were 0.198 mm, 0.592 mm, 1.184 mm, 1.773 mm and 2.169 mm and these depths coincide with cutting lips engagement of 10%, 30%, 60%, 90%, and 110%, respectively, in the vertical direction. Note that entry delamination was not observed at the drill penetration of 0.198 mm and 0.592 mm, where mostly chisel edge is engaged on the material. Figure 8 presents entry delamination when both the chisel edge and the drill cutting lips penetrated the material to depths of 1.184 mm, 1.773 mm and 2.169 mm. For each depth entry delamination occurs mostly where the cutting direction becomes negative to the fiber direction. In addition, severe entry delamination occurs when the depth is 1.773 mm or 90% of the cutting lips engagement in the vertical direction. This means entry delamination forms even before the margin enters the material. Entry delamination occurs due to peel-up from the cutting lips and occurs before the margin contacts the material.



(a) Uncoated carbide drill



(b) Diamond coated drill



(c) Nanocomposite coated drill

**Figure 9.** Entry delamination at various hole depths and coatings.

#### 4. Summary

The hole quality of diamond, nanocomposite and AlTiN coated and uncoated carbide drills were investigated when drilling of CFRP. The change in hole quality with tool wear of the various coatings was also studied. The diamond coated drill showed the most consistent hole size and lowest roundness because of its superior wear resistance. The other coated tools showed a two-phase hole size trend of coating removal and then carbide substrate wear. It was found that delamination damage increased with tool wear. Of the various coatings tested the diamond coated drill showed slightly better performance overall in terms of hole size, hole roundness, and surface roughness. Entry delamination remained approximately 1.2 to 1.7 mm regardless of hole number and drill type. This may be due to the random nature of peel-up from the cutting lips, resulting in entry delamination. The overall performance of the nanocomposite and AlTiN coated drills are not impressive when drilling CFRP when compared to the uncoated drill. These tools showed better hole quality initially than the uncoated. However, wear of coatings led to a decrease in hole quality.

#### 5. References

- [1] Rajakumar P and Vijayaraghavan L. (2012), Drilling of carbon fibre reinforced plastic (CFRP) composites – a review *Int. J. Mach. Tools and Manufact.* 43, (1-4), 43-67.
- [2] Park K., Beal, A., Kim, D., Kwon, P., Lantrip, J., (2011) "Tool wear in drilling of composite/titanium stacks with carbide and polycrystalline diamond tools" *Wear*, Vol. 271 (11-12), pg. 2826-2835.
- [3] Rawat, S., Attia, H., (2009), "Wear mechanisms and tool life management of WC–Co drills during dry high speed drilling of woven carbon fibre composites." *Wear*, 267(5-8), 1022-1030.
- [4] Krishnaraj, V., Vijayarangan, S., Davim, J. P., (2008), An experimental and statistical study on the effect of drill geometries on force and hole quality in drilling of glass fibre reinforced plastic, *Int. J. of Materials and Product Technology* 32 (2/3), 264 – 275.
- [5] Carvajal, R., González-R, P. L., Lozano, S., (2011) Research study of factors affecting difference between hole diameters in hybrid metal-composite drilling, *Proceedings of the Institution of Mechanical Engineers, Part B: Journal of Engineering Manufacture*, 225, 991-1000.
- [6] Khashaba, U.A. , El-Sonbaty, I.A., Selmy, A.I., Megahed, A.A., (2010), Machinability analysis in drilling woven GFR-epoxy composites- Part II - Effect of drill wear, *Composites: Part A*, 41, 1130-1137.
- [7] Faria, P.E., Campos Rubio, J.C., Abrão, A.M., Davim, J.P., (2009) Dimensional and Geometric Deviations Induced by Drilling of Polymeric Composite, *Journal of Reinforced Plastics and Composites*, 28, 2353-2363.

- [8] Tsao, C.C. and Hocheng, H. (2008), Evaluation of thrust force and surface roughness in drilling composite materials using Taguchi analysis and neural network. *Journal of Materials Processing Technology*. 203, 342-348.
- [9] Davim, J.P. and Reis, Pedro. (2003), Study of delamination in drilling carbon fiber reinforced plastics (CFRP) using design experiments. *Composite Structures*. 59, 481-487
- [10] Wang, X., Kwon, P., Kim, D., & Sturtevant, C. (2012). Tool Wear of Ultra-Hard Coatings in Drilling CFRP. *Proceedings of North American Manufacturing Research Institute/Society of Manufacturing Engineers*, South Bend, IN, June 3-8, 2012.
- [11] Brinksmeier E. and Janssen R. (2002), Drilling of Multi-Layer Composite Materials consisting of Carbon Fiber Reinforced Plastics (CFRP), Titanium and Aluminum Alloys *CIRP Annals – Manufacturing Technology*. 51, 87-90.
- [12] Zitoune, R., Krishnaraj, V., Almagbouacif B.S., Collombet F., Sima M. and Jolin A. (2012), Influence of machining parameters and new nano-coated tool on drilling performance of CFRP/Aluminum sandwich. *Composites: Part B*. 43, 1480-1488
- [13] Shya I.S., Soo S.L., Aspinwall D.K., Bradley S., Perry R., Harden P., and Dawson S. (2011), Hole quality assessment following drilling of metallic-composite stacks. *Int. J. Mach. Tools and Manufacture*. 51, 569-578.
- [14] Kim D., Ramulu M., (2004) "Drilling process optimization for graphite/bismaleimide-titanium alloy stacks" *Composite Structures* 63, 101-114.
- [15] Di Paolo, G., S. G. Kapoor, and R. E. De Vor, (1996) "An Experimental Investigation of the Crack Growth Phenomenon for Drilling Fiber-Reinforced Composite Materials," *Journal of Engineering for Industry, ASME Transaction* 118, 104-110.
- [16] Colligan, K.; Ramulu, M., (1991) Delamination in surface plies of graphite/epoxy caused by the edge trimming process, *Processing and manufacturing of composite materials*; 112th ASME Winter Annual Meeting, Atlanta, GA, Dec. 1-6, (A93-32021 12-37), p. 113-125



## WSU-TASK 2. STRUCTURAL INTEGRITY IMPROVEMENT OF THE FRP JOINTS.

### 1 INTRODUCTION

Composite materials have revolutionized the way that designers tackle complex engineering problems. Manufacturers from almost all fields have incorporated composites into designs for everything from boats, to aircraft, to cars, to automobiles and wind turbine blades [1-4]. The difficulty with incorporating composites lies in joining material sections together. Composite joints can be created by adhesion or by mechanical fastening using bolts or fasteners [5-13]. Adhesion offers many advantages over mechanical fastening such as high strength-to weight ratio, electrical/thermal insulation, increased conductivity and corrosion/fatigue resistance [5,6]. Mechanical fastening with a pin is a common method of composite joining due to its low cost, simplicity and ease of repair/replacement [7-13].

The fit between the pin and the hole is one of the key parameters that help to determine the strength of pin-joined composites. According to ISO286, the fit ranges can be divided into clearance, transition and interference. A clearance fit results in limits of size that assure clearance between assembled mating parts. Interference fit has limits of size that always result in interference between mating parts. Most former researchers have followed an interference percent theory ( $I = (D_p - D_h)/D_h$ ), where  $D_p$  equals pin diameter and  $D_h$  equals hole diameter, in order to define the amount of interference [11]. A transition fit is either a slight clearance or interference fit. In general, designers utilized clearance fit for the composite materials, because interference fit joining may cause severe damage around the hole which reduces overall joint strength [14, 15]. However, clearance-fit pins, in all cases, lead to higher stress concentrations since the contact area of the pin does not react with the entire radius of the drilled hole. In addition, clearance fit pins allow moisture intrusion and escape, which limits their use in many applications where fluids must be contained to either prevent leaks and spills, or to prevent the composite itself from absorbing moisture which causes increased inter-laminar degradation. Some studies have shown the benefits of interference-fit pins on the composite joints [16-19]. Application of interference-fit pins into composites reduces the magnitude of the local oscillatory stress components under dynamic loadings which results in improved fatigue life [17, 18]. Recently, Kiral [19] reported that use of interference-fit was beneficial in the static strength of the pin-joined GFRP. Although some benefits of interference-fit pins have been studied for the strength of composite joints reported, the experimental studies concerning fatigue enhancement of interference-fit pin-loaded composite holes are very limited.

Many researchers have conducted numerical studies on the stress distribution of the bolt or pin joined FRP composites. Due to the computational difficulties involved in modeling and analysis of the real 3-D structure, many numerical studies have simplified their composite joint problems by using a plate with a hole as a 2-D shell with plane stress assumptions. The anisotropy of the composite material adds to the complexity of the contact analysis as well. With the recent increases in computing power, 3-D FEA has become feasible. The laminates have been modeled either with one or more orthotropic solid elements per ply or with layered solid elements representing multiple plies in order to account for through-thickness variations in stiffness. The earlier study [20] of 3-D FEA for composite joints did not consider contact between the hole and the bolt, but made a simple assumption to simulate the presence of the bolt, such as fixing the radial displacement of the nodes around the hole. Also, many

researchers conducted frictionless contact analyses for composite joint based on assumption that the friction was insignificant. Lanza et al. [11] performed a nonlinear contact analysis using a 2-D FEA study to examine the elastic behavior of a cross-ply fibre glass-reinforced epoxy laminate loaded in tension through a pin fitted with clearance and interference. They found that clearance causes high compressive stress in the bearing area and interference has beneficial effects to the joint. Pierron et al. [21] have studied the behavior of woven glass fibre epoxy pin joints both numerically and experimentally, with particular attention given to the sensitivity of the model to different parameters such as clearance, friction, and material nonlinearity. They reported that FE model required considering frictional contact condition and material nonlinearity to simulate the behavior of the composite joint accurately. Pradhan and Babu [18] performed non-linear contact analysis to study the effects of interference for different material cases. They formulated 3-D FE models to investigate the effects of interference-fits in pin-loaded laminates and considered friction between the pin and the hole surface to simulate the real situation.

GFRP composite fabrication processes used in this study are the hand lay-up (HL), vacuum infusion (VI), and hybrid (HL+VI) processes. The HL technique, is by large the most widely used composite fabrication technique due to its advantages including low capital cost and large structure capability. However, it causes a major health risk for operators by the resin fumes that exhale from the process. Consequently, manufacturers of fiber-reinforced composite laminates are looking for cleaner and friendlier work environments and processes. The VI process is now being used as a useful alternative to the traditional HL technique. While in the typical HL technique, reinforcements are laid into the mold and manually wet out using brushes or rollers and then vacuum is used to remove the resin in excess, VI takes a different approach, in that a vacuum is drawn while the materials are still dry. Once vacuum is achieved, resin is literally sucked into the laminate via carefully placed tubing. Ideally, any excess resin that is introduced will eventually be sucked out into the vacuum line. Therefore, besides environmental issues, VI potentially offers another important benefit over HL, in that it should allow for a very predictable resin usage approaching prepreg levels of resin content. Because of the improvement in the fiber-to-resin ratio, laminates manufactured by VI should be stronger and lighter as compared to laminates manufactured by HL [22]. Here the hybrid term refers to composite material formed by applying the HL technique to construct the exterior lay-up against the mold, followed by a VI process on the interior once the HL portion is cured. This type of hybrid composites is beneficial to a structure like the composite exterior skins, which should possess a good resistance to wave impact or local shock loads as well as good structural integrity with high stiffness and strength [1, 22].

The present project aims to investigate the effect of interference-fit on the strength and fatigue life of pin-joined GFRP fabricated from various manufacturing processes. Three GFRP fabrication processes namely HL, VI and hybrid (HL+VI) are used. The interference percent ranges from 0% to 2% when the pin diameter is consistent at 6.35 mm. Stainless steel pins with interference-fits were mechanically inserted. All test specimens have consistent the width-to-diameter ( $W/D = 4$ ) and edge distance-to-diameter ( $E/D = 3$ ) ratios in order to minimize the effect of specimen geometries on failure modes and strengths. The interference-fit pin installed GFRP have been analyzed with 3-D linear FEA considering contact with friction. The radial and tangential strains of the vicinity of hole are obtained from the FEA results. The interference-fit pin installation experiments were conducted using stainless steel dowel pins applied to hand lay-up processed GFRP samples. The pin insertion force and strains around the hole in both radial and tangential directions were measured during the experiments in order

to verify the FEA results. Bearing strength and fatigue life of the pin-loaded fibre reinforced plastics (FRP) with various interference-fit percents were investigated experimentally. Damage in the composite holes was observed using an optical microscope. Fractography and failure mode of the joints are discussed.

## **2 EXPERIMENTAL METHODS**

### **2.1 Material Systems and Fabrication Processes.**

Table 1 contains references to the different sample names along with fabrication process, number of plies, lay-up sequence, glass and matrix materials, thickness, and fiber volume %. These types of GFRP composites are widely used in marine and wind turbine structures [1, 23]. All the material systems consist of [M/90/0] lamina, which are a combination of one layer of chopped strand mat, one layer of 90 degree unidirectional fibers, and one layer of 0 degree unidirectional fibers. The chopped strand mat contains randomly oriented fibers with the average length of 50.8 mm or 2 inches. Table 2 presents the mechanical properties of each sample those were determined as an average of 5 specimens with 0 degree fiber directional loading for each test.

The conventional hand lay-up (HL) process was used to consolidate the HL sample. Glass fibers were placed manually inside of a mold then matrix material was spread evenly over the fiber layers. Entrapped air was then removed with squeegees and rollers. Hardening of the fiber/matrix system was accomplished at ambient temperature. In order to complete the VI process, fibers were placed into or on top of a mold. The distribution media, highly permeable fabric, was placed on top of the fibers in order to spread the resin efficiently throughout the sample. A system of tubes connected to resin reservoirs was then placed to distribute resin material evenly throughout the sample. Plastic film, so called vacuum bag, was laid over the entire system and sealed at the sides. A vent line connected to a vacuum source was also placed under the bagging film. Vacuum was then applied in order to pull the resin fluid through the tubing and into the fiber in an evenly distributed fashion. The injection continued until the entire fibers was completely infused so additional resin bled through the vent line. Preliminary testing showed that the vacuum pressure should be at least 67.5 kPa in order to gain the largest benefit in void reduction [1]. The VI sample was processed at 94.5 kPa in order to assure limited void content and complete fiber wet-out. Similar to HL, consolidation of the fiber/matrix system in VI was accomplished at ambient temperature. For the hybrid samples, the first sequence of layers was manufactured using the HL technique and left to cure until the additional layers of fibers were added and fabricated using the VI technique.

**Table 1 Material Types and Descriptions**

| Sample Name | No. of Plies | Orientation   | Glass Material              | Matrix material | Thickness (mm) | Fiber Vol. % |
|-------------|--------------|---|-----------------------------|-----------------|----------------|--------------|
| HL          | 12           | [M/90/0] <sub>4</sub>   | Owens Corning CDM 2408      | B               | 5.948          | 30.97        |
| VI          | 9            | [M/90/0] <sub>3</sub>   | Vectorply E-LTM 3610        | A               | 3.541          | 52.43        |
| HYB         | 19           | [M <sub>4</sub> /(M/90/0)] <sub>HL</sub><br>+[(M/90/0) <sub>4</sub> ] <sub>VI</sub> | Owens Corning CDM 2408 (HL) | B               | 7.792          | 38.82        |
|             |              |   | Vectorply E-LTM 3610 (VI)   | A               |                |              |

CDM 2408: Non-crimp woven, 1,080 g/sq.m (0°: 414g/sq.m, 90°: 391g/sq.m, Chopped mat: 275g/sq.m).

E-LTM 3610: Non-crimp woven, 1,520 g/sq.m (0°: 608g/sq.m, 90°: 608g/sq.m, Chopped mat: 305g/sq.m)

M = mat : chopped strand mat layer with approximately 0.25 mm thickness after curing

A = Derakane Momentum 411-200 Epoxy Vinyl Ester: Density = 1.14 g/cc

B = Reichhold Hydrex 100 Vinyl Ester: Density = 1.16 g/cc

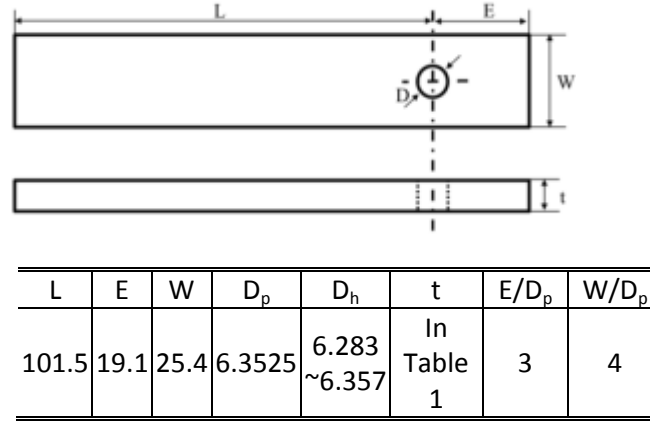
For all matrix materials the catalyst is 2 wt% methyl ethyl ketone peroxide.

**Table 2 Mechanical properties GFRP coupons tested with 0 degree fiber directional loading**

| Sample Name | Tensile properties |               |              | Compressive properties |               |              |
|-------------|--------------------|---------------|--------------|------------------------|---------------|--------------|
|             | UTS (MPa)          | Modulus (GPa) | Max % Strain | UCS (MPa)              | Modulus (GPa) | Max % Strain |
| HL          | 260.56             | 15.32         | 2.279        | 279.95                 | 17.33         | 1.973        |
| VI          | 430.50             | 24.48         | 2.288        | 322.02                 | 27.90         | 1.408        |
| HYB         | 278.46             | 18.55         | 2.219        | 263.32                 | 25.37         | 1.309        |

## 2.2 Drilling Procedures.

Sample sizes for quasi-static and fatigue testing are chosen based on ASTM D953-02 Standard Test Method for Bearing Strength of Plastics (See Fig. 1).



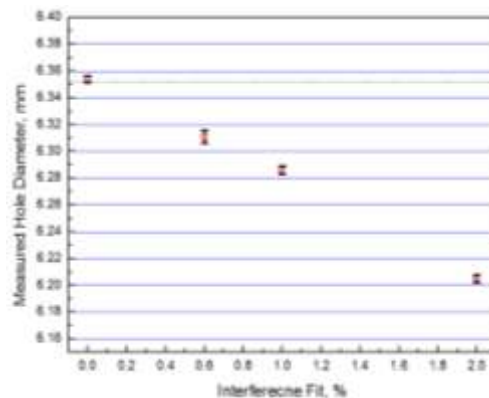
**Fig. 1 Quasi-static / fatigue sample size (unit=mm),  $D_p$  = pin diameter,  $D_h$  = hole diameter.**

For each interference fit percent (0, 0.6, 1), at least 10 coupons were created from each type of composite panel tested. This yielded enough coupons for 5 tensile tests and 5 fatigue tests for each interference fit percent and each laminate type. Width to pin diameter ( $W/D_p$ ) and Edge distances to pin diameter ratio ( $E/D_p$ ) are very important factors for the failure mode of pin-loaded joints [24,25]. The  $E/D_p$  smaller than 2 and  $W/D_p$  smaller than 3 have proven to affect the amount of bearing strength attainable by causing premature failure in net tension, shear-out, and cleavage-tension. All specimens were manufactured with 3 of  $E/D_p$  and 4 of  $W/D_p$ . This means that  $E/D_p$  and  $W/D_p$  may fail in bearing.

In order to create interference fits in the composite material it was necessary to drive pins into an undersized hole. To accomplish this task economically, a standard dowel pin (18-8 stainless steel) size of 38.1mm length and 6.353 mm diameter was selected. The pins are chamfered slightly at each end, which made driving them in much less damaging to the composite material. The hole in the composite materials was created by drilling undersize and then reaming to desired finished dimensions with a HAAS CNC milling machine. A solid carbide slow spiral  $\Phi$  5.953mm size drill bit was employed to create an undersized hole in the coupon. Straight flute high speed steel reamers were then used to bring the hole to the required finished size. An intermediate  $\Phi$  6.096mm reamer was used before reaming to the final hole size for all coupons tested. Drill speed was set to 5200 RPM for a  $\Phi$  6.35mm drill. Feed was set to 0.0762 mm/rev. Flood coolant was used to remove debris, and provide cooling and lubrication. Reamer speeds of 1200 RPM with a feed of 0.0508 mm/rev proved to work very efficiently, and prolonged tool life.

Interference-fit (I) percentages between 0% and 2% were obtained. Fig. 2 shows the hole diameter distribution for each interference-fit. For  $I = 0\%$ , hole diameter was  $6.3513 \pm 0.0047$  mm while the pin diameter was  $6.3525 \pm 0.0030$  mm. This is a typical transition-fit. The hole diameter was obtained as  $6.3135 \pm 0.0098$  mm at interference-fit of 0.6%. When interference-fit becomes 1%, the

hole diameter becomes  $6.2862 \pm 0.0062$  mm. Lastly, the hole diameter is  $6.2050 \pm 0.0065$  at interference-fit of 2 %.



**Fig. 2** Measured Hole Diameter with Standard Deviation vs. Interference Fit %

### 2.3 Pin Insertion Procedure.

A tension and compression testing machine (Model 4482, Instron, USA) was used to insert the stainless steel pins into the composite coupons. Fixtures were made (Fig. 3) to allow the pin to be pressed into the hole. The pin is inserted at a rate of 1 mm per minute for a distance of 20 - 22 mm depending on the thickness of the coupon being tested. This allows enough pin protrusion for quasi-static and fatigue testing, and simulates the distance an average bolt would have to travel through the material into a structure below to fully engage a nut or a nut-plate. The composite plate is first centered below the pin using a ball gauge. The plate is then clamped using vise grips 50 mm behind the hole. A pin is inserted into the upper fixture which has a 6.375mm hole reamed 19.05mm deep in its center. The pin is then inserted to the composite specimen and the loading and displacement data are recorded.



**Fig. 3** Photo of installation process with pin installation fixture.

### 2.3 Mechanical Property Test Procedures

Static tension tests were performed in accordance with ASTM D 953. The tension and compression testing frame was utilized at a speed of 1 mm/min in the tensile direction. Data samples were taken at 20 points per second.

Fatigue testing is used to determine the expected lifespan of a component subjected to sine wave type loading. Fatigue tests were conducted on an Instron universal testing machine (Model 8802, Instron, USA) with a 250 kN capacity. This test assembly has hydraulically controlled grips which can clamp either flat or round stock. In fatigue tests, a load or stress controlled test was accomplished on the specimen. The stress ratio ( $R = \text{Min. Stress} / \text{Max. Stress}$ ) was set as 0.1 and the loading frequency was 10 Hz. Displacement versus load data was obtained for the pin in each of the fatigue tests accomplished. The displacement-load data was acquired at 200 Hz, which is equivalent to 20 data points per load cycle. The controller was set up with a displacement limit of 1 mm. This corresponds to a displacement of roughly 16% of the pin diameter, and allows for a test stoppage point for failure analysis. The maximum fatigue stress ( $S_{\max} = 172 \text{ MPa}$ ) applied during fatigue testing was determined by 80% of the static bearing strength which yields an average life expectancy greater than 10,000 cycles for the baseline transition fit ( $I = 0\%$ ) specimens. If a test specimen didn't fail at  $10^6$  stress cycles, which means the pin was not displaced by 1 mm after undergoing  $10^6$  stress cycles, then the test was suspended and that specimen was considered a run-out.

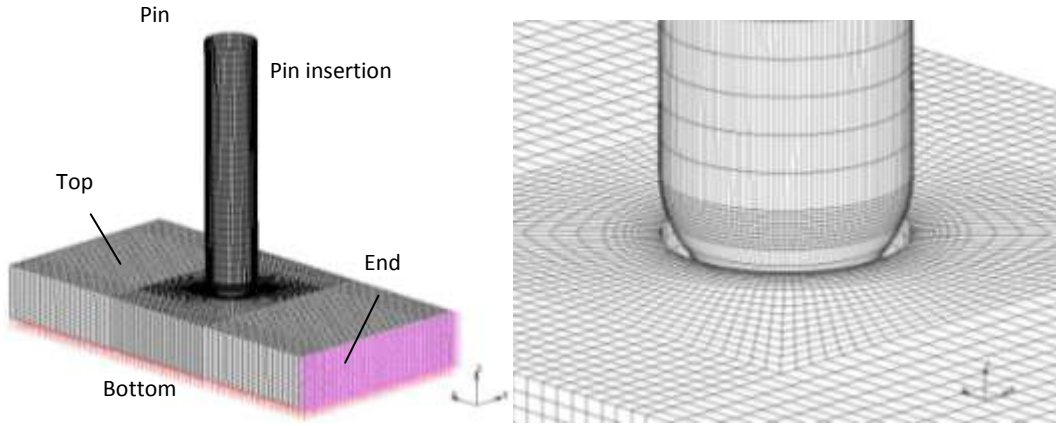
### 3. PIN INSTALLATION FE SIMULATION AND EXPERIMENTAL RESULTS

#### 3.1 FE Modeling

FE models of the interference-fit pin installed GFRP with 0.4% and 1% interference-fit conditions have been developed and analyzed with FEA software Marc 2010 (MSC Software Co., USA)[31]. Figure 4 shows the created three-dimensional model and mesh of a pin and GFRP specimen with an undersized hole, as a non-sectioned full model. The pin has been created with a number of 6,768 rigid 4-point surface elements, and has the round-shaped end to substitute the chamfered end of the real pin for simplifying FEA model. The model has 25.4 mm in width, 50.8 mm in length and 6.56 mm in thickness, and consists of 82,880 nodes and 75,000 of 8-node solid elements. The undersized hole has been created on the center of the GFRP specimen. A fine mesh has been created on the vicinity of hole for the accuracy of analysis.

As shown in Figure 4, the pin has been aligned to the hole without touching the GFRP specimen. The bottom surface of specimen has been fixed on only the Z-direction against the driving force. The end of specimen has been fixed on the X and Y-direction by considering mechanical clamping on the experimental set-up. In the analysis, the pin drives the hole toward the bottom surface of the GFRP specimen, and contact area between GFRP and the hole has a friction coefficient of 0.1 to simulate the real situation [18,32]. The total driving distance was set at 10 mm which is enough to penetrate the GFRP specimen, and has been divided into 400 sub-steps with same driving distance at each sub-step. The contact condition between the pin and the hole was updated at the end of each sub-step by using an iterative procedure to find the sub-step equilibrium state.

In this study, linear analysis was performed with an orthotropic mechanical property matrix, since the stress-strain relation of the composite material was almost linear before fracture. Mechanical tests, tensile test (ASTM D 3039) and shear test (ASTM D 5379), were performed to determine the material properties. Experimental results are shown in Table 3 along with  $E_3$ ,  $\nu_{12}$ ,  $\nu_{23}$ , and  $\nu_{31}$  values from prior research results [32].



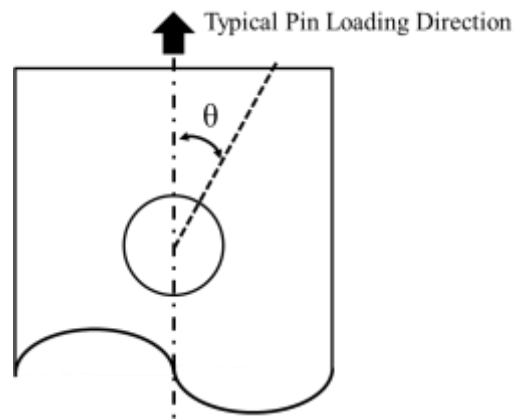
**Fig. 4** The model and boundary conditions of FEA for pin insertion

| Young's moduli |                |                | Poisson's ratios |            |            | Shear moduli      |                   |                   |
|----------------|----------------|----------------|------------------|------------|------------|-------------------|-------------------|-------------------|
| $E_1$<br>(GPa) | $E_2$<br>(GPa) | $E_3$<br>(GPa) | $\nu_{12}$       | $\nu_{23}$ | $\nu_{31}$ | $G_{12}$<br>(GPa) | $G_{23}$<br>(GPa) | $G_{31}$<br>(GPa) |
| 15.7           | 15.7           | 7.8            | 0.3              | 0.3        | 0.3        | 3.36              | 3.36              | 3.36              |

**Table 3** Mechanical Properties of GFRP for FEA

### 3.1 FE Simulation Results of the Pin Installation Process

The results of the stress analysis for 0.4% and 1.0% of interference-fit obtained from the FE analysis are presented here. Figure 5 defines the angle designation to explain the stress and strain distributions on the samples. For example, the angle becomes 0 degree ( $\theta = 0^\circ$ ) when the direction is the same with the fatigue loading direction. Figures 6 and 7 show both radial and tangential stress distributions on the composite sample surface after pin insertion with 0.4% and 1.0% of interference-fit.

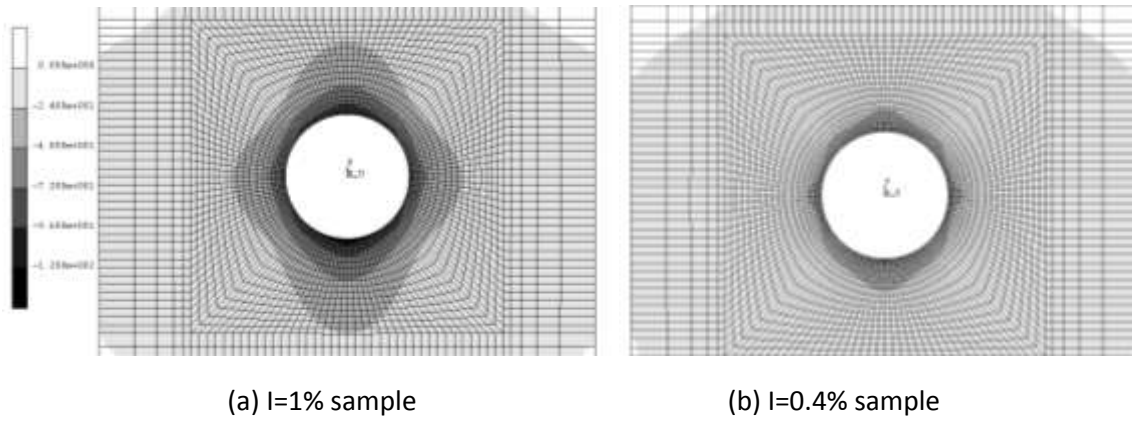


**Fig. 5** Definition of angle from the pin loading direction and sectioned plane angle during experiments

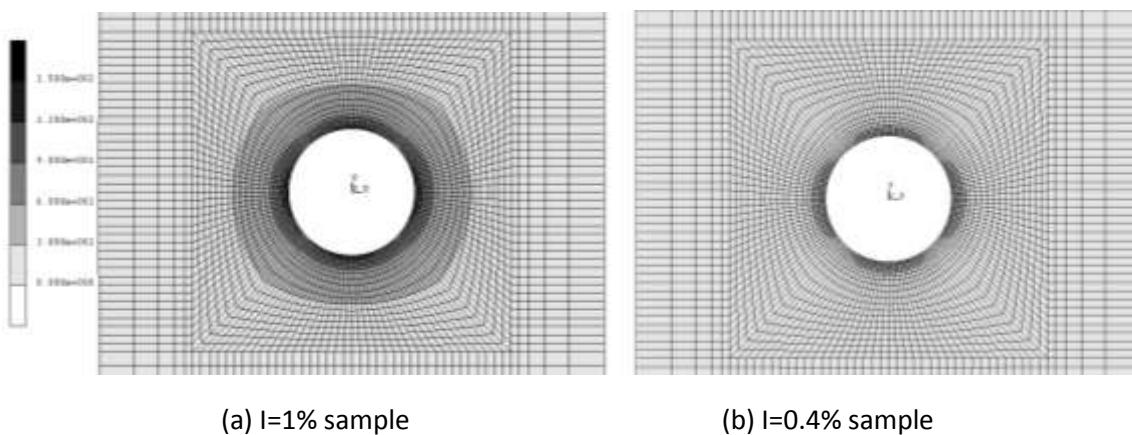
As shown in Figure 6, the radial stresses are all in compression. The amounts of radial stresses at 0 and 90 degrees are larger than that at 45 degree and this is simply because the GFRP layup is cross-ply,



which fibres are aligned at 0 and 90 degrees. When compared between 0 and 90 degrees, the maximum radial stress at 0 degree is larger than that at 90 degrees. This might be due to the constraint effect on the hole distance to the specimen edge. As shown in Fig. 2,  $E/W = 1$ , which means the distance from the hole edge to the free edge in 90 degrees is about half of that in 0 degree. Amount of radial stresses increase with increasing interference-fit percent. The maximum radial stress of interference-fit of 1% ( $I=1\%$ ) sample is approximately 1.7 times larger than that of  $I=0.4\%$ . The maximum radial stress for  $I=1.0\%$  and  $I=0.4\%$  are found to be  $-102 \text{ MPa}$  and  $-59 \text{ MPa}$ , respectively. The trend of these data is well agreed with the results from the previous studies [18, 19]. As shown in Figure 7, the tangential stresses are all in tension. The tangential stresses distributed around hole more consistently than the radial stress distribution. Similar to the case in the radial stresses, the tangential stresses becomes higher near the hole edge at the 0 and 90 degree direction over the 45 degree direction. This may be also due to fibre reinforcement at 0 and 90 degree direction. According to the results of the previous studies [11, 18], the stress magnitude was consistent regardless of the directions. This study presented stresses in both radial and tangential directions can vary depending on the angles around the hole. This discrepancy might be due to the specimen geometry and the amount of  $I\%$  used. The current study used 0.4% to 1.0% while 0.0002% to 0.04% were used for the previous studies [11,18]. Similar to the trend of the radial stress cases, amount of tangential stresses increase with increasing interference-fit percent. The maximum tangential stress of  $I=1\%$  sample is approximately 2.3 times larger than that of  $I=0.4\%$ . The maximum tangential stresses for  $I=1\%$  and  $I=0.4\%$  are found to be  $134 \text{ MPa}$  and  $57 \text{ MPa}$ , respectively.



**Fig. 6** Radial stress distribution on the vicinity of hole in MPa

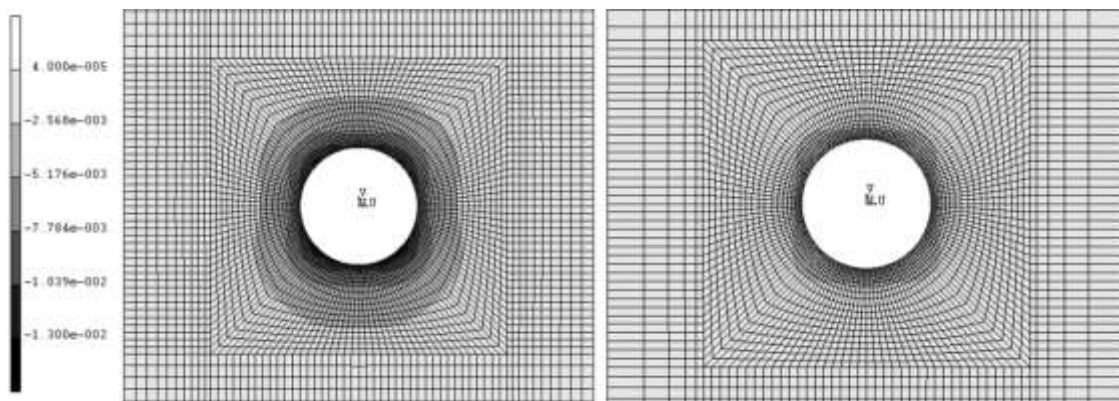


**Fig. 7** Tangential stress distribution on the vicinity of hole in MPa

Figures 8 and 9 show radial and tangential strains on the surface of GFRP samples after pin insertion with 0.4% and 1.0% of interference-fits. Overall, smaller compressive radial and tensile tangential strains have been observed at 0 degree and 90 degrees than 45 degrees, the definition came from Figure 5. It seems that the composite has been stiffened by the reinforcement when the fibre directions are the same as the GFRP hole expansion directions.

When the strains of the radial direction are compared through the specimen thickness, the radial strains on the bottom side are a little larger than the ones on the top side. It is caused by the defined boundary condition of the bottom, while the top side is still free. The constraint has been applied as a boundary condition at the bottom surfaces, 38.1mm away from the center of the hole.

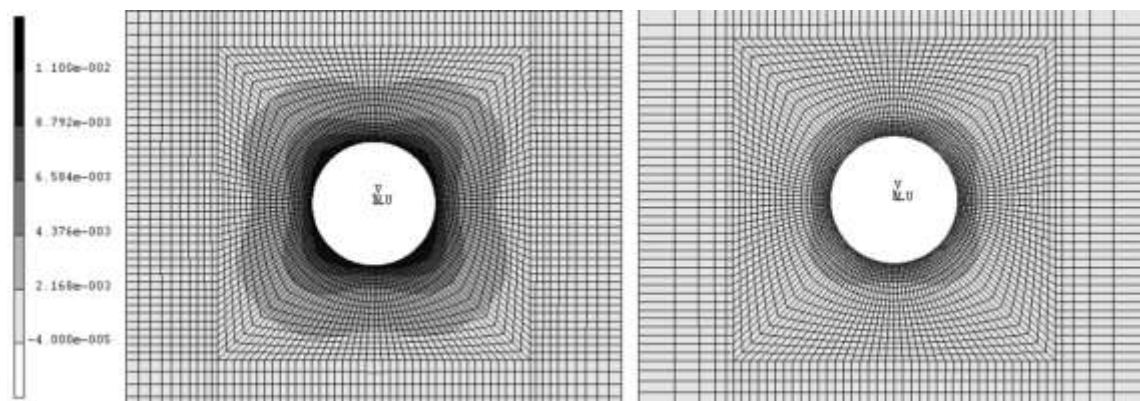
The material properties for both 0 and 90 degrees are the same for FEA because the cross ply composite material was used. However, the radial and tangential strains on the 0 degrees have larger values than 90 degrees. It means that 0 degrees have a larger residual stress than 90 degrees. It is caused by the constraint effect by a longer ligament at 0 degrees, about 22.2 mm ( $=E-D/2$  on Figure 2), and shorter ligament at 90 degrees, about 9.5mm ( $=W/2-D/2$  on Figure 2).



(a) I=1% sample

(b) I=0.4% sample

**Fig. 8** Radial strain distribution on the vicinity of hole



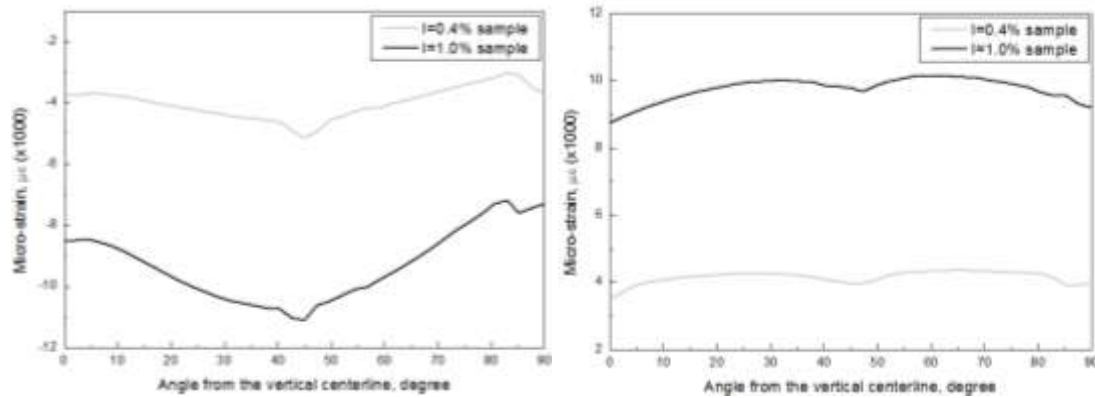
(a) I=1% sample

(b) I=0.4% sample

**Fig. 9** Tangential strain distribution on the vicinity of hole

Figures 10 and 11 shows the FEA results of strain values around the GFRP hole surface after installing 0.4% and 1.0% interference-fit pins. The model with  $I=1.0\%$  have shown the larger radial and tangential strains than that with  $I=0.4\%$ . The radial and tangential strains of  $I=1.0\%$  are 2.16~2.51 times larger (average of 2.35 times) than those of  $I=0.4\%$  at the same location.

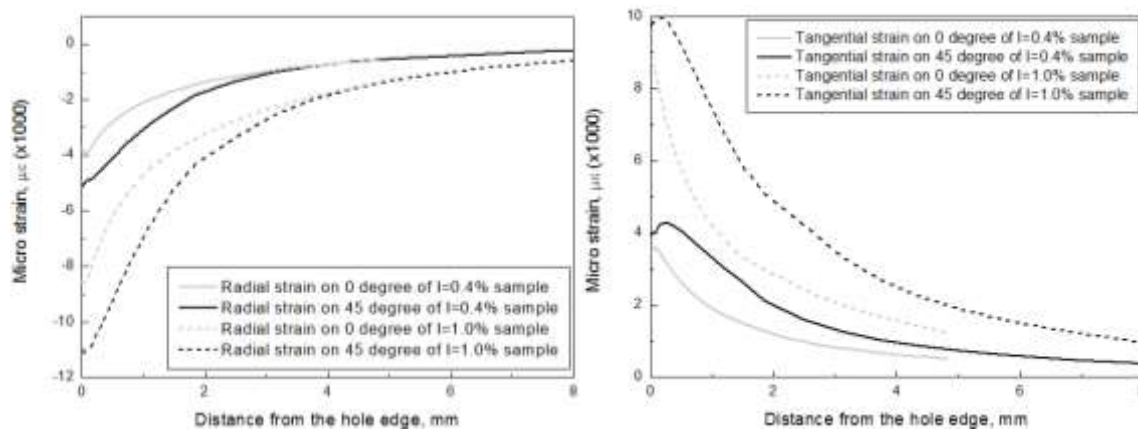
As a cross-ply material characteristic, the samples have larger strains at 45 degrees because no fibres are oriented in that direction. The radial and tangential strains at 45 degrees are larger than those at 0 degree regardless of interference-fit percent. In case of  $I=0.4\%$ , the radial strain at 45 degrees is 1.37 times larger than the strain at 0 degree. And the tangential strain at 45 degrees is 1.13 times larger than that at 0 degree. It seems that radial and tangential strains for  $I=1.0\%$  has similar magnifications with  $I=0.4\%$  at 45 degrees as there is no ply has 45 degree directional fibres.



(a) Radial strain

(b) Tangential strain

**Fig. 10** Strain distribution around the hole edge



(a) Radial strain

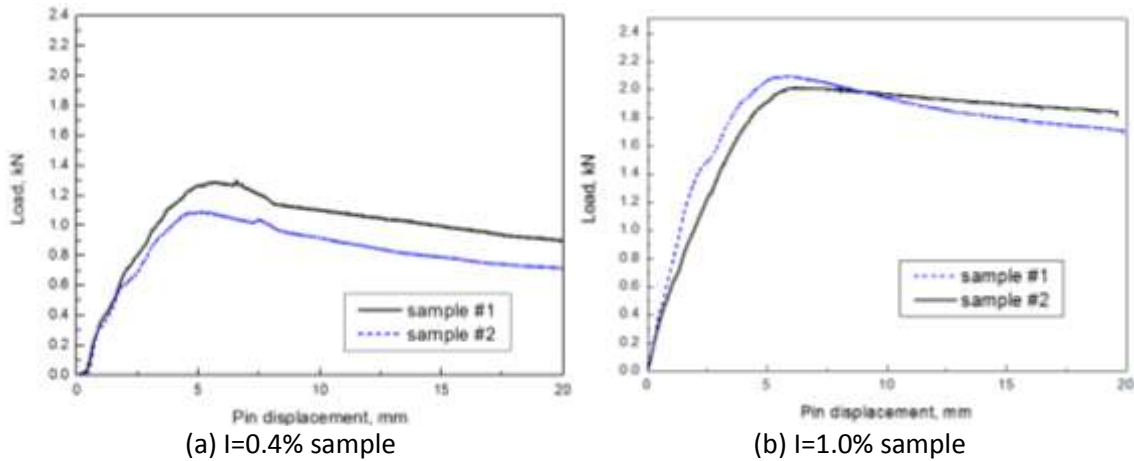
(b) Tangential strain

**Fig. 11** Directional strain distribution from the hole edge

### 3.3 Experimental verification of the pin installation process

Figure 12 shows load change over pin displacement of the pin insertion tests with  $I = 0.4\%$  and  $1.0\%$ . The insertion load increases to drive the pin into the undersized GFRP hole until the pin penetrates the specimen with the maximum value. As the pin progresses through the specimen the friction forces build, resulting in an increase in force necessary to continue inserting the pin. Maximum

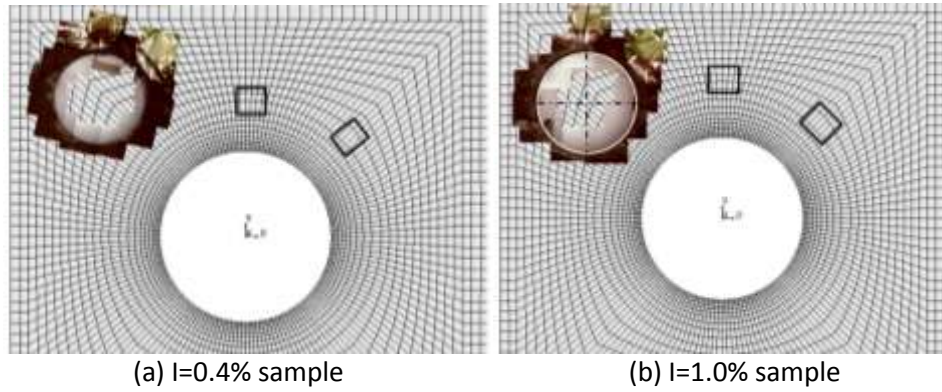
insertion load was obtained as the pin exited the hole in the bottom of the specimen. The maximum insertion load of I=1.0% sample (maximum average 2.05kN) is larger than I=0.4% sample (maximum average 1.15kN). After the pin penetrated, insertion load decreased gradually.



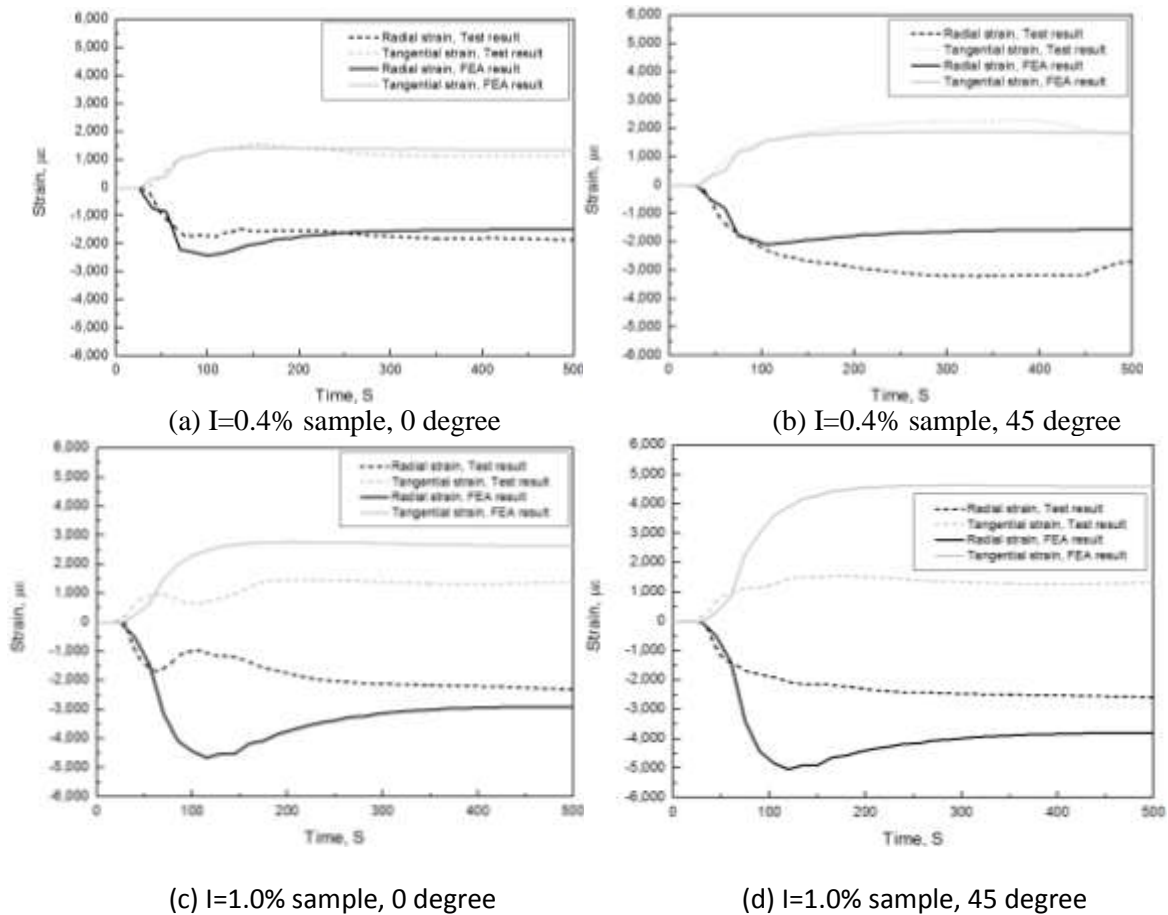
**Fig. 12** Load versus pin displacement curves during the pin installation tests

Figure 13 shows the locations of tee-rosette strain gauges attached on the test specimens. Figure 14 shows experimental and computational strain data at the strain gauge locations during pin installation. In both of I=0.4% and 1.0% results, the experimental and FEA results show an increasing trend at the initiatory stage of pin insertion, while they show a different trend at the mid and end stages. In case of I=0.4%, tangential strains from the experiments at both 0 and 45 degrees agree well with the FEA results. Experimentally obtained radial strains show, also, similar trend to the FEA results up to the peak point when the chamfer at pin head passes through the specimen surface where the strain gauges are attached. As for I=1.0%, there is no increase on radial strain after the peak point at both 0 and 45 degrees of the FEA results, which is similar with the case of I=0.4%. However, both tangential and radial strains from the experiments have 50% lower strains at the peak point region (around 120 seconds) than the strains obtained from the FEA results. This may be due to the micro-scale fibre damage around the hole due to large amount of interference-fit percent between the pin and the hole during the pin installation experiments. The fibre damage causes the loss of the reinforced stiffness by the fibres. Fibre damage might cause the increasing radial strain after the peak point during the installation experiment. FEA simulation did not consider local fibre damage in this study. After the peak point, the radial strain from the FEA results decreased slightly while the experimentally obtained radial strain values increased slightly. These discrepancies can be explained that the fibre damage might occur at the hole and pin contact area during the pin installation experiment. Fibre damage increases radial strains after the peak point during the installation experiment.

From the experimental results of the 0 degree direction, the sample of I=1.0% produces the radial strain of  $-2297\mu\epsilon$  and the tangential strain of  $1385\mu\epsilon$  after pin installation, while the radial strain of  $-1855\mu\epsilon$  and the tangential strain of  $1155\mu\epsilon$  remain at the I=0.4% sample. Even with the fibre damage, I=1.0% induced higher radial strain over I=0.4%. This means that the I=1% sample contains larger pre-compression stresses in the radial direction and pre-tensile stresses in the tangential direction around the hole vicinity over I=0.4% sample after installing the pin. This can be why the I=1% sample had longer average fatigue life over the I=0.4% sample (See Figure 1).



**Fig. 13** Tee-rosette strain gauge locations in the FE models with the actual photos (The boxes indicate the strain gauges.)

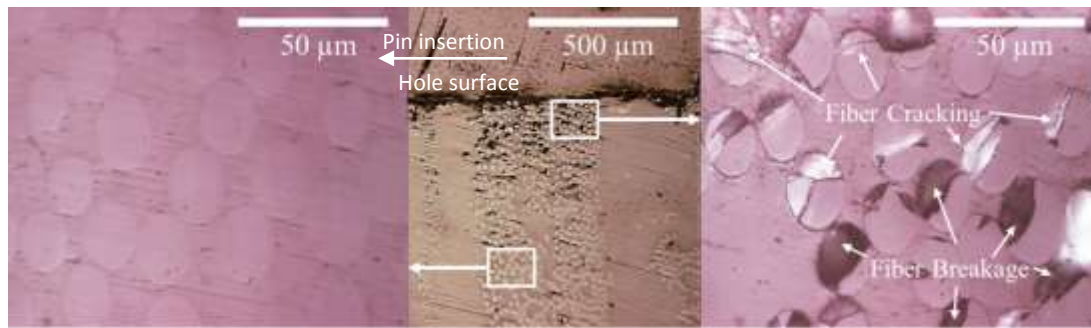


**Fig. 14** Comparisons of experiments and FEA on strains versus pin installation time

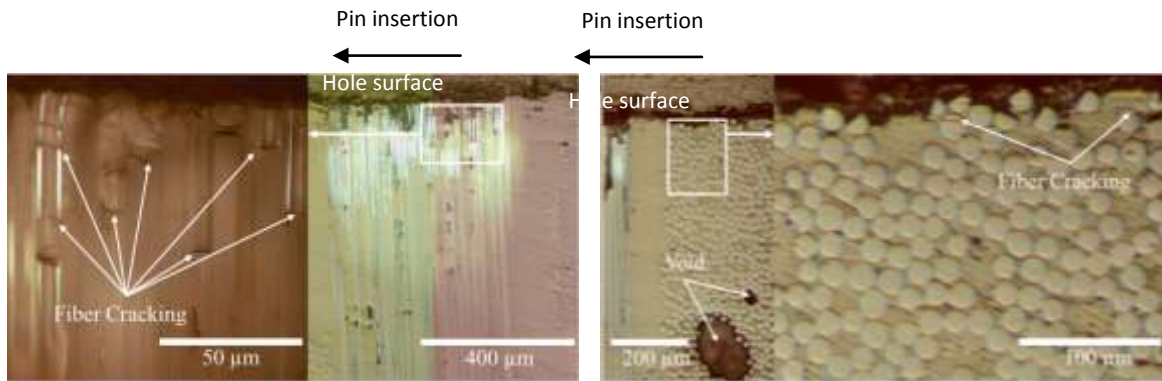
### 3.4 Micro-scale failure on the interference-fit pin installed GFRP

In order to investigate micro-scale failure occurred on the interference-fit pin installed GFRP samples, the tested specimens have been cut along the 0 degree and 45 degree; the cutting plane definition came from Figure 5. The specimens have been cut using a slow-speed diamond coated blade saw and have been observed with an optical microscope (Model MM-40, Nikon, Japan). After sectioning specimens, the pins were removed with care. The middle regions of the sectioned holes were carefully polished and presented in Figures 15 and 16.





(a) 45 degree plane showing the 90 degree ply

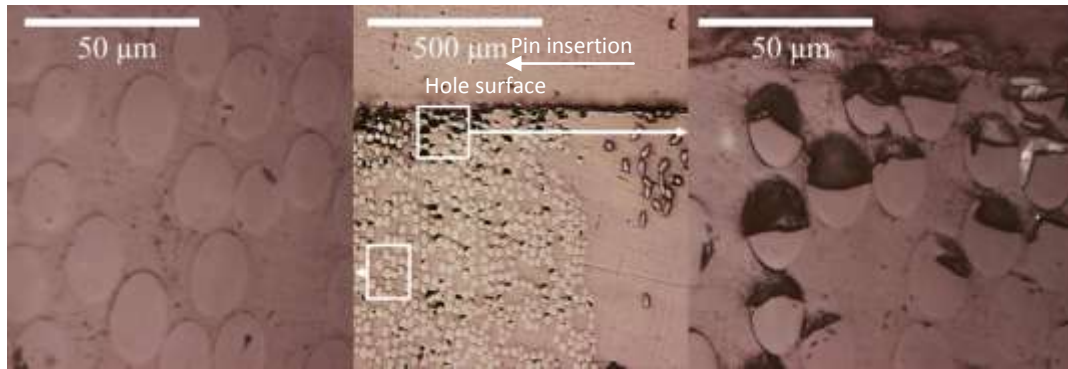


(b) 0 degree plane showing the 0 degree ply

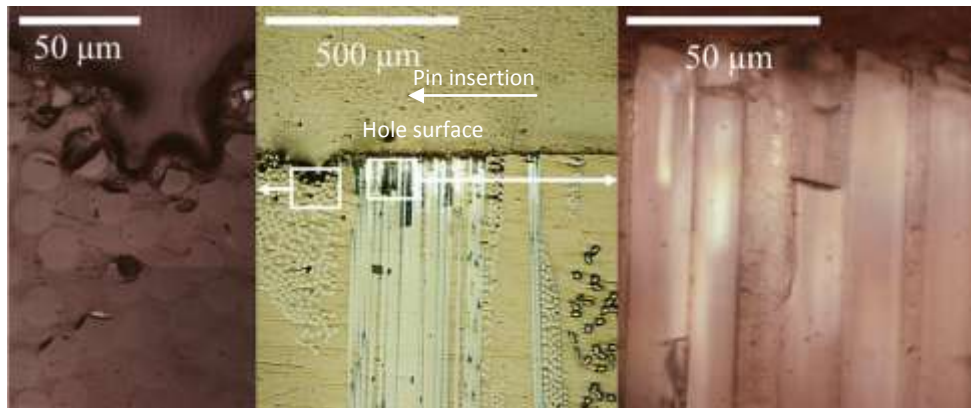
(c) 0 degree plane showing the 90 degree ply

**Fig. 15** Sectioned images of 1% interference-fit GFRP sample

Figures 15 show the sectioned microscope images at both 0 and 45 degree planes of the I=1% sample. Due to the interference-fit pin, hole surface became rough and micro-scale damage can be observed near the hole surface. Micro-scale damage to the fibres includes fibre de-bonding, cracking and breakage near the hole surface area where the contact between the pin and GFRP is severe. Due to the damage, the strains might have been released after peak point and less radial and tangential strains remain. The maximum damage depth is approximately 250  $\mu\text{m}$  from the hole surface. Figure 15(a) shows the GFRP hole sectioned at 45 degree and fiber cracking and breakage are observed mostly at the 90 degree plies. Figures 15 (b) and (c) show the sectional microscope images at the 0 degree plane. No severe fibre brakeage has been found at the 90 degree plies except few fibre cracking exists near the hole surface. Because most of the radial force from the pin is resisted by fibres at the 0 degree plies so that most of the fibre damage such as fibre cracking and debonding were observed at the 0 degree plies. The fibre damage area at the 0 degree plies extends approximately 250  $\mu\text{m}$  in depth. Fibre damage up to approximately 250  $\mu\text{m}$  caused strain relief during the pin installation when 1% interference-fit pin is installed, showing the strain magnitude drop around 120 seconds during the pin installation experiment.



(a) 45 degree plane showing the 90 degree ply



(b) 0 degree plane showing both the 90 degree and 0 degree plies

**Fig. 16** Sectioned images of 0.4% interference-fit GFRP sample

Figures 16 show the sectioned microscope images at both 0 and 45 degree planes after installing a 0.4% interference-fit pin. Fibre damage such as fibre cracking, breakage and de-bonding on both 0 and 90 degree plies is observed occasionally near the hole surface up to approximately 100  $\mu\text{m}$  in depth. When compared with the  $I=1.0\%$  sample, the damage area is much smaller. In addition, no fibre damage was observed in some regions of the  $I=0.4\%$  sample while the  $I=1.0\%$  sample contains fibre damage on the entire hole surface. The strain gauge test results of the  $I=0.4\%$  sample agree well with the FEA results and this is mainly because fibre damage is minimal with  $I = 0.4\%$ .

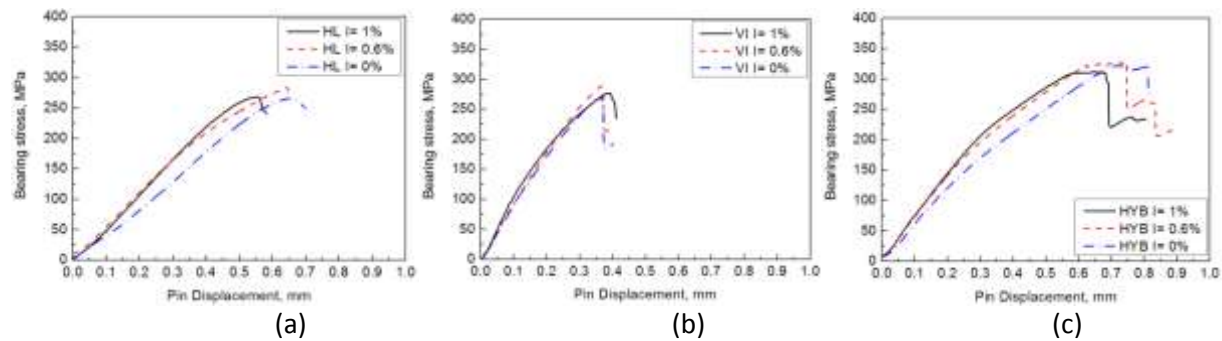
#### 4. BEARING STRENGTH AND FATIGUE LIFE TEST RESULTS

##### 4.1 Bearing Strength Analysis.

Typical bearing stress vs pin displacement graphs for each sample were presented in Fig. 17. The curves rise quickly in a linear fashion and end abruptly in failure. Table 4 presents the average values of the slope of the curves (joint stiffness per unit bearing area), the bearing strength, and displacement at maximum bearing stress. The joint stiffness per unit bearing area can be defined as the slope of the linear portion of the stress-deformation curve and is a measure of the rigidity of the joint [32]. Figure 17 demonstrates that the curves with higher interference-fit percentages have larger joint stiffness per unit bearing area. This shows that the interference-fit pin actually increases the stiffness of the joint, while

providing a decrease in the stress concentration forces in the vicinity of the hole [18,19]. This may be due to local pre-compression stresses induced by inference-fit, which improves the joint stiffness [19]. Regardless of the fabrication processes, the joint stiffness per unit bearing area increases with increasing interference-fit percentage. Table 4 clearly show that the overall bearing stiffness properties are much higher for the VI sample than for the HL or HYB samples. This correlates well with the tensile and compressive modulus data as shown in Table 2.

As shown in Figs. 17(b) and 17(c), VI and HYB curves with 1% interference-fit show the slope changes in the mid-section of quasi-static curve. It is considered that this phenomenon is induced by damage during pin insertion with an excess amount of interference-fit. Unlike these, in case of HL, the bearing strength increase, up to 1% interference-fit, and the slope don't change in the mid-section of quasi-static curve. It is considered that this phenomenon is caused by the stretching ability of resin-rich HL material, as shown in Fig. 17(a).



**Fig. 17** Typical quasi-static curves (a) HL (b) VI (c) HYB.

**Table 4** Average max bearing stress (MPa), average max pin displacement at max bearing stress and average joint stiffness per unit bearing area are vs. interference fit % for all fabrication process types tested with standard deviation.

|  |     | Interference-fit percentage |               |               |
|--|-----|-----------------------------|---------------|---------------|
|  |     | 0                           | 0.6           | 1             |
| Average maximum bearing stress (MPa)                             | HL  | 267.39±10.73                | 275.25±10.79  | 279.97±11.30  |
|  | VI  | 263.51±7.78                 | 279.94±14.02  | 262.91±23.39  |
|  | HYB | 324.87±27.96                | 344.19±18.85  | 324.79±12.97  |
| Average maximum pin displacement at maximum bearing stress (MPa) | HL  | 0.569±0.126                 | 0.749±0.192   | 0.622±0.253   |
|  | VI  | 0.366±0.001                 | 0.413±0.068   | 0.394±0.010   |
|  | HYB | 0.710±0.022                 | 0.724±0.061   | 0.715±0.060   |
| Average joint stiffness per unit bearing area (MPa/mm)           | HL  | 567.21±23.83                | 576.71±56.99  | 578.80±36.90  |
|  | VI  | 995.96±57.38                | 1121.13±70.93 | 1181.63±29.64 |
|  | HYB | 703.57±36.44                | 788.59±41.45  | 826.42±48.33  |

Maximum bearing stress can be defined as the applied maximum load divided by the bearing area, defined by the diameter of the pin multiplied by the thickness of the specimen [30]. The maximum bearing strength considered in this paper is located at the point of initial laminate failure [33]. All of the data after initial failure is ignored in this analysis, since the hole is no longer successfully containing the pin. Samples of VI and HYB reach a higher maximum load as interference-fit percentage increases, up to 0.6% interference-fit and decreases at 1% interference-fit. Unlike these, the bearing strength of HL



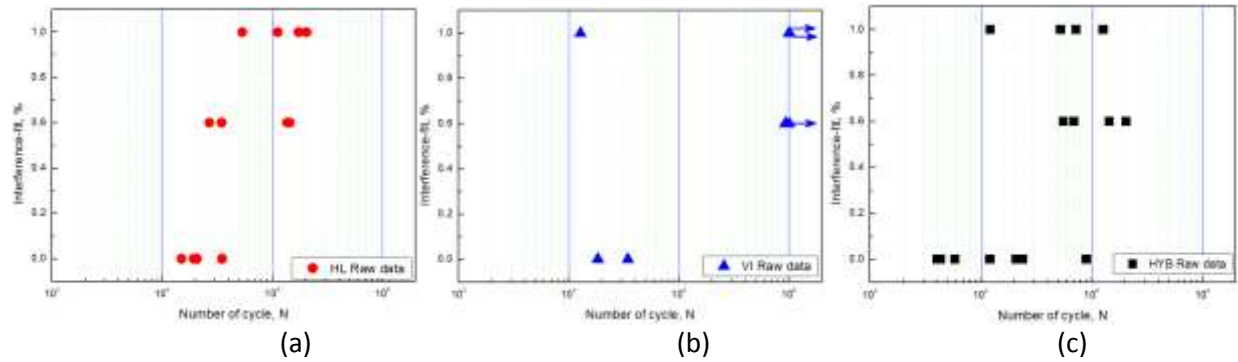
sample increases, up to 1% interference-fit. A recent study [19] shows that small gains, approximately 3%, in bearing strength are found due to the use of interference-fit fasteners when both of W/D and E/D are set as 4. This study shows the similar results. Small improvements in bearing strength are found as interference-fit is increased in the case of 0.6%. Average bearing strength of I = 0.6% sample shows approximately 2.9% (HL), 6.2% (VI), and 6.0% (HYB) higher than that of I = 0% sample. When considering the scatter of raw data, the bearing strength values of I = 0.6% sample are not always higher than those of I = 0% sample.

When it comes to the VI sample, even though small improvements in bearing strength are found in I = 0.6% and 1%, bearing strength data of 0.6% and 1% are more scattered when compared with I = 0% sample. This may be due to locally damaged specimens with interference-fit. Even with possible local damage on the joints, interference-fit does not degrade the performance of the composite joints under static loading, especially when kept under 1%.

Note that average bearing strength of HYB sample shows approximately 22% higher than VI and HL samples. This result can be related to out-of-plane stresses, which are the stresses in the through-the-thickness direction caused by pin compression. When pin loading is applied to the hole, the bearing load may induce inter- and intra-laminar macroscopic cracks due to out-of-plane stresses [34]. It is well known that bearing strength can be improved due to a clamping force by nut, washer, etc., which results to reduce the resultant out-of plane stresses [35, 36]. In HYB sample, the thick HL portion may act as a nut to obstruct out-of plane stresses of the VI portion, which carries most loading.

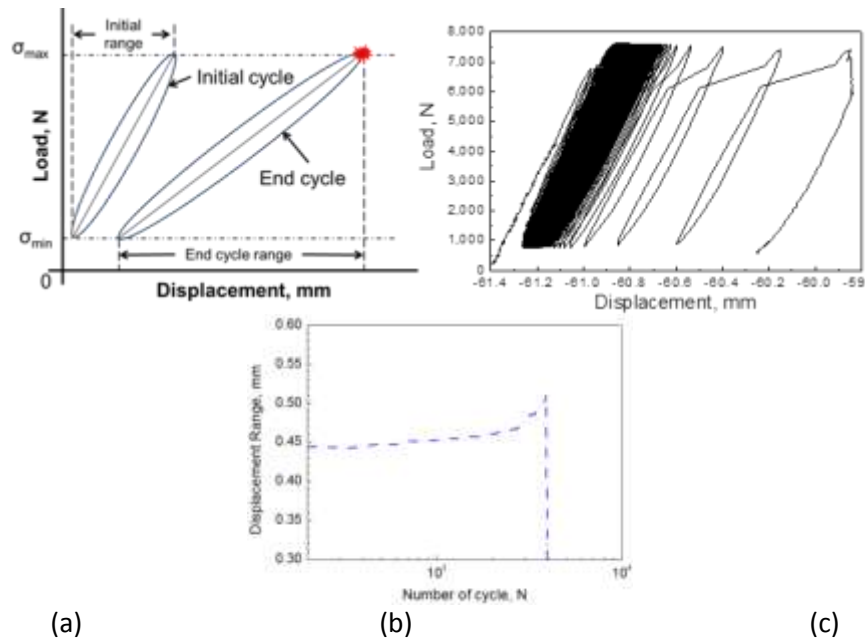
## **4.2 Fatigue Properties.**

Figure 18 show the number of cycles to failure for each coupon, in each process type. The fatigue life was greatly affected by the amount of interference fit imposed, regardless of the process type. In all cases, the average fatigue life of the samples was extended as the interference fit percentage of the pins was increased to I=0.6%. It is apparent that an increase in interference fit percent greatly improves the fatigue life of VI sample. The I=0.6 % VI sample attains the longest fatigue life, which is approximately 37 times longer average fatigue life than the I=0% VI sample. The I=1% coupons still generally outperform 0% interference samples, but the damage caused by pin insertion definitely affects these coupons in fatigue testing. For the results, the VI coupons with 1% of interference fit tend to be a little more scattered. The poor performance of I=1% VI coupons can be attributed to pin installation damage. The fatigue lives of HL and HYB samples are also affected by interference fit pins, but to a much lower degree. In both HL and HYB samples infinite life was never achieved during fatigue analysis. When it comes to the HL sample, the average fatigue life increases with increasing the interference-fit % up to 1 %. The I=1% HL sample has approximately 6 times longer average fatigue life than the I=0% HL sample. The HYB samples show the greatest gains in average fatigue life in the 0.6% of interference fit range. The I=0.6% HYB sample has approximately 5 times longer than the I=0% HYB sample.

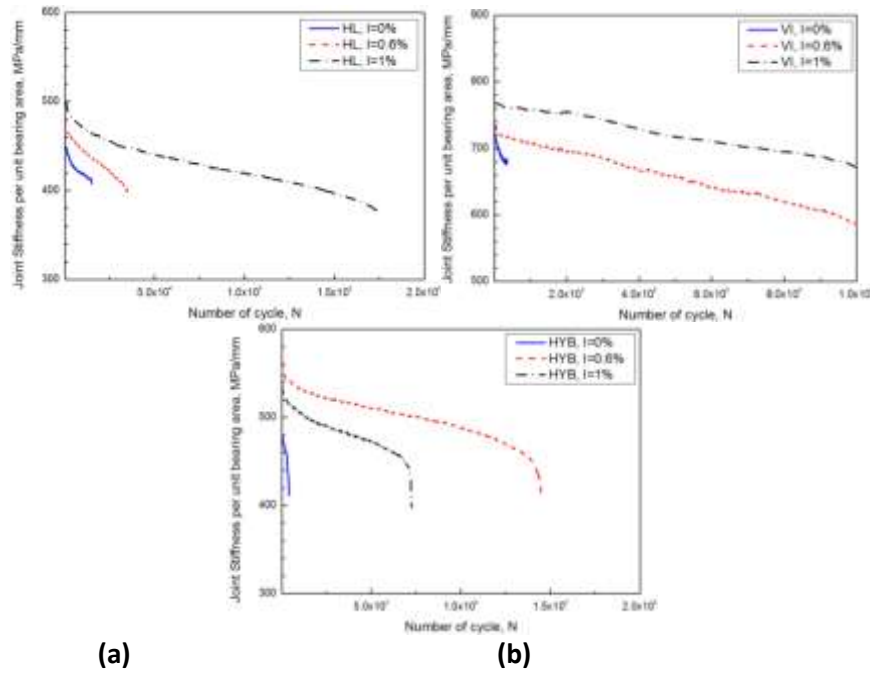


**Fig. 18** Interference Fit % vs. Cycles to Failure (Arrows indicate run-out specimens.) (a) HL (b) VI (c) HYB.

Figure 19 (a) shows a typical load versus pin displacement plot for a fatigue specimen. The pin displacement range can be defined as the difference between the maximum and the minimum displacements of a pin. Often, the pin displacement range in the beginning of fatigue test is very small due to the undamaged composite stiffness and resistance to pin deflection. As fatigue failure is initiated in the joint and the pin displacement range increases as shown in Fig. 19 (a). Figure 19 (b) shows an entire load displacement curve for a typical fatigue test. From this plot it is easy to see that the amount of deformation for a great deal of cycles stays very small due to the resistance of the coupon to failure. Near the end of the life of the sample the displacement moves very quickly as the sample finally breaks apart as seen by the large sweeping motions of the graph toward the right. The load-displacement curve can be plotted as the pin displacement range versus fatigue cycles curve, as shown in Fig. 19 (c). The joint stiffness per unit bearing area was then obtained from the ratio of the applied maximum bearing stress to the pin displacement range under fatigue cycles.

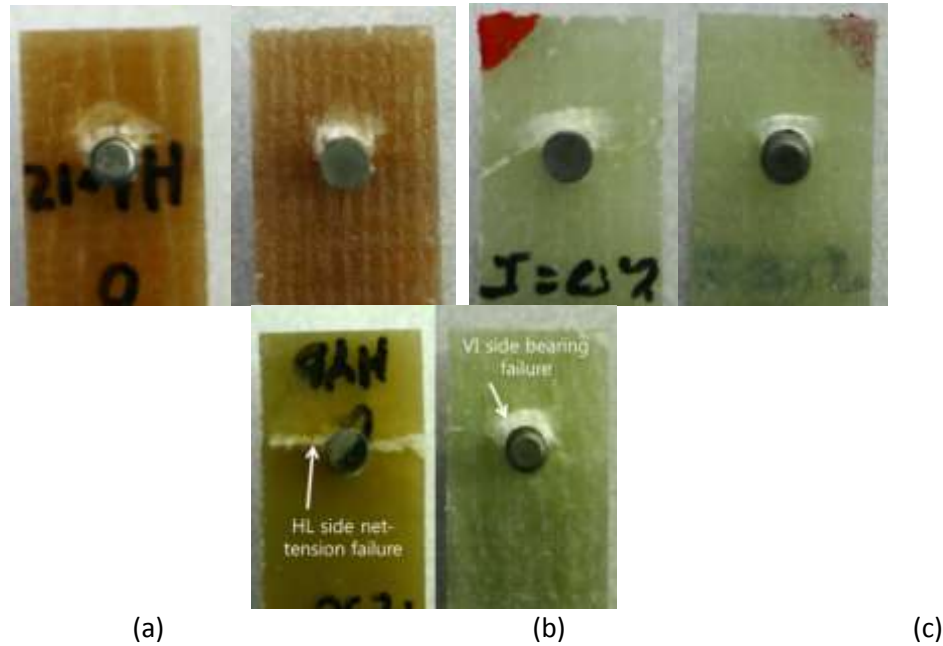


**Fig. 19** (a) a typical load versus pin displacement plot for a fatigue specimen, (b) an entire load displacement curve for a typical fatigue test, (c) the pin displacement range versus fatigue cycles curve (HL, I = 0%).



**Fig. 20** The joint stiffness per unit bearing area versus fatigue cycles (a) HL (b) VI (c) HYB.

Fig. 20 presents the joint stiffness per unit bearing area versus fatigue cycles in each sample. For all coupons, stiffness degradation was observed so the joint stiffness per unit bearing area decreases when cycles increase. The joint stiffness per unit bearing area in the beginning of the fatigue testing increases with increasing the interference-fit %. This improved the joint stiffness per unit bearing area extended the fatigue life. Interference-fit not only increases the joint stiffness per unit bearing area value but also decreases stiffness degradation. For all  $I=0\%$  coupons in Fig. 20, the joint stiffness per unit bearing area drops quite rapidly as cycles increased. The joint stiffness per unit bearing area curves for the interference-fit coupons ( $I = 0.6\%$  and  $I=1\%$ ) drop in the beginning of fatigue cycles but tend to decrease linearly until they drop quickly near the failure. Note that the VI coupons with infinite fatigue life ( $I = 0.6\%$  and  $I=1\%$ ) show the linearly decreasing stiffness curves. This low rate of stiffness degradation can be due to local pre-compression stresses induced by interference-fit, which delays damage growth during fatigue loadings. Unlike HL and VI samples, HYB sample reaches a higher joint stiffness per unit bearing area as interference-fit percentage increases, up to  $0.6\%$  interference-fit and decreases at  $1\%$  interference-fit. This results the highest fatigue enhancement at  $I = 0.6\%$  for the HYB sample. In fact, the initial joint stiffness per unit bearing area of the VI coupons ranges from  $700 \text{ MPa/mm}$  to  $800 \text{ MPa/mm}$ , while HL and HYB coupons range from  $450 \text{ MPa/mm}$  to  $550 \text{ MPa/mm}$ . This shows that the load holding characteristics of the fiber-rich VI specimens is superior to the resin-rich HL specimens.



**Fig. 21** Fatigue failure characteristics of (a) HL (b) VI (c) HYB.

From the quasi-static test results, average bearing strength of HYB sample was higher than the HL and VI samples regardless of interference-fit %. In fatigue, however, the HYB coupons do not perform much better than the HL specimens. This shows that for cyclical load conditions, the failure of the HYB coupons is more dependent on the HL side failure than the stronger VI side. This idea is verified by an analysis of the fracture characteristics of the HYB coupons found in Fig. 21. For VI and HL specimens, only bearing failure modes were found regardless of interference-fit percent. However, the HYB specimens show two distinct failure modes in one specimen. The HL portion of HYB sample failed in the net-tension failure mode while the VI portion failed in the bearing failure mode. The net-tension failure mode of the HL portion of the HYB sample is mainly due to the large amount of mat layers, which consist of randomly chopped fibers on the matrix. It was reported that randomly chopped glass mat reinforced plastics with width to pin diameter ratio ( $W/D_p$ ) smaller than 5 have proven to affect the amount of bearing strength attainable by causing premature failure in net tension [37]. Due to the present sample geometry ( $W/D_p = 4$ ), premature net-tension failure may occur in the HL portion of HYB sample. During the fatigue test of the HYB sample, the cracks across the net-section of the HL side observed first. Due to the crack initiation and growth on the net-section of the HL side, the joint stiffness per unit bearing area drops quite rapidly over the cycles. This premature net-tension failure on the HL side of HYB coupons is grown, and load is then placed more heavily on the un-failed VI side. The VI portion is then failed in the bearing failure mode.

## 5 SUMMARY

In order to investigate benefits of the interference-fits, numerical and experimental studies were carried out on a pin-loaded GFRP laminate. Following are the summaries of the study.

- 1) FEA results show that interference-fit induces the compressive stresses in the radial direction while the tensile stresses remain in the tangential direction. The magnitudes of the stresses increase with increasing interference-fit percent.
- 2) The strain gauge experimental results agree well with the numerical results. The strain magnitudes after the pin installation increase with increasing interference-fit percent. Fatigue enhancement with interference-fit up to 1% was verified with both the FEA and experimental results.
- 3) As for the sample with 1% interference-fit, discrepancy between the experimental result and the numerical result was observed on the strain profiles when installing the pin. This may be due to the micro-scale fibre damage occurred in local regions around the hole due to large amount of interference-fit percent between the pin and GFRP hole during the pin installation experiments.
- 4) Regardless of interference-fit percent, local fibre de-bonding was observed at 90 degree plies. This can be caused by friction between pin and specimen from driving force. At 0 degree fibre layers, most of the damage was found to be fibre cracking, caused by the radial forces from the pin.
- 5) Overall, pin installation process with interference fit has been successfully implemented to GFRP, up to 1%. Interference-fit of 1% may occasionally induce damages around the hole during the pin installation process of VI and the VI portion of the HYB coupons. 0.6% of interference-fit is considered to create minimal damage to GFRP holes.
- 6) Average bearing strength was slightly improved after insertion of interference-fit pin up to 1%. Larger bearing strength deviation was found at the interference-fit joined samples. When considering the scatter of raw data, the bearing strength values among the samples are overlapped. The HYB sample has the largest bearing strength over the VI and HL samples because the matrix-rich HL portion of the HYB sample may obstruct inter- and intra-laminar cracks of the VI portion, which carries most loading.
- 7) The pin-loaded joints of GFRP laminate with 0.6% and 1% of interference-fit showed enhanced fatigue life than 0% of transition-fit. But, a few VI and HYB coupons with interference-fit of 1% had shorter fatigue life than 0% of transition-fit, due to their damage associated during pin installation. In VI case, three of interference-fit pin-loaded specimens were survived up to  $10^6$  cycles, while all transition-fit pin-loaded specimens failed less than  $10^5$  cycles
- 8) The joint stiffness per unit bearing area improved by interference-fit of 0.6% as approximately 1.5% (HL) and 12% (VI and HYB) in quasi-static test. This may be due to local pre-compression stresses induced by inference-fit, which improves the joint stiffness. This improved joint stiffness per unit bearing area by interference-fit may cause fatigue enhancement. In addition, interference-fit decreases the degradation rate of joint stiffness per unit bearing area over the fatigue cycles.
- 9) In both of the quasi-static and fatigue tests, the HL portion of HYB sample failed in the net-tension failure mode while the VI portion failed in the bearing failure mode. For cyclical load conditions, the failure of the HYB coupons is much more dependent on the HL side failure than the stronger VI side.

## 6 REFERENCES

- [1] Kim D, Hennigan DJ and Beavers K. Effect of fabrication processes on mechanical properties of glass fiber reinforced polymer composites for 49 meter (160 foot) recreational yachts. *International Journal of Naval Architecture and Ocean Engineering* 2010; 2(1): 45-56.
- [2] Kim D and Ramulu M, Study on the drilling of titanium/graphite hybrid composites. *ASME Transactions Journal of Engineering Materials and Technology*, 2007; 129: 390-396.

- [3] Kim D, Kim Y, Gururaja S, and Ramulu M. Processing and fiber content effects on the machinability of compression moulded random direction short GFRP composites. *International Journal of Automotive Technology*. 2010; 11(6): 849-855.
- [4] Choi J-H, Kang M-S, Koo J-M, Seok C-S and Kim H-I. Fatigue crack propagation behavior according to fiber arraying direction for load direction in woven CFRP composite. *International Journal of Modern Physics B* 2010; 24; 15-16.
- [5] Ducept F, Davies P and Gamby D. Mixed mode failure criteria for a glass/epoxy composite and an adhesively bonded composite/composite joint, *International Journal of Adhesion and Adhesives* 2000; 20(3): 233-244.
- [6] Canyurt OE and Zhang J. Pre-stressed adhesive strap joints for thick composite sandwich structures. *International Journal of Mechanical Sciences* 2006; 48(4); 389-399.
- [7] Camanho PP and Matthews FL. Stress analysis and strength prediction of mechanically fastened joints in FRP: A review. *Composites Part A* 1997; 28(6): 529-547.
- [8] Tserpes KI, Labeas G, Papanikos P and Kermanidis T. Strength prediction of bolted joints in graphite/epoxy composite laminates. *Composites Part B* 2002; 33 (7): 521-529.
- [9] Choi J-H, Ban C-S and Kweon J-H. Failure load prediction of a mechanically fastened composite joint subject to a clamping force. *Journal of composite materials* 2008; 42; 1415-1429.
- [10] Ireman T, Ranvik T and Eriksson I. On damage development in mechanically fastened composite laminates. *Composite Structures* 2000; 49; 151-171.
- [11] Lanza Di Scalea F, Cloud GL and Cappello F. A Study on the Effects of Clearance and Interference Fits in a Pin-Loaded Cross-Ply FGRP Laminate. *Journal of Composite Materials* 1998; 32(8); 783-801.
- [12] Okutan B, Aslan Z and Karakuzu RA. Study of the effects of various geometric parameters on the failure strength of pin-loaded woven-glass-fiber reinforced epoxy laminate. *Composite Science & Technology* 2001; 61; 1491-1497.
- [13] Ahn H-S, Kweon J-H and Choi J-H. Failure of unidirectional-woven composite laminated pin-loaded joints. *Journal of Reinforced Plastics and Composites* 2005; 24; 735-752.
- [14] Bunin BL. *Critical composite joint subcomponents*. N87-10975, 1987.
- [15] McCarthy MA, Lawlor VP, Stanley WF and McCarthy CT. Bolt-hole Clearance effects and strength criteria in single-bolt, single lap, composite bolted joints. *Composites Science and Technology* 2002; 62; 1415-1431.
- [16] Liu Ping and Zhang Kaida. An experimental study on fatigue life of interference-fit composite joint. *ACTA Aeronautica et Astronautica Sinica*. 1991; 12; 545-548.
- [17] Sendeckyj GP and Richardson MD. Fatigue behavior of a graphite-epoxy laminate loaded through an interference-fit pin. *Proceedings of 2<sup>nd</sup> Air Force Conference on Fibrous Composites in Flight Vehicle Design, Tech. Rep. AFFDL-TR-74-103, Air Force Flight Dynamics Lab, WPAFB, Ohio* 1974.
- [18] Pradhan B and Babu PR. Assessment of beneficial effects of interference-fit in pin-loaded cross-ply FGRP laminate. *Journal of Reinforced Plastic Composite* 2007; 26; 771-788.
- [19] Kiral BG. Effect of the clearance and interference-fit on failure of the pin-loaded composites. *Materials and Design* 2010; 31; 85-93.
- [20] Benchechou B, White RG. Stresses around fasteners in composite structures in flexure and effects on fatigue damage initiation. Part 1: cheese-head bolts. *Composite Structure* 1995; 33(2): 95-108.
- [21] Pierron F, Cerisier F, Grediac M. A numerical and experimental study of woven composite pin-joints. *Journal of Composite Materials* 2000; 34(12): 1028-1054.
- [22] Belingardi, G., Cavatorta, M.P., and Paolino, D.S., 2008, "Repeated impact response of hand lay-up and vacuum infusion thick glass reinforced laminates," *Int. J. Imp. Eng.*, **35**, pp. 609-619.

- [23]Amenabar, I., Mendikute, A., Lopez-Arraiza, A., Lizaranzu, M., and Aurrekoetxea, J., 2011, "Comparison and analysis of non-destructive testing techniques suitable for delamination inspection in wind turbine blades," *Composites : Part B*, **42**, pp. 1298-1305.
- [24]Aktas, A., 2005, "Bearing strength of carbon epoxy laminates under static and dynamic loading," *Comp. Struc.*, **67**, pp. 485-489.
- [25]Karakuzu, R., Gulem. T, and Icten, B.M., 2006, "Failure analysis of woven laminated glass-vinylester composites with pin-loaded hole," *Comp. Struc.*, **72**, pp.27-32.
- [26] ASTM D695: Standard test method for compressive properties of rigid plastics. ASTM International, West Conshohocken, PA, USA.
- [27]ASTM D732: Standard test method for shear strength of plastics by punch tool. ASTM International, West Conshohocken, PA, USA.
- [28]ASTM D3039: Standard test method for tensile properties of polymer matrix composite materials. ASTM International West Conshohocken, PA, USA.
- [29]ASTM D3846: Standard test method for in-plane shear strength of reinforced plastics. ASTM International, West Conshohocken, PA, USA.
- [30]ASTM D953: Standard test method for bearing strength of plastics. ASTM International, West Conshohocken, PA, USA.
- [31]Marc 2010 User's Guide. Santa Ana: MSC Software, 2010.
- [32]Liu D, Raju BB, and You J. Thickness effects on pinned joints for composites. *Journal of Composite Materials* 1999;33(01):2-21.
- [33]Camanho, P.P., and Lambert, M., 2006, "A design methodology for mechanically fastened joints in laminated composite materials," *Compo. Sci. Tech.*, **66**, pp. 3004-3020.
- [34]Vieille, B., Aucher, J., and Taleb, L., 2011, "Woven ply thermoplastic laminates under severe condition: Notched laminates and bolted joints," *Composites : Part B*, **42**, pp.341-349.
- [35]Sen, F., Pakdil, M., Sayman, O., and Benli, S., 2011, "Experimental Failure Analysis of Glass-Epoxy Laminated Composite Bolted-Joints with Clearance Under Preload," *Int. J. Dam. Mech.*, **20**, pp.163-178.
- [36]Pekbey, Y., 2008, "The Bearing Strength and Failure Behavior of Bolted E-Glass/Epoxy Composite Joints," *Mech. Comp. Mater.*, **44**(4), pp. 397-414.
- [37]Caprino, G., Giorleo, G., Nele, L., Squillace, A., 2002, "Pin bearing strength of glass mat reinforced plastics," *Composites : Part A*, **33**, pp. 779-785.